
# $Ti_3C_2T_x$ as an Advanced Support Material for Polymer Electrolyte Fuel Cell Catalysts to Facilitate the Oxygen Reduction Reaction

Dissertation submitted in partial fulfilment of the requirements for the degree Master of Science in Engineering in Chemical Engineering (MScEng Chem Eng)

Author: Tyler Daniel America

Supervised by: Dr Tokoloho Rampai & Associate Professor Pieter Levecque

HySA/Catalysis Centre of Competence

Department of Chemical Engineering

University of Cape Town

31st of March 2022

# Plagiarism Declaration

I know the meaning of plagiarism and declare that all the work in the document, save for that which is properly acknowledged, is my own. This dissertation has been submitted to the Turnitin module (or equivalent similarity and originality checking software) and I confirm that my supervisors have seen my report and any concerns revealed by such have been resolved with my supervisors.

Signed: Signed by candidate

Date: 31st of March 2022

# Acknowledgements

This work is the culmination of self-sacrifice and determination but could never have been completed without the support I received from those around me. This support formed the foundation on which I was able to conduct this research and perform at a level deserving of a master's degree.

To the University of Cape Town, thank you for continuing to prioritise students. From the impact of the Covid-19 pandemic to the mountain fire, I never lost faith that operations would continue, and my best interests be retained. Through HySA Catalysis, who were the sponsors of this project, I was able to get the necessary materials and equipment timeously. For this, I extend an enormous vote of thanks to both the University for their facilities and HySA Catalysis for their sponsorship. My friends, peers, the analytical laboratory team, centre for imaging and analysis team, as well as all Catalysis technical and research staff at the University of Cape Town – thank you for always extending a helping hand.

To my family, we will now have plenty more time for adventures! Thank you for your continued support throughout this journey. There were times where doubt overcame me, but your guidance always kept me aligned with priorities. To my supervisors, TK and Pieter without whom none of this would have been possible. From the day I started lab work to the day of submission, you allowed me to shape my own path while offering me so much guidance. This afforded me opportunities to achieve what I never thought possible. I cannot thank you enough for this or the knowledge you have shared.

To my wife Kaylin, this has been a process and I am so glad to have had you at my side through it all. Your upliftment in tough days offered me courage and your high spirits always kept me motivated. Thank you for the sacrifices you have made to help me realize this opportunity.

In ending (unknown author),

- You don't have to be great to start, but you have to start to be great.

# Abstract

Polymer electrolyte fuel cell's (PEFC's) have the potential to offer a leading energy conversion technology. These fuel cells make use of hydrogen and oxygen and by means of a chemical reaction, electricity, heat and liquid water are produced. In 2015 the Department of Energy (DoE) of the United States declared a 5000-hour lifetime target for transport applicable fuel cells. With current technological limitation, the achieved lifespan is, however, restricted to only 1700-hours. An assessment to find a more active but primarily more durable support for the oxygen reduction reaction (ORR) in a PEFC than the currently employed carbonaceous support was therefore undertaken.

A MXene, $Ti_3AlC_2$ was selected for assessment based on its theoretically suitable electrical and thermal conductivities, as well as its possession of among the strongest resistance to oxidation of the many different MAX phases.

The synthesis of high (>50 $m^2 g^{-1}$), specific surface area, delaminated $Ti_3C_2T_x$ flakes was attempted first with mild in-situ HF conditions. While this method could both etch and delaminate flakes in a single stage, because the flake size remained large and unchanged, the specific surface area was not seen to increase to the outlined requirements. To synthesize $Ti_3C_2T_x$ flakes with a high specific surface area, HF etching was therefore employed. In this report, 0.5 g of 400-mesh $Ti_3AlC_2$ flakes synthesized by hot pressing were etched in 10 ml of 48 wt % HF for 24 hours at 30 °C. After micronizing for 10 minutes and probe sonicating in solution for a further 40 minutes, high specific surface area (86 $m^2 g^{-1}$), delaminated $Ti_3C_2T_x$ flakes were attained. Using metal organic chemical deposition, well dispersed 2-5 nm platinum particles were successfully deposited onto the support material.

Initial electrochemical performance evaluations indicated a lack of conductivity which restricted electron transport and therefore limited catalyst activity. This was determined to be the result of more defective flakes and by correlation, an increase in interfaces leading to increased resistance. With the incorporation of carbon to the catalyst material to synthesize a hybrid electrode, a positive result confirming ORR activity was attained. While the electrochemical surface area (ECAS) was less than half of that of Pt/C (80 vs 28 $m^2 g^{-1}$), it confirmed where the synthesis constraints lie.

In review of the durability results, it was found that trapped intermediates between high specific surface area MXene sheets not only restricts access to catalytic sites but are further protonated and reduced to form hydrogen peroxide which causes irreversible damage the PEFC's catalyst membrane.

# Table of Contents


Plagiarism Declaration ..... i
Acknowledgements ..... ii
Abstract ..... iii
List of Illustrations ..... vi
List of Tables ..... x
Nomenclature ..... xii
Chapter One: Introduction ..... 1
Chapter Two: Literature Review ..... 3
2.1 Polymer Electrolyte Fuel Cells ..... 3
2.1.1 PEFC Operating Principles ..... 3
2.1.2 PEFC Operating Parameters ..... 4
2.1.3 PEFC Catalyst Shortcomings ..... 4
2.1.4 Platinum as a PEFC Catalyst for the ORR ..... 5
2.1.4.1 Motivation for Platinum Selection ..... 5
2.1.4.2 Platinum Alloys and Particle Size Distribution ..... 7
2.1.5 Catalyst Support Considerations ..... 8
2.1.5.1 Current Catalyst Support Properties and Shortcomings ..... 8
2.1.5.2 Properties of an Ideal Catalyst Support ..... 9
2.2 MAX Phases ..... 11
2.2.1 Composition and Crystal Structure of MAX Phases ..... 11
2.2.2 Atomic Bonding within MAX Phases ..... 12
2.3 MXene's ..... 12
2.3.1 Composition and Crystal Structure of MXene's ..... 12
2.3.2 MXene Properties as a Function of MAX Phases ..... 13
2.3.3 Selection of a $Ti_3AlC_2$ as the Starting MAX Phase ..... 14
2.3.4 Synthesis of $Ti_3C_2T_x$ Through the Selective Etching of $Ti_3AlC_2$ ..... 16
2.3.4.1 Using Hydrofluoric Acid ..... 16
2.3.4.2 Using in-situ Hydrofluoric Acid ..... 17
2.3.5 Delamination of $Ti_3C_2T_x$ Flakes ..... 17
2.3.5.1 Sonication as a Means of Delaminating $Ti_3AlC_2$ Flakes ..... 18
2.3.5.2 Intercalation as a Means of Delaminating Ti3AlC2 Flakes ..... 19
2.4 Electrochemical Performance Evaluation ..... 19
2.4.1 Platinum Deposition ..... 19
2.4.2 Electrochemical Surface Area Measurements ..... 20
2.5 Rationale and Sustainable Development Goals ..... 21
2.5.1 Rationale of the Study ..... 21

2.5.2 Sustainable Development Goals ..... 21
Chapter Three: Hypothesis and Key Questions ..... 22
3.1 Hypothesis ..... 22
3.2 Key Questions ..... 22
Chapter Four: Research Approach ..... 23
4.1 Experimental System ..... 23
4.2 MXene Synthesis Parameters ..... 23
4.2.1 In-situ HF Etching ..... 24
4.2.2 HF Acid Etching ..... 24
4.3 Platinum Deposition ..... 25
4.4 Electrochemical Performance Evaluation ..... 26
4.4.1 Electrode and Catalyst Ink Preparation ..... 26
4.4.2 Electrochemical System Configuration ..... 26
4.4.3 Electrochemical Surface Area and Activity Parameters ..... 27
4.4.4 Accelerated Durability Testing Parameters ..... 27
4.5 MXene Characterisation ..... 27
Chapter Five: Results ..... 29
5.1 MAX Phase Material Characterization by Batch ..... 29
5.2 $Ti_3C_2T_x$ MXene Synthesis ..... 33
5.2.1 X-ray Diffraction Analysis Considerations ..... 33
5.2.2 In-situ HF etching ..... 34
5.2.2.1 Etchant HCl:LiF Molar Ratio Optimization ..... 34
5.2.2.2 Temperature and Molar Ratio Optimization ..... 38
5.2.2.3 Etching Time Optimization ..... 40
5.2.3 HF Etching ..... 41
5.2.3.1 $Ti_3AlC_2$ Etching in 30 wt % HF for Different Times ..... 41
5.2.3.2 Concentration Changes ..... 44
5.2.3.3 Sonication of HF Etched MXene's ..... 45
5.2.3.4 Size Reduction by Mechanical Grinding ..... 48
5.2.3.5 Etching Results Summary ..... 52
5.3 Electrochemical Performance Evaluation ..... 53
5.3.1 Platinum on Carbon Baseline Activity Measurements ..... 53
5.3.2 Platinum on MXene Activity Measurements ..... 56
5.3.2.1 21 wt % (40 eq. wt % Pt/C) Platinum on $Ti_3C_2T_x$ ..... 57
5.3.2.2 40 wt % (78 eq. wt% Pt/C) Platinum on $Ti_3C_2T_x$ ..... 58
5.3.2.3 40 wt % (78 eq. wt% Pt/C) Platinum on $Ti_3C_2T_x$ after Carbon Addition ..... 60
5.3.3 Platinum on MXene Durability Measurements ..... 63
5.3.4 Platinum on Carbon Durability Measurements ..... 64

Chapter Six: Overall Discussion ..... 66
Chapter Seven: Conclusions and Recommendations ..... 69
7.1 Conclusions of the Study ..... 69
7.2 Recommendations from the Study ..... 69
References ..... 71

# List of Figures

Figure 2.1: Polymer electrolyte fuel cell basic operating principle shown as a diagram..... 3
Figure 2.2: Depiction of the associative and dissociative oxygen reduction reaction methods replicated from Holton & Stevenson (2013). ..... 5
Figure 2.3: a) Oxygen reduction activity plotted as a function of the oxygen binding energy (Jaksic et al., 1998) and b) Oxygen reduction activity as a function of O and OH binding energy (Nørskov et al., 2004). ..... 6
Figure 2.4: Diagram of catalyst nanoparticles and support material for a) the ideal Pt dispersion on the support material b) Pt dissolution resulting from support corrosion and c) Ostwald ripening via Pt agglomeration on a corroded support..... 9
Figure 2.5: Periodic Table presenting the elements constituting a MAX Phase (Halim, 2016). ..... 11
Figure 2.6: Crystalline structure by unit cells for a) 211, b) 312, and c) 413 MAX phases replicated from Barsoum & Radovic (2011). ..... 12
Figure 2.7: a) Etched $Ti_3AlC_2$ Crystal Structure by i), ii) top view and iii), iv) side view with interparticle distances in Å. Ti, C, O and F are shown in purple, grey, red, and cyan, respectively (Liu & Li, 2019) b) SEM image of etched $Ti_3C_2T_x$ etched in 49 wt % HF at 60 °C for 24 hours (Li, Wang, et al., 2015). ..... 13
Figure 2.8: SEM images of $Ti_3AlC_2$ depicting the layered structure of the MAX phase replicated from a) Zhou (2012) and b) Koyappayil & Chavan (2020). ..... 15
Figure 2.9: Crystal structure transformation from a) MAX phase to MXene b) pre and c) post sonication adapted from Naguib et al. (2011). Ti, C, Al, O and H are shown in grey, black, red, blue and pink, respsectively. ..... 18
Figure 5.1: XRD of $Ti_3AlC_2$ MAX phases synthesized by hot pressing as sourced from Easchem Co. Diffractogram is shown first by batch number and then particle size of 200 and 400-mesh, respectively, against the reference pattern of $Ti_3AlC_2$. ..... 29
Figure 5.2: SEM images of batch 1 a), b) batch 2 c), d) and batch 3 e), f) of $Ti_3AlC_2$ MAX phases synthesized by hot pressing as sourced from Easchem Co. Images a), b) and c), d) correspond to a 200-mesh particle size and e), f) a 400-mesh particle size..... 31
Figure 5.3: $Ti_3AlC_2$ material Raman spectrums shown first by batch size and then particle size. ..... 32
Figure 5.4: XRD evolution from zero to 90 hours showing a decrease in peak intensity of 0.5 g, 200-mesh $Ti_3C_2T_x$ etched in 10 ml of 30 wt % HF at 30 °C after filtering and drying at 60 °C..... 33
Figure 5.5: SEM images of 0.5 g, 200-mesh $Ti_3C_2T_x$ etched in 10 ml of 30 wt % HF at 30 °C after vacuum filtering and oven drying at 60 °C. The particle inscribed in the red square is shown at a higher magnification the adjacent right sided image. ..... 34

Figure 5.6: XRD diffractogram of 0.5 g, 200-mesh $Ti_3AlC_2$ etched in 10 ml in-situ HF at different molar ratios of LiF:HCl, for 24 hours at 35 °C against reference patterns of $Ti_3AlC_2$ and LiF. ..... 34
Figure 5.7: 0.5 g, 200-mesh $Ti_3AlC_2$ etched in 10 ml in-situ HF using a 3:1 HCl:LiF molar ratio for 24 hours at 35 °C shown at different magnifications in a) and b). ..... 35
Figure 5.8: EDS spectrum sources and elements shown in atomic weight % of 0.5 g, 200-mesh $Ti_3C_2T_x$ etched in 10 ml 3:1 HCl:LiF for 24 hours at 35 °C. ..... 36
Figure 5.9: SEM images of 0.5 g, 200-mesh $Ti_3C_2T_x$ etched at different HCl:LiF molar ratios in 10 ml in situ-HF for 24 hours at 30 °C. Images a) and b) 10:1 HCl:LiF at different magnifications & images c) and d) 6:1 HCl:LiF at different magnifications. The particle inscribed in the red square is shown at a higher magnification in the adjacent right sided image. ..... 37
Figure 5.10: XRD of 0.5 g, 200-mesh $Ti_3C_2T_x$ etched in 20 ml 3:1 HCl:LiF for 24 hours at 60 °C (covered) contrast to 0.5 g $Ti_3AlC_2$ etched in 10 ml 3:1 HCl:LiF for 24 hours at 60 °C (uncovered). ..... 39
Figure 5.11: SEM images of 0.5 g, 200-mesh $Ti_3C_2T_x$ etched in 20 ml 3:1 HCl:LiF for 24 hours at 60 °C (covered). The particle inscribed in the red square is shown at a higher magnification in the adjacent right sided image..... 40
Figure 5.12: XRD of 0.5 g, 200-mesh $Ti_3C_2T_x$ etched in 20 ml 3:1 HCl:LiF for 24 hours at 60 °C (covered) comparison to 0.5 g $Ti_3AlC_2$ etched in 20 ml 3:1 HCl:LiF for 48 hours at 60 °C (covered). ..... 40
Figure 5.13: SEM images of 0.5 g, 200-mesh $Ti_3C_2T_x$ etched in 20 ml 3:1 HCl:LiF for 48 hours at 60 °C (covered). The particle inscribed in the red square is shown at a higher magnification the adjacent right sided image..... 41
Figure 5.14: XRD diffractogram of 0.5 g, 200-mesh $Ti_3AlC_2$ etched at 30 °C in 10 ml 30 wt % HF at various time intervals from 1.5 to 24 hours against the reference pattern of $Ti_3AlC_2$. ..... 41
Figure 5.15: SEM images of 0.5 g, 200-mesh $Ti_3C_2T_x$ after etching in 10 ml in 30 wt % HF at 30 °C for 1.5 hours. The particle inscribed in the red square is shown at a higher magnification the adjacent right sided image. ..... 42
Figure 5.16: SEM images of 0.5 g, 200-mesh $Ti_3C_2T_x$ etched in 10 ml, 30 wt % HF at 30 °C for a), b) 3 hours, c), d) 6 hours, e), f) 12 hours and g), h) 24 hours. The particle inscribed in the red square is shown at a higher magnification in the adjacent right sided image..... 43
Figure 5.17: XRD diffractogram of 0.5 g, 200-mesh $Ti_3AlC_2$ etched in 10 ml 48 wt % HF at 30 °C for 24 hour comparison to 30 wt % HF at 30 °C for 24 hours against the pattern of $Ti_3AlC_2$..... 44
Figure 5.18: SEM images of 0.5 g, 200-mesh $Ti_3C_2T_x$ after etching in 10 ml of 48 wt % HF at 30 °C for 24 hours. The particle inscribed in the red square is shown at a higher magnification the adjacent right sided image. ..... 44

Figure 5.19: XRD diffractogram of 0.5 g, 200-mesh $Ti_3AlC_2$ etched in 10 ml 48 wt % HF at 30 °C for 24-hours and probe sonicated for various times from 5 to 40 minutes against the reference pattern of $Ti_3AlC_2$. ..... 45
Figure 5.20: SEM images of 0.5 g, 200-mesh $Ti_3C_2T_x$ etched in 10 ml of 48 wt % HF at 30 °C for 24 hours and probe sonicated for 5 minutes a), b) 10 minutes c), d), 20 minutes e), f) and 40 minutes g), h).. 47
Figure 5.21: XRD diffractogram of 0.5 g, 200-mesh $Ti_3AlC_2$ etched in 10 ml 48 wt % HF at 30 °C for 24-hours and ground by mortar and pestle and a micronizor before being probe sonicated for 40 minutes against the reference pattern of $Ti_3AlC_2$. ..... 48
Figure 5.22: SEM image of 0.5 g, 200-mesh $Ti_3C_2T_x$ etched in 10 ml of 48 wt % HF at 30 °C for 24 hours and ground by a), b) mortar and pestle and c), d), micronizor. The particle inscribed in the red square is shown at a higher magnification the adjacent right sided image. ..... 49
Figure 5.23: SEM images of 0.5 g, 200-mesh $Ti_3AlC_2$ etched in 10 ml 48 wt % HF at 30 °C for 24-hours and ground by a), b) mortar and pestle c), d) sonicator before being probe sonicated for 40 minutes. The particle inscribed in the red square is shown at a higher magnification the adjacent right sided image..... 50
Figure 5.24: XRD of 0.5 g, 400-mesh $Ti_3C_2T_x$ etched in 10 ml of 48 wt % HF at 30 °C for 24 hours after micronizing for 10 minutes and probe sonicating for 40 minutes with $Ti_3AlC_2$ reference. ..... 51
Figure 5.25: SEM images of 0.5 g, 400-mesh $Ti_3C_2T_x$ etched in 10 ml of 48 wt % HF at 30 °C for 24 hours after micronizing for 10 minutes and probe sonicating for 40 minutes..... 51
Figure 5.26: TEM images of a 40 wt % Pt/C commercial catalyst at different magnifications a) and b) with the histogram c) showing of the corresponding platinum particle size distribution. ..... 53
Figure 5.27: First cyclic voltammogram from 0.01 to 1.2 V versus RHE of a 40 wt % Pt/C catalyst recorded at 50 mV/s in 0.10 M deoxygenated $HClO_4$ solution recorded at room temperature..... 54
Figure 5.28: Second cyclic voltammogram from 0.01 to 1.2 V versus RHE of a 40 wt % Pt/C catalyst recorded at 50 mV/s in 0.10 M deoxygenated $HClO_4$ solution recorded at room temperature..... 55
Figure 5.29: Linear sweep curves corrected for IR drop and background current for a 40 wt % Pt/C catalyst in 0.1M $HClO_4$ solution recorded at room temperature. ..... 55
Figure 5.30: TEM images of a 40 eq. wt % Pt/C to Pt/MXene catalyst at different magnifications a) and b) with the histogram c) showing of the platinum particle size distribution..... 57
Figure 5.31: Cyclic voltammogram from 0.01 to 1.2 V versus RHE of a 40 eq. wt% Pt/C to Pt/$Ti_3C_2T_x$ catalyst at 50 mV/s in 0.10 M deoxygenated $HClO_4$ solution at room temperature..... 58
Figure 5.32: TEM images of a 40 wt % Pt/$Ti_3C_2T_x$ catalyst at different magnifications a) and b). Corresponding particle size distribution shown in Figure 5.33. ..... 58

Figure 5.33: Platinum particle size distribution of a 40 wt % Pt/$Ti_3C_2T_x$ catalyst corresponding to TEM images a) and b) in Figure 5.32. ..... 59
Figure 5.34: Cyclic Voltammogram from 0.01 to 1.2 V versus RHE of a 40 wt % Pt/MXene catalyst recorded at 50 mV/s in 0.10 M deoxygenated $HClO_4$ solution at room temperature. ..... 59
Figure 5.35: TEM images of the 46 wt % Pt/MXene at different magnifications a), b). Images c), d) show the catalyst after carbon addition (to 15 wt % of the catalysts total mass), post bath sonication for 30 minutes. ..... 60
Figure 5.36: Histogram of Pt particle size distribution based off TEM imaging from Figure 5.35 a), b) showing Pt dispersion and inter particle distance for the 46 wt % Pt/MXene. ..... 61
Figure 5.37: Cyclic Voltammogram from 0.01 to 1.2 V versus RHE of a 46 wt % Pt/MXene catalyst + 15 wt % carbon recorded at 50 mV/s in 0.10 M deoxygenated $HClO_4$ at room temperature. ..... 61
Figure 5.38: Linear sweep curves corrected for IR drop and background current for a 46 wt % Pt/MXene catalyst + 15 wt % carbon catalyst in 0.10 M $HClO_4$ solution at room temperature. ..... 62
Figure 5.39: Metal support durability measurements recorded up to 3000 cycles from 0.01 to 1.2 V versus RHE for a 46 wt % Pt/MXene catalyst + 15 wt % carbon catalyst recorded in 0.10 M deoxygenated $HClO_4$ solution at room temperature. ..... 63
Figure 5.40: Metal support durability measurements recorded to 5000 cycles from 0.01 to 1.2 V versus RHE for a 40 wt % Pt/C catalyst in 0.10 M deoxygenated $HClO_4$ solution at room temperature. ..... 64

# List of Tables

Table 1: Advanced Catalyst Supports Considered for the ORR. ..... 10
Table 2: $Ti_3C_2T_x$ in-situ HF etched SSA by different methods of grinding and sonicating ..... 52
Table 3: $Ti_3C_2T_x$ HF etched SSA by different process methods of grinding and sonicating ..... 52
Table 4: Corrected current densities of the linear sweep curves for a 40 wt % Pt/C catalyst from an RPM range of 400 to 2500 RPM referenced against results from the Levich Equation. ..... 56
Table 5: Electrochemical surface area results summary for a 46 wt % Pt/MXene catalyst + 15 wt % carbon catalyst recorded in 0.10 M deoxygenated $HClO_4$ solution at room temperature ..... 64
Table 6: Electrochemical surface area results summary for a 40 wt % Pt/C catalyst recorded in 0.10 M deoxygenated $HClO_4$ solution at room temperature ..... 65

# Nomenclature

| | |
|---|---|
| * | Catalytically active site |
| Ω | Angular rotation rate |
| CNT | Carbon nanotubes |
| CV | Cyclic voltammetry |
| $CO_2e$ | Carbon dioxide equivalent gasses |
| D | Diffusion coefficient |
| $e^-$ | Electron |
| ECSA | Electrochemical surface area |
| EDS | Energy dispersive spectroscopy |
| F | Faraday constant |
| $H^+$ | Proton |
| *In-situ* | In the original place |
| MEA | Membrane electrode assembly |
| MOCD | Metal organic chemical deposition |
| n | Number of electrons transferred in a half reaction |
| ORR | Oxygen reduction reaction |
| PEFC | Polymer electrolyte fuel cell |
| PEM | Proton exchange membrane |
| $Pt(acac)_2$ | Platinum (II) acetylacetonate |
| RDE | Rotating disk electrode |
| RHE | Reversible hydrogen electrode |
| SEM | Scanning electron microscopy |
| TEM | Transmission electron microscopy |
| $\nu$ | Kinematic Viscosity |
| XRD | X-Ray diffraction |

# Chapter One: Introduction

It has been determined that the transport sector is responsible for 14 % of the 45 billion tonnes of $CO_2e$ (carbon dioxide equivalent), emissions in 2017. While the transport sector does not impact as significantly as the power generating sector (25 % of the total $CO_2e$ emissions), it is seen as having the largest short-term potential to reduce these emissions (Holmberg & Erdemir, 2017; IPCC, 2018).

To promote renewable energy as a viable solution to support the reduction in $CO_2e$ emissions, the development of efficient storage and conversion technologies are required. To this end, Polymer electrolyte fuel cell's (PEFC's) have the potential to offer a leading energy conversion technology. These fuel cells make use of hydrogen and oxygen and by means of a chemical reaction, electricity, heat, and liquid water are produced. In 2015 the Department of Energy (DoE), of the United States declared a 5000-hour lifetime target for transport applicable fuel cells. With current technological limitation, the achieved lifespan is restricted to only 1700-hours. The limitations are mainly due to the oxygen reduction reaction (ORR), the cathode reaction within the PEFC. This reaction has slow kinetics and occurs in a low pH and an oxygen rich environment. Platinum was introduced as an electrocatalyst in a PEFC to speed up the kinetics, however, the current support material of choice, carbon black, is often oxidised due to the harsh operating conditions. This support corrosion leads to platinum particle detachment and agglomeration both of which decrease the PEFC's efficiency and durability.

Advanced support materials such as carbon nanotubes (CNT's), graphene and inorganic oxides are a few developments in the space of catalysis. While CNT's and graphene show promising characteristics with respect to their surface areas and power densities, they are still subject to varying degrees corrosion. Then, while inorganic oxides have a high corrosion resistance, they require larger platinum nanoparticles which only further increases already high platinum costs. It is therefore clear that, a new class of catalyst supports need to be identified which hold the desired features of both activity and durability. To this end, $Ti_3C_2T_x$ was assessed. $Ti_3C_2T_x$ is a negatively charged, ternary layered carbide synthesised by the exfoliation of $Ti_3AlC_2$. Literature suggests $Ti_3C_2T_x$ MXene sheets possess suitable conductivity, an adequate pore size, a strong corrosion resistance which would hinder the detachment of platinum particles and can have specific surface areas of up to 68 $m^2\ g^{-1}$.

The objective of this study was therefore to determine if $Ti_3C_2T_x$ can offer a more active but primarily more durable support for the ORR in a PEFC than the currently employed carbonaceous supports.

All $Ti_3C_2T_x$ synthesis routes investigated in this report were at the lowest feasible operating temperature, with the shortest possible etching time and with HF concentrations kept to a minimum. These conditions maintained that the scope of work be kept to the mildest possible conditions such that the desired MXene properties could be attained. This consideration was made due to the extreme risk presented by the etching solution.

# Chapter Two: Literature Review

## 2.1 Polymer Electrolyte Fuel Cells

### 2.1.1 PEFC Operating Principles

A polymer electrolyte fuel cell's (PEFC's) consists of three key components: an anode, a cathode, and the proton exchange membrane (PEM). Together, these components form the membrane electrode assembly (MEA). The membrane is composed of a hydrated solid and promotes proton conduction. Furthermore, the membrane which is chemically resistant, acidic, absorptive and ultimately a good proton ($H^+$) conductor when hydrated, and allows proton transfer which permits the energy generation process (Rayment & Sherwin, 2003). Typically, these membranes are produced from Nafion, although other types of membranes are sometimes used. A PEFC has an electric efficiency between 50-60 % and typically operates between 50-100 °C (Palatkar, Dhopte & Sajjanwar, 2017).

Shown in Figure 2.1 is the principle of operation. Each electrode in the fuel cell makes use of its own catalyst to perform a function. On the anode side, the catalyst dissociates hydrogen into protons and electrons. As mentioned, the membrane between the electrodes is designed to be electrically insulating, thus, only the protons will pass through leaving the electrons to travel an external pathway, which then becomes the utilized power supply. On the cathode side, oxygen molecules react with hydrogen ions and the returned electrons, to form water (Rayment & Sherwin, 2003). The reactions taking place at the anode and cathode are shown in Equations 1 and 2, respectively:

$$H_2 \rightarrow 2H^+ + 2e^- \quad (1)$$

$$\tfrac{1}{2} O_2 + 2H^+ + 2e^- \rightarrow H_2O \quad (2)$$

Finally, because high temperatures are not required to hydrate the PEM, PEFC's are able to operate at the temperatures described above.

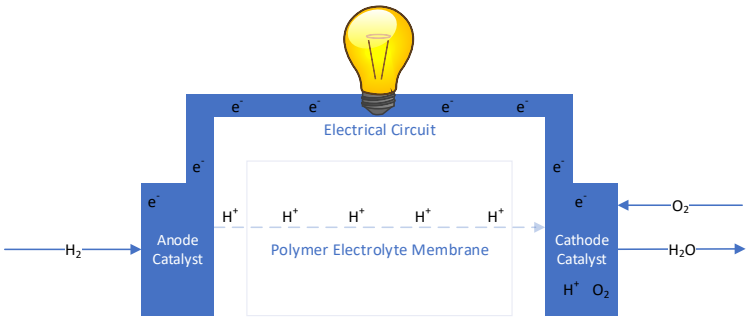


Figure 2.1: Polymer electrolyte fuel cell basic operating principle shown as a diagram.

### 2.1.2 PEFC Operating Parameters

The efficiency of a fuel cell is limited by the management of its operating conditions. Since the product of Equation 2 is water, it is important to avoid electrode flooding which will decrease the availability of active sites for the desired Equations 3-5 to occur. As mentioned, it is important that the PEM remains hydrated to facilitate proton transfer. Consequently, it is required to maintain a balance between the rate of water removal and retention.

In addition to water management, air flow must also be regulated. The rate of air flow or in some cases oxygen flow, must again be governed so as not to dry either of the electrodes or the PEM. The airflow must therefore be regulated in tandem with the water management system to maintain optimal efficiency and durability of all components.

The rate of water formulation is of course by Equation 2, dependant on the activity of the catalyst. It is therefore predicted that the increased durability of a novel catalyst support will also make the PEFC easier to control. This is given that the rate of water retention will then be constant over a longer time period (Rayment & Sherwin, 2003).

### 2.1.3 PEFC Catalyst Shortcomings

In a PEFC and for the oxygen reduction reaction (ORR), taking place on the cathode, the catalyst is solid platinum (Pt) nanoparticles, deposited on an inert, high surface area (± 250 $m^2 g^{-1}$), carbonaceous support. The reactants within the cell are both gaseous $O_2$ and $H_2$ making the reaction heterogeneous.

In accordance with Wu et al. (2020), the commercial viability of PEFC's is limited by the ORR taking place on the cathode which has very slow kinetics. It is because of this slow reaction that electrocatalysis was introduced. The preferred of the two mechanisms by which the ORR can proceed, is the dissociative or four-electron process. This process was described by Holton & Stevenson (2013), and is shown in Equations 3-5; where * denotes a catalytically active site.

$$½\ O_2 + * \rightarrow O* \quad (3)$$

$$O* + H^+ + e^- \rightarrow OH* \quad (4)$$

$$OH* + H^+ + e^- \rightarrow H_2O + * \quad (5)$$

As seen in Equation 3, $O_2$ is adsorbed to the metal surface where its bonds are broken, and individual oxygen atoms attained. Following in Equation 4, these atoms are protonated by the $H^+$ ions from across the PEM, and then reduced by electrons returned from the external circuit.

Finally in Equation 5, the bound OH* molecules are further protonated and reduced before leaving the metal surface as $H_2O$. The unpreferred, associative or two-electron process involves the preservation of the O=O bonds shown in Equation 2. This leads to the process described in Equations 6 to 9 (Holton & Stevenson, 2013).

$$O_2 + * \rightarrow O_2* \quad (6)$$

$$O_2* + H^+ + e^- \rightarrow HO_2* \quad (7)$$

$$HO_2* + H^+ + e^- \rightarrow H_2O_2* \quad (8)$$

$$H_2O_2* \rightarrow H_2O_2 + * \quad (9)$$

As seen in Equation 6, the O=O bonds are retained, and oxygen adsorbed onto the catalyst surface. In Equation 7, the adsorbed oxygen is protonated and reduced and in Equation 7, the previous product subjected to the same process. What this leads to, as seen in Equation 8, is the formation of hydrogen peroxide ($H_2O_2$), which will either react further or desorb. Figure 2.2, replicated from Holton & Stevenson (2013) summarises the two mechanisms.

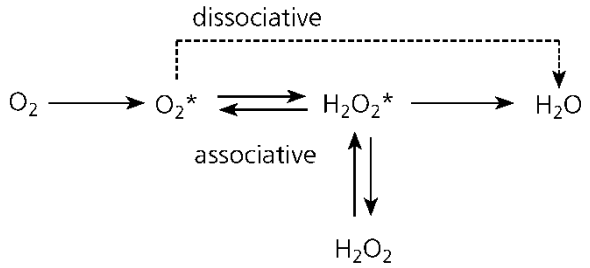


Figure 2.2: Depiction of the associative and dissociative oxygen reduction reaction methods replicated from Holton & Stevenson (2013).

Where the associative mechanism is taking place and hydrogen peroxide formed, significant harm to the PEM is incurred. This is the result of its rapid PEM degradation occurring in the presence of $H_2O_2$ (Holton & Stevenson, 2013). A good catalyst can therefore be described as one which favours the dissociative over the associative mechanism.

### 2.1.4 Platinum as a PEFC Catalyst for the ORR

#### 2.1.4.1 Motivation for Platinum Selection

The ORR occurs at the cathode of the PEFC in a low pH and an oxygen rich environment which must be endured by the catalyst. It is therefore important that the catalyst be stable and resistant to corrosion while maintaining a high enough chemical activity to decompose $O_2$ per Equation 2. Furthermore, it is important that the catalyst be noble enough to enable the facile release of the liquid water product as described in Equation 4. This is an important characteristic as it once more avails the catalytic site to reinitiate the process.

This balance of ideal interactions between catalyst and substrate is known as the Sabatier principle and is best represented by the Balandin volcano plot shown in Figure 2.3 (Jaksic et al., 1998). In Figure 2.3 a) the oxygen reduction activity is plotted as a function of its binding energy. From Figure 2.3 a) platinum has the highest activity of all bulk metals, it is also seen that it overshoots the optimum point and binds 0.2 eV too strongly. It is still, however, regarded as the optimum metal in terms of oxygen reduction activity.

With a similar undertaking to the oxygen activity for the hydroxyl reduction activity, Jaksic et al. (1998) and Nørskov et al. (2004), combined the data to produce the plot shown in Figure 2.3 b). The resultant plot motivates the use of Pt in a PEFC as it holds the ideal balance of binding energies of both oxygen and hydroxyl groups. This agrees with literature published by Wu et al. (2020), who mention that Pt was found to facilitate the ORR best by having the ideal balance between its affinity to dissociate oxygen and then hydrogenate it to water.

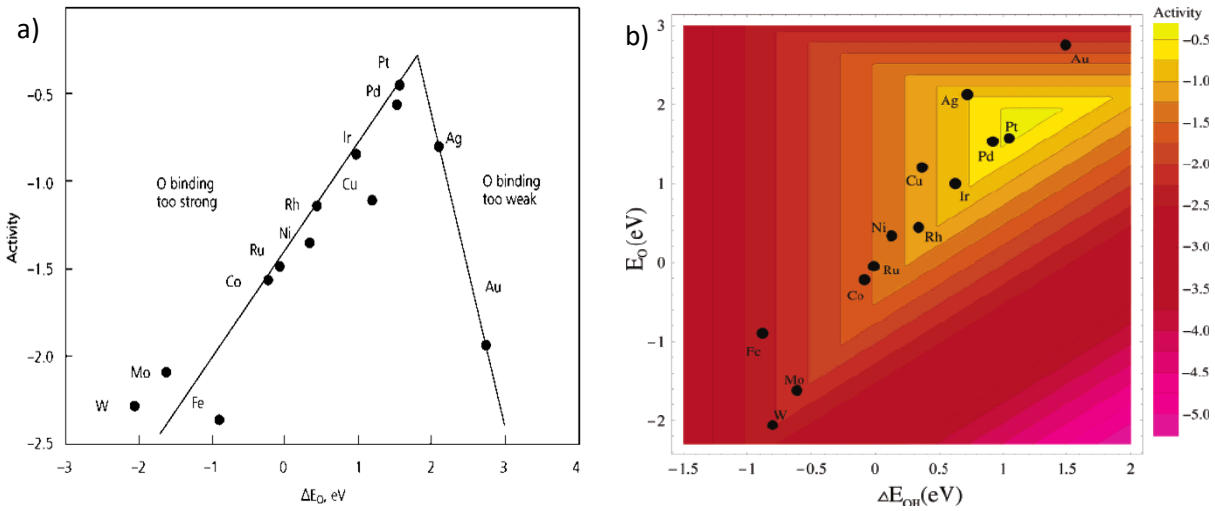


Figure 2.3: a) Oxygen reduction activity plotted as a function of the oxygen binding energy (Jaksic et al., 1998) and b) Oxygen reduction activity as a function of O and OH binding energy (Nørskov et al., 2004).

As important as a catalyst's activity is, so is its selectivity. While it is important to maximize production of a desired product, it is equally as important to limit the production of those undesired. As mentioned, two routes exist for the reduction of oxygen in a PEFC. The alternative mechanism where $O_2$ is adsorbed associatively and then protonated and reduced, results in the formation of $H_2O_2$. The presence of $H_2O_2$ is highly detrimental to the operating environment in the polymer electrolyte fuel cell. Platinum once more when compared to other pure metals, provided the best selectivity with an almost exclusive selection for the dissociate or four electron mechanism (Yuan, Wang & Zhang, 2008).

Furthermore, platinum was also selected as the ideal catalyst based on its thermodynamic stability in the previously mentioned low pH and oxygen rich environment at potentials over 0.9 V – a feature which most noble metals do not possess in their pure forms (Stephens et al., 2012). Due to this characteristic feature, platinum is also less susceptible to dissolution by comparison. Finally, while platinum can be poisoned by carbon oxides, it is neither the most nor the least susceptible to poisoning from impurities such as sulphur containing molecules or carbon monoxide by comparison to other catalysts (Cheng et al., 2007; Sethuraman & Weidner, 2010). It is based on these properties of activity, selectivity, stability, and poisoning resistance which make platinum the ideal candidate for electrocatalytic application in a PEFC.

#### 2.1.4.2 Platinum Alloys and Particle Size Distribution

From the volcano plot shown in Figure 2.3, the optimum binding interaction according to the Sabatier principle is not obtained with pure platinum. Several strategies to further improve the catalyst have been developed amongst which alloying is one of the most known ones. In alloying, a means of cost reduction is also found when cheaper metals forming enhanced properties are utilized.

In a study by Antolini (2009), it was found that by alloying Pt with Palladium (Pd) in a 3:1 atomic ratio, the catalyst provided a higher specific activity than pure Pt for the ORR. Antolini (2009) do, however, also mention that Pt alloy catalysts present larger particle sizes than pure Pt catalysts and because of the resulting decrease in specific surface area, a corresponding decrease in catalytic activity is also exhibited. While other metals such as cobalt (Co), and Iron (Fe), can be seen from Figure 2.3 b) to possess poor activity for the ORR, Antolini (2009) suggest that by alloying either of these metals with Pd, a higher activity than that of pure Pt can be attained. It was also found by Vliet et al. (2011), that alloying 55 wt % Pt with Nickel (Ni), has a mass activity of 2.5 times that of pure Pt for the ORR. While the activity of the catalyst can be manipulated in this manner, it is important to note that the alloy stability is a factor yet to be augmented (Jackson et al., 2017).

The activity and stability of Pt based catalysts is clearly an important aspect in the efficient operation of PEFC's, and in accordance with Wang, Markovic & Stamenkovic (2012), there still exists a lack of understanding of the fundamental properties at the nanoscale. Given the ideal affinity Pt possesses for the ORR in terms of the properties previously mentioned, this study will utilize only pure platinum metal for assessment in the PEFC.

It is generally recognised that noble metals are extremely expensive with Li, Hu, et al. (2015) noting that the Pt cost for a 100 kW PEFC is more than that of an entire power equivalent combustion engine. High metal utilization corresponding to a high electrochemical surface area (ECSA), is therefore a crucial requirement. Given that the active sites of the catalyst are only on its surface, having a bulk catalyst material would serve no additional purpose. It is thus typical that Pt nanoparticles between 2 and 5 nm are uniformly distributed on high surface area catalyst supports (Li, Hu, et al., 2015). With platinum now motivated as a catalyst, an investigation into its support material and its corresponding role in ORR will be investigated.

### 2.1.5 Catalyst Support Considerations

In accordance with Sharma & Pollet (2012), a catalyst support material, by virtue of its durability and activity directly govern a PEFC's electrocatalytic performance. In terms a PEFC's commercial viability, increasing the catalyst support durability will directly decrease the PEFC manufacturing cost (Rabis, Rodriguez & Schmidt, 2012).

#### 2.1.5.1 Current Catalyst Support Properties and Shortcomings

Carbon catalyst supports for the ORR are known to suffer from corrosion due to the low pH and oxygen rich environment which causes their oxidation. They are, however, employed due to their high specific surface areas of ± 250 $m^2\ g^{-1}$, high conductivity's of around ± $10^3$-$10^4$ S $cm^{-1}$, diverse range of morphologies, availability, and relatively low cost (Marinho et al., 2012; Rabis, Rodriguez & Schmidt, 2012; Trogadas, Fuller & Strasser, 2014). In accordance with Li, Hu, et al. (2015), the primary mechanism of the carbon catalyst supports oxidation can be represented by Equation 10.

$$C + 2H_2O \rightarrow CO_2 + 4H^+ + 4e^- \quad (10)$$

This mechanism occurs primarily during a PEFC's shut down/start-up sequencing during which time the potential can spike to 1.5 V. This is considerably higher than the typical operating potential of between 0.6-1.0 V. This drastic surge then increases the rate of irreversible carbon loss at the electrode (Li, Hu, et al., 2015).

Rabis, Rodriguez and Schmidt (2012), motivated the use of carbonaceous supports for potentials below 0.8 V where the kinetics of the carbon oxidation reaction are very sluggish. It is, however, due to the actual start-stop cycles of a PEFC, the shortcomings of the carbonaceous support material is made abundantly evident. In Figure 2.4 a), depicts the desired catalyst support with uniformly distributed Pt nanoparticles.


Figure 2.4: Diagram of catalyst nanoparticles and support material for a) the ideal Pt dispersion on the support material b) Pt dissolution resulting from support corrosion and c) Ostwald ripening via Pt agglomeration on a corroded support.

One of the primary mechanisms of electrochemical surface area (ECSA), reduction is Pt particle detachment at the support surface as shown in Figure 2.4 b). This rate of is seen to increase monotonically between 0.65 and 1.10 V beyond which the formation of an oxide film inhibits further dissolution (Wang et al., 2006). As a result of the platinum dissolution, some catalyst material is lost in the wastewater stream leaving the fuel cell. A portion of the remaining catalyst material then undergoes Ostwald ripening where dissoluted catalyst particles redeposit and form larger particles as shown in Figure 2.4 c). The agglomeration shown in Figure 2.4 c) can also occur without support corrosion through crystallite migration if the platinum anchoring or metal-support interaction is too weak (Nie, Li & Wei, 2015; Ahmad Junaidi et al., 2021).

To increase the lifetime of PEFC's Rabis, Rodriguez and Schmidt (2012), recommended several key aspects for investigation. First, it was suggested to implement a catalyst with a higher oxygen evolution affinity than that of carbon corrosion at the $H_2$ or air front. This concept is, however, limited by mass transport properties. Second, it was suggested to use an anode electrocatalyst with an ability to only oxidize and not reduce oxygen, however, no data on the durability of such a catalyst is known yet to exist. Finally, they recommend an investigation into alternative catalysts supports to eliminate the consequence of corrosion. This project will focus primarily on this: the development of an advanced catalyst support material to increase the durability of a PEFC. To this end, there are specific requirements such an advanced catalyst is to satisfy which are discussed in the following section.

#### 2.1.5.2 Properties of an Ideal Catalyst Support

In accordance with Trogadas, Fuller and Strasser (2014), carbon black is the most utilized carbonaceous support for fuel cells. As described, these supports are susceptible to corrosion. In the pursuit of finding alternative support materials, Rabis, Rodriguez and Schmidt (2012), recommend the following key parameters be considered.

1. The electronic conductivity must be at least equal to 0.1 S $cm^{-1}$ over the typical PEFC operating temperature range (50 - 100 °C). This is sufficiently larger than the proton conductivity of the ionomer at 50 % relative humidity
2. There should exist porous structures with pore sizes of at least 25 nm
3. It should hinder (almost) completely the dissolution of metal cations
4. A Brunauer-Emmett-Teller (BET) surface area of at least 50 $m^2$ $g^{-1}$ is required
5. It is desired although recognisably a challenge, that the material cost less than the currently employed high surface area carbons

Carbon nanotubes (CNT), graphene, inorganic oxides and carbide supports were subjected to investigation in accordance with the above parameters by Sharma and Pollet (2012). These results are summarized in Table 1.

Table 1: Advanced Catalyst Supports Considered for the ORR.

| Type of support | Support properties | ECSA ($m^2$ $g^{-1}$) | Power density (mW $cm^{-2}$) |
|---|---|---|---|
| Carbon nanotubes | $Sp^2$ carbon, hydrophobic, high conductivity, Pt 2-5 nm with 0.04 mg $cm^{-2}$ | - | 595 |
| Graphene | $Sp^2$ carbon sheet, hydrophobic, high conductivity, $10^3$-$10^4$ S $cm^{-1}$ | 45-82 | 390-440 |
| Inorganic Oxides | Semiconductor, high oxidation resistance, Pt nanoparticles between 5 – 30 nm | 32-90 | <90 |
| Inorganic Carbides | Similar catalytic properties to Pt, CO tolerant | 182 | 200 |

While carbon nanotubes and graphene show promising characteristics with respect to their power densities and conductivities, they are still subject to varying degrees of carbon corrosion. Contrary, while inorganic oxides can be seen to have a high corrosion resistance, they require larger Pt nanoparticles which only further increases already high Pt costs (Sharma & Pollet, 2012).

Typically, inorganic carbides, although showing promising activity characteristics are particularly vulnerable to continuous oxidation upon exposure to water and are often not stable at voltages above 0.8 (Sharma & Pollet, 2012). MXene's, however, while still inorganic carbides are said to have an electronic conductivity of up to 5000 S $cm^{-1}$, pore sizes between 15 and 200 nm in diameter, a strong corrosion resistance which should hinder the dissolution of metal cations, and a specific surface area of the sheets of up to 68 $m^2$ $g^{-1}$ (Lipatov et al., 2016; Shahzad et al., 2017; Liu et al., 2018; Maleski et al., 2018). MXene's, and more specifically, $Ti_3C_2T_x$ synthesized from the MAX phase $Ti_3AlC_2$ will therefore be investigated for use as an advanced catalyst support in this project.

## 2.2 MAX Phases

### 2.2.1 Composition and Crystal Structure of MAX Phases

MAX phases are unique in their characteristics and features which exhibit properties of both metallic and ceramic materials. They are generally ductile, thermally, and electrically conductive as well as resistant to oxidation (Ghosh & Harimkar, 2012). MAX phases with $M_{n+1}AX_n$ formula, are ternary layered carbides comprised of an early transitional metal (M), an A-group element (mostly groups 13 and 14) and either a carbon or a nitrogen (X) and with n ranging from 1 to 3. This is represented by Figure 2.5 replicated from Halim (2016), in which the early transitional metal is shown in red, the A-group element in blue, and the C or N in black. MAX phases are the precursors to MXene's and are polycrystalline nanolaminates further known to form laminated structures with anisotropic properties (Yoon et al., 2018).

| H | | M | | | | A | | | X | | | | | | | | He |
|---|---|---|---|---|---|---|---|---|---|---|---|---|---|---|---|---|---|
| Li | Be | Early transition metal | | | | Group A element | | | C and/or N | | | B | C | N | O | F | Ne |
| Na | M | | | | | | | | | | | Al | Si | P | S | Cl | Ar |
| K | Ca | Sc | Ti | V | Cr | Mn | Fe | Co | Ni | Cu | Zn | Ga | Ge | As | Se | Br | Kr |
| Rb | Sr | Y | Zr | Nb | Mo | Tc | Ru | Rh | Pd | Ag | Cd | In | Sn | Sb | Te | I | Xe |
| Cs | Ba | Lu | Hf | Ta | W | Re | Os | Ir | Pt | Au | Hg | Tl | Pb | Bi | Po | At | Rn |
| Fr | Ra | Lr | Rf | Db | Sg | Bh | Hs | Mt | Ds | Rg | Cn | Uut | Fl | Uup | Lv | Uus | Uuo |

Figure 2.5: Periodic Table presenting the elements constituting a MAX Phase (Halim, 2016).

By the many feasible combinations of the transitional metal, A group and C or Nitrogen, it was found that over 60 different MAX phases exist (Liu et al., 2017). Figure 2.6, replicated from studies by (Barsoum & Radovic, 2011), shows that for each hexagonal unit cell, two formula units exist. It can be noted that colours assigned to each atomic species correspond between Figure 2.5 and Figure 2.6.

In Figure 2.6, all unit cells with space group P63/mmc consists of $M_6X$ octahedra corresponding to $Ti_6C$. The unit cells are then interleaved, in accordance with the $M_{n+1}AX_n$ formula, with the appropriate number of A group layers. These A groups layers also act as a mirror plane from which the MX layers are reflected (Eklund, Rosen & Persson, 2017). With A-group elements located at the centre of a trigonal prism, they can accommodate larger elemental species by comparison to an octahedral site location (Barsoum & Radovic, 2011). Further, in Figure 2.6 c), for the 413 MAX phases, two polymorphs exist, α and β (Eklund et al., 2007). For the α polymorph, layering is ABABACBCBC; and for the β polymorph, layering is ABABABABA.

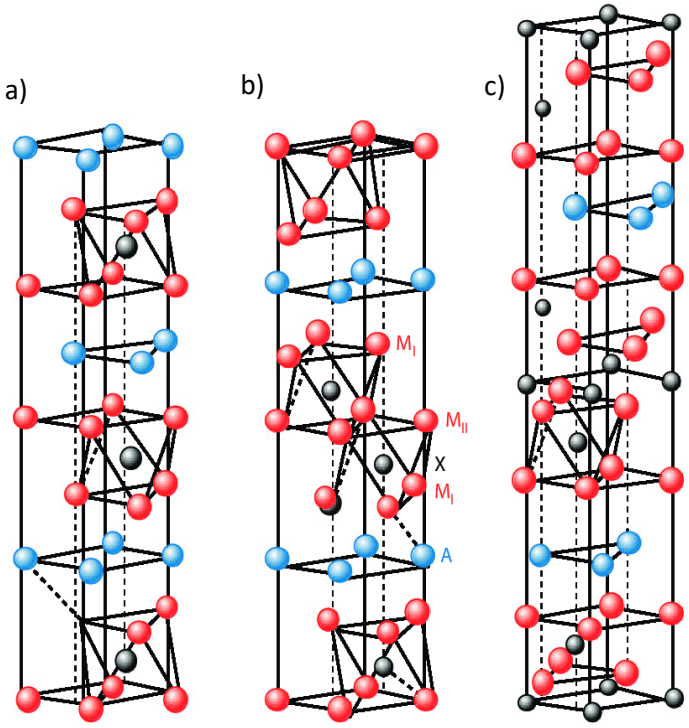


Figure 2.6: Crystalline structure by unit cells for a) 211, b) 312, and c) 413 MAX phases replicated from Barsoum & Radovic (2011).

### 2.2.2 Atomic Bonding within MAX Phases

Bonding within MAX phases is in accordance with Magnuson & Mattesini (2017), made up of a combination of metallic, covalent, and ionic chemical bonds. Further, MX layers are further described by to possess strong covalent bonds originating from the overlap between the *p* and *d* levels of the X and M elements, respectively. A-group elements bound are bound metallically and are by contrast, less strongly bound by comparison to the MX phases. For A-group elements, only their *p* orbitals overlap *d* orbitals of M atoms. This difference in bond strength is what allows the selective etching of A group elements (Li, Wang, et al., 2015; Magnuson & Mattesini, 2017).

## 2.3 MXene's

### 2.3.1 Composition and Crystal Structure of MXene's

MXene's are synthesised by the wet chemical etching of MAX phases and are negatively charged hexagonal, ternary layered carbides (Maleski et al., 2018). They are 2D materials with $M_{n+1}X_nT_x$ formula and have a similar hexagonal structure to their MAX phase precursors. The properties of a MXene such as its structure, lateral flake size, conductivity, capacitance and surface functionalization are all, albeit to varying degrees, a function of its MAX phase (Wei et al., 2021). MXene's are, however, through removal of the A-group found generally to be less prone to oxidation than their MAX phase precursors (Wei et al., 2021).

As mentioned in Section 2.3.2, Naguib et al. (2011) and Magnuson & Mattesini (2017), indicate that the removal of the A-group is possible because it is weaker bound by comparison to MX-groups. After the acid etching of a MAX phase, Alhabeb et al. (2017), suggest the formation of hydrogen and van der Waals bonds to hold the 2D $M_{n+1}X_n$ layers together.

Figure 2.7 a) shows the crystal structure of the etched and terminated MAX phase – now a MXene. As seen in image a) ii) and iv), the distances between the surface Ti layers and the oxygen and fluoride termination groups are 0.88 and 1.23 Å, respectively. This suggests that O terminated with respect to F terminated groups are more strongly bound (Liu & Li, 2019). This difference in bond strength was later found by Liu & Li (2019) to correlate to ORR activity. Figure 2.7 b) shows the SEM image of exfoliated $Ti_3AlC_2$ replicated from Li, Wang, et al. (2015). As seen, by removal of the Al atoms, an accordion-like morphology is obtained. This morphology is desired to simplify the delaminating stage.

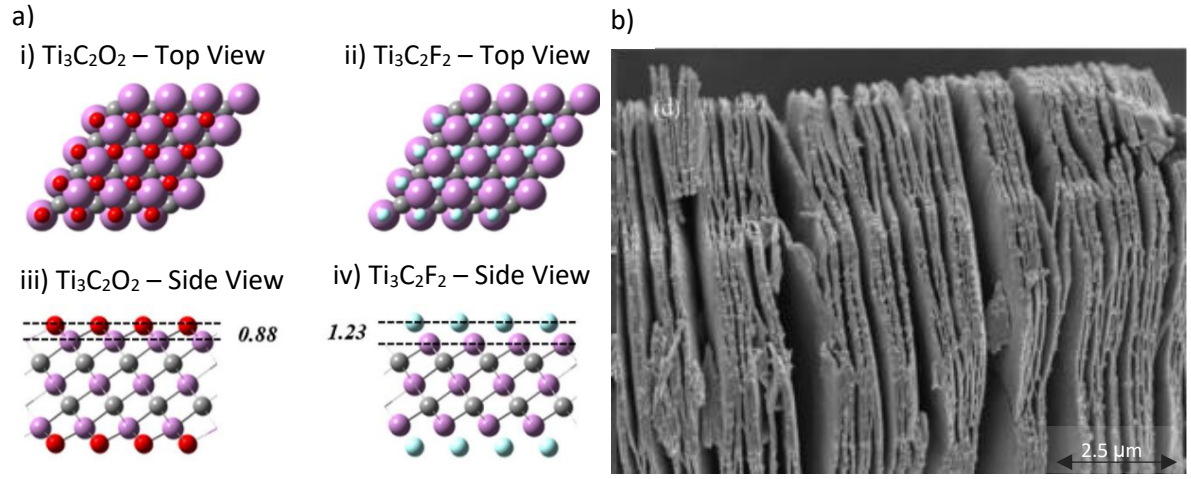


Figure 2.7: a) Etched $Ti_3AlC_2$ Crystal Structure by i), ii) top view and iii), iv) side view with interparticle distances in Å. Ti, C, O and F are shown in purple, grey, red, and cyan, respectively (Liu & Li, 2019) b) SEM image of etched $Ti_3C_2T_x$ etched in 49 wt % HF at 60 °C for 24 hours (Li, Wang, et al., 2015).

As the properties of the MAX phase often extend to the MXene, both material characteristics must therefore be considered in selecting a MAX phase for analysis in this work.

### 2.3.2 MXene Properties as a Function of MAX Phases

Naguib et al. (2011) were the first to synthesize any MXene, however, when Li et al. (2015), later tried replicating their experimental procedure under the same conditions, they could not achieve the same results. The results obtained by Li et al. (2015), were supported by Mashtalir et al. (2013). Li et al. (2015), later attributed the deviation in results to the method in which the MAX phase was prepared which was by either high pressure or pressure less synthesis.

This observation was supported by Alhabeb et al. (2017), who mention that as all MXene's are a function of the MAX phase from which they are derived, the sintering conditions of the precursor may introduce impurities – such as TiC, $Ti_2AlC$ and $Al_2O_3$ – which may further introduce variability to the required etching time. Another important aspect in synthesizing MXene's is the particle size of the MAX phase materials. In accordance with Sinha et al. (2018), this is an important variable in order to accrue high quality and yield MXene's flakes. This is supported by Lei (2015), who mentioned that etching and delaminating parameters are both functions of the MAX phase's particle size. Ultimately, a reduction in starting particle size will reduce the required etching time or required etching concentration (Lei, Zhang & Zhou, 2015).

### 2.3.3 Selection of a $Ti_3AlC_2$ as the Starting MAX Phase

As the properties of the MXene are often like those of its MAX phase precursor as mentioned in Section 2.4.1, it is important to assess all both sets of materials to ensure the best fit for purpose catalyst support is selected. Of the 60 plus MAX phases, $Ti_3AlC_2$ is one of the few shown to possess the suitable electrical and thermal conductivities required for use in a PEFC. This MAX phase also possess among the strongest resistance to oxidation of the many different MAX phases (Wang & Zhou, 2010).

For this MAX phase $Ti_3AlC_2$ used for the synthesis of $Ti_3C_2T_x$, Li, Wang, et al. (2015), investigated the thermal stability and found that between 0 and 200 °C in an oxygen environment, only a 0.38 % weight loss of material was exhibited. It is important to note, that the temperature was elevated at a rate of 15 °C/min with measurements taken as soon as the final temperature had been attained. The 0.38 % weight loss they attributed only to the removal of physically adsorbed water.

Given that a typical operating temperature of a PEFC is around 80 °C, this motivates thermal suitability for the desired application. Lipatov et al. (2016), later considered the propensity of $Ti_3C_2$ flakes to oxidise over a 70-hour period in 50 % relative humidity air. They compared the conductivity before and after air exposure through the fabrication of field effect transistors and their results showed a decrease in conductivity of 18.5 %. However, with a film resistance only a single order of magnitude (versus three for graphene), above that of a single flake, these authors still deemed the results promising for electrocatalytic applications. The variation in resistance between bulk and monolayer flakes was attributed to the resistance perpendicular to the basal plane. This is defined as that contributed toward by contact resistances between individual flakes at their interfaces (Lipatov et al., 2016).

In accordance with Naguib et al. (2011), the resistance of a cold pressed, "thin", $Ti_3C_2$ disc is 0.03 µΩ m. The same authors also determined the elastic modulus along the basal plane of a single $Ti_3C_2$ sheet as 300 GPa. This value is slightly higher than the 250 GPa attained for a chemically derived graphene sheet (Gómez-Navarro, Burghard & Kern, 2008). This means the MXene sheet will be stiffer and less prone to any deformation of its morphology.

It was also predicted by Naguib et al. (2011), that by varying the surface termination groups of the MXene, the electronic structure of the of the layers can be tuned to a desired application. To this end, Lipatov et al. (2016) and Maleski et al. (2018), determined that for a $Ti_3C_2T_x$ sheet with a lateral size of 9 µm, a conductivity of 4600 ± 1100 S $cm^{-1}$ is attained. This significantly surpasses the 0.1 S $cm^{-1}$ requirement outlined by Rabis, Rodriguez & Schmidt (2012), in 2.1.5.2. Based on the desired properties of the $Ti_3C_2T_x$ MXene discussed, its corresponding 312-$Ti_3AlC_2$ MAX phase has been selected for analysis. Shown in Figure 2.8, is the SEM images of $Ti_3AlC_2$ at different magnifications a) and b). These images present the physical morphology and layered structure relating to the crystal structure described in Figure 2.6.

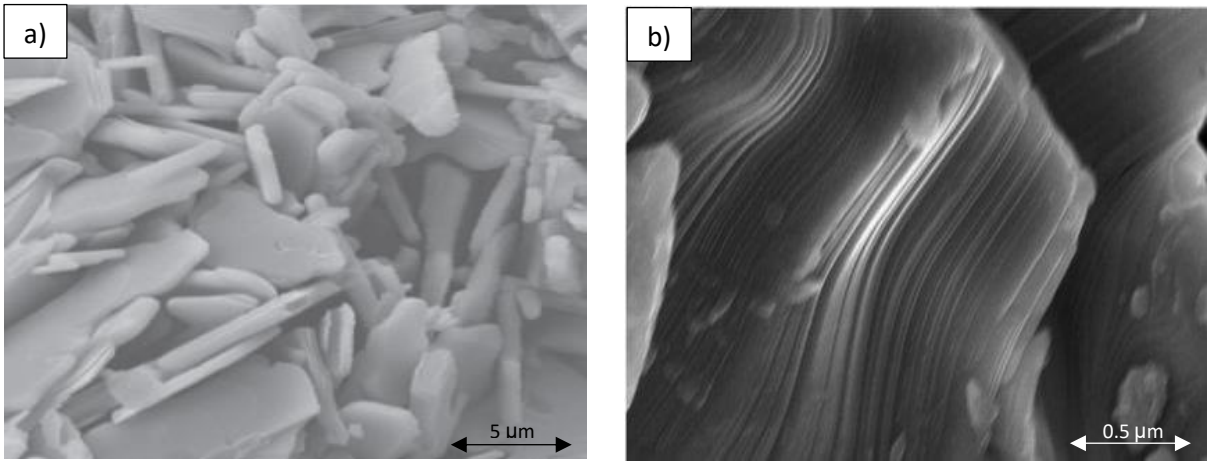


Figure 2.8: SEM images of $Ti_3AlC_2$ depicting the layered structure of the MAX phase replicated from a) Zhou (2012) and b) Koyappayil & Chavan (2020).

Regali et al. (2014), found that the properties inherent within the $Ti_3C_2T_x$ MXene's surface terminations can potentially aid in increasing surface activity towards the oxygen reduction reaction. Further, with a high resistance to corrosion, $Ti_3C_2T_x$ may more importantly also offer a longer lasting catalyst support. If proven successful, the increase in surface activity would also mean less Pt will be required for the same performance.

### 2.3.4 Synthesis of $Ti_3C_2T_x$ Through the Selective Etching of $Ti_3AlC_2$

#### 2.3.4.1 Using Hydrofluoric Acid

In accordance with Naguib et al. (2011), the selective wet etching of the A-group with In-situ hydrofluoric acid (HF), creates an active site for termination ($T_x$), by a surface group (typically -OH or -F). These surface terminations, in accordance with Maleski et al. (2018), are responsible for the MXene's hydrophilic nature and also render them capable of solution processing. As described in Section 2.3.1 Li, Wang, et al. (2015) and Magnuson & Mattesini (2017), mention that A-group elements are weakly bound by comparison to the $M_{n+1}X_n$ layers which allows for this selective etching. In accordance with Naguib et al. (2011), the following three simplified reactions take place with $Ti_3Al_2C$ and hydrofluoric acid in the aqueous etching solution:

$$Ti_3AlC_2 + 3HF \rightarrow AlF_3 + 3/2H_2 + Ti_3C_2 \quad (11)$$

$$Ti_3C_2 + 2H_2O \rightarrow Ti_3C_2(OH)_2 + H_2 \quad (12)$$

$$Ti_3C_2 + 2HF \rightarrow Ti_3C_2F_2 + H_2 \quad (13)$$

The Equations (11-13), were validated using density function theory (DFT), based geometry optimizations. Equation 11 is the most essential and allows either Equation 12 or 13 to proceed. During the first reaction there is a loss of metallic bonding because of the etched-out Al atoms. As a result, $Ti_3C_2$ layers are etched from one another. After exfoliation, each unit formula has two Ti atoms exposed and requires suitable ligands for satisfaction to an equilibrium charge. Given that the experiment typically occurs in an aqueous solution rich in fluorine and hydroxyl ions, these are the resulting termination groups. It is worth noting that there will be a combination of Equations 12 and 13 occurring and they are not satisfied independently (Naguib et al., 2011).

For hydrofluoric acid (HF), etching, Naguib et al. (2011), who discovered MXene's first etched $Ti_3AlC_2$ in a 50 wt % HF solution at room temperature for 2 hours. More recently, however, Li et al. (2015) suggest etching in a 49 wt % HF solution at 60 °C for 24 hours. It was further noted by Li, Wang, et al. (2015), that exfoliating at a temperature of less than 60 °C, significantly increases the required etching time and at 0 °C, regardless of the HF concertation, at least 72 hours will be required to initiate exfoliation. Alhabeb et al. (2017), discussed the variability in etching time and found that at room temperature, exfoliating in a 5 wt % HF solution for 72 hours removes the same amount of Al as that of a 30 wt % solution for 18 hours. There was, however, a large discrepancy in morphologies with only the 30 wt % HF solution providing the accordion like structure shown in Figure 2.7 b). These authors also found that MXene powder exfoliated from the lower concentration solution would hardly be distinguishable from that of the MAX phase powder. This was attributed to the limitation imposed on the exothermic kinetics of the HF reaction with Al.

Consequently, it was found that a decrease in the amount of $H_2$ escaping (Equations 12 and 13), hinders transformation to the desired accordion like morphology (Li, Wang, et al., 2015). It is thus desired to exfoliate MAX phases in both higher concentrated HF solutions as well as temperatures.

#### 2.3.4.2 Using in-situ Hydrofluoric Acid

The in-situ hydrofluoric acid method was developed to decrease the reliance on hazardous HF. Further it was found that while all HF methods require further processing for delamination following exfoliation, using a specific in-situ HF method, eliminates the need for secondary processing. This methodology also allows larger flakes with cleaner edges to be produced (Liu et al., 2017). All Equations 11-13 remain the same but are preceded by Equation 14 where the HF is formed from a reaction between LiF and HCl.

$$LiF + HCl \rightarrow LiCl + HF \quad (14)$$

Several parameters such as HCl volume and concentration, HCl:LiF molarity, temperature and time have been evaluated by various authors for the optimization of in-situ HF etching methods (Lipatov et al., 2016; Alhabeb et al., 2017; Liu et al., 2017). Lipatov et al. (2016), took the approach of etching using an approximate 2:1 HCl:LiF ratio in 10 ml of etchant at 35 °C for 24 hours. By contrast, Liu et al. (2017), etched using a 3:1 HCl:LiF ratio in 20 ml of etchant at a temperature of 60 °C for 24 hours. The method and conditions outlined by Lipatov et al. (2016), is known as the minimally intensive later delamination (MILD) method. With an excess of $Li^+$ ions in solution, intercalation is facilitated in the etching solution using this method. Alhabeb et al. (2017), motivated MILD application in environments where high electrical conductivity and environmental stability are favoured. They do, however, suggest the use of alternate methods where smaller more defective sheets are required such as in the case of electrochemical applications. It should be noted, however, that Maleski et al. (2018), showed that while smaller particles possess a higher specific surface area, they are less conductive than their larger counterparts. There is therefore a trade-off between specific surface area and conductivity when considering electrochemical applications.

### 2.3.5 Delamination of $Ti_3C_2T_x$ Flakes

The desired catalyst properties for an ORR catalyst as per Section 2.1.4 is 2 to 5 nm Pt particles uniformly distributed on a support possessing a specific surface area of at least 50 $m^2\ g^{-1}$ (Rabis, Rodriguez & Schmidt, 2012). It is also imperative that the support possess a specific area to achieve the desired loading of Pt with a coverage of around 0.4 mg $cm^{-2}_{geometric}$ loading (Stephens et al., 2012). Shahzad et al. (2017), indicate that multi layered $Ti_3C_2$ sheets only possess a specific surface area of 0.5 $m^2\ g^{-1}$. By contrast, the specific surface area of delaminated $Ti_3C_2$ sheets is up to 68 $m^2\ g^{-1}$.

It is therefore vital that exfoliated sheets be delaminated to attain the SSA requirement outlined in section 2.1.5.2 by Rabis, Rodriguez & Schmidt (2012). Delamination of MXene's can be undertaken through either sonicating methods or chemical intercalant methods.

#### 2.3.5.1 Sonication as a Means of Delaminating $Ti_3AlC_2$ Flakes

As mentioned in Section 2.3.4.2, in-situ HF etching with the ideal set of parameters, requires no secondary delamination stage. This section therefore relates specifically to the treatment of post HF etched MXene's.

Sonication, in accordance with Maleski et al. (2018), is a very strong function of the etching parameters. While sonication was only used by other researchers as a means of delaminating flakes, Maleski et al. (2018) used it, in conjunction with density gradient centrifugation to determine which 2D MXene flake sizes, in a delaminated colloidal solution with large lateral-size polydispersity, are responsible for key conductivity properties. They found that by varying the input energy, sonication can also be used as a means for selectively controlling the flake size. This agrees with previous literature by Alhabeb et al. (2017), who stated that longer sonicating times with higher powers are responsible for smaller, more defective flakes. As discussed, for catalytic applications it was recommended to make use of smaller flakes to increase electrochemical performance. This was further motivated by Maleski et al. (2018) who determined that smaller flake sizes can provide more active sites for deposition, which in turn enables better electrolyte accessibility leading to an increase in electrochemical performance. Maleski et al. (2018) noted that flakes with a lateral size of ±1 µm show the best capacitance and rate performance of flakes between 0.1 and 5 µm and that conductivity is inversely proportional to lateral flake size. The transformation of the crystalline structure from MAX phase to MXene pre and post sonication, is shown in Figure 2.9 replicated from Naguib et al. (2011).

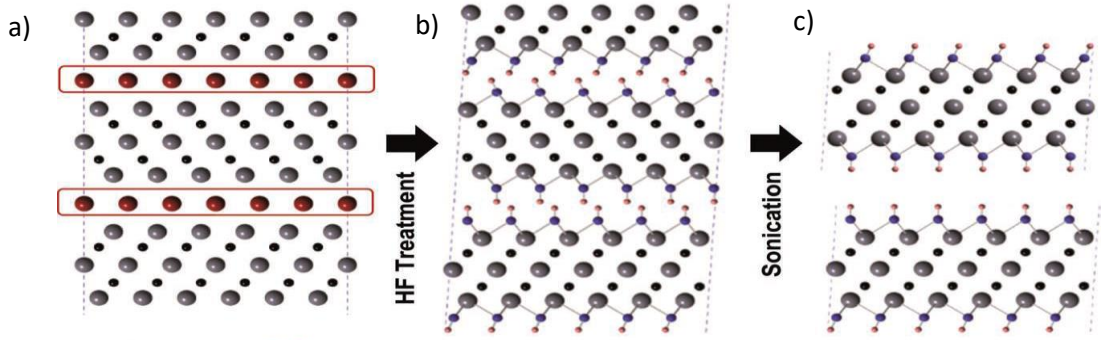


Figure 2.9: Crystal structure transformation from a) MAX phase to MXene b) pre and c) post sonication adapted from Naguib et al. (2011). Ti, C, Al, O and H are shown in grey, black, red, blue and pink, respsectively.

#### 2.3.5.2 Intercalation as a Means of Delaminating Ti3AlC2 Flakes

Li, Wang, et al. (2015), found that the spacing between atomic planes (or d-spacing) of layered MXene flakes can be increased using intercalating compounds. This step could be achieved by weakening interactions between the 2D layers and consequently, separating or delaminating them. Intercalation of MXene's takes place in a suitable solvent for both the multi-layered sheets and the intercalant. Several intercalants have been studied to delaminate MXene's, each with their own advantages and disadvantages. Dimethyl sulfoxide (DMSO) was among the first of these investigated. This intercalant does, however, require that sonication follows. Without sonication the multi-layered sheets would settle as sediment. Intercalating with DMSO will provide a lateral flake size, after sonicating, of the order of a few hundred nanometers (Alhabeb et al., 2017). When obtaining diffractogram results, each peak corresponds to an individual d-space. As a result of the intercalation, it is therefore expected that the XRD peaks will be shifted. This was confirmed by Li, Wang, et al. (2015), who mention that the MXene peaks after intercalation with DMSO were shifted to a lower angle and broadened. The broadening they attributed to an increase in d-spacing and a decrease in the thickness of the sheet layers.

Another intercalant investigated was urea. It was found by Li, Wang, et al. (2015), that while intercalation with $CH_4N_2O$ at 60 °C for 24 hours increased the physical unit cells dimensions – or c lattice parameter (LP c) – from 19.853 to 25.108 Å, the MXene characteristic peaks were sharpened. This meant urea molecules diffused into the crystal planes and glued the layers together resulting in an increase in thickness of the layers.

A final consideration for intercalation is with $Li^+$ ions in hydrochloric acid (HCl). The exfoliation parameters of $Ti_3AlC_2$ using LiF, NaF, KF and $NH_4F$ salts were investigated by Liu et al. (2017). They reported that of all the species tested, LiF performed most desirably and provided the most delaminated sheets. This corresponds to what was previously mentioned in Section 2.3.4.2, where MXene synthesis using the MILD method, due to the excess of $Li^+$ ions and sufficiently concentrated HCl, provided etched and delaminated sheets in a single stage.

## 2.4 Electrochemical Performance Evaluation

### 2.4.1 Platinum Deposition

Many methods of depositing Pt to a support exist with different advantages and disadvantages. The methods evaluated for use in this project include polyol, wet chemistry, spray coating and metal-organic chemical deposition (Li & Hsing, 2006; Jackson et al., 2017; Palma et al., 2018).

The first two investigated methods of polyol (or ethylene glycol reduction) and wet chemistry (or borohydride reduction), while most commonly employed are disadvantaged by their long preparation times of up to 40 hours (Huang, Ganesan & Popov, 2010; Lv et al., 2010). Furthermore, Castillo et al. (2018), have found that while electrospray methods can achieve above 90 % deposition into pores, Pt nanoparticles formed from electro sprayed droplets are found to agglomerate at the support surface.

Studies conducted by Gertzen & Moydien (2017) & Jackson et al. (2017) on metal organic chemical deposition (MOCD), showed favourable results in depositing well dispersed, platinum nanoparticles between 2 and 6 nm onto a carbide support material in 10 hours. Based on its ease of application, time efficiency and application to carbides, MOCD was selected for use in this project.

### 2.4.2 Electrochemical Surface Area Measurements

To assess whether the MXene-based support outperforms its carbon alternative in terms of both durability while maintaining similar activity, an electrochemical performance evaluation was to be conducted. The protocols used in this report are those scientifically standard and typically employed by Hydrogen SA (HySA). These protocols involve the preparation of an ink containing catalyst dropped and uniformly dispersed over a polished glassy carbon electrode. It was shown by Kocha et al. (2017), that both the magnitude of the measured ORR activity and the ability to achieve consistent results is a function of system cleanliness. Consequently, glassware was regularly cleaned. Much like system cleanliness, Kocha et al. (2017), also show that both the magnitude of the measured ORR activity and the ability to achieve consistent results is a function of both ink formulation along with film drying. To achieve the desired consistency, both respects were kept routine as discussed in section 4.4. Following the ORR measurements, the charge under the hydrogen potential region between approximately 0.05 and 0.40 V (vs RHE), shown in Figure 5.28 was related to an electrochemical surface area (ECSA). Using 210 μC $cm^{-2}$ as the charge for the adsorption of an atomic monolayer of hydrogen in the acid electrolyte (Garsany et al., 2014), Equation 15 was used to calculate the ECSA.

$$ECSA\ \left(\frac{cm^2}{gPt}\right) = \frac{Charge\left(\frac{\mu C}{cm^2}\right)}{210\left(\frac{\mu C}{cm^2}\right)\cdot Pt\ loading\left(\frac{gPt}{cm^2}\right)} \quad (15)$$

In accordance with Garsany et al. (2014), electrocatalytic activity measurements should be reported area and mass specifically at 1600 rpm and at 0.90 V vs RHE. Before reporting, corrections to the voltage and current are required to remove the effects of impedance and acquire the corrected ORR polarization curves. Equation 16 shows the Equation of the mass transport corrected current:

$$I_k = \frac{I_{lim}\cdot I}{I_{lim}-I} \quad (16)$$

In Equation 16, $I_{lim}$ is the limiting current, and I, the current measured at a potential of 0.90 V vs RHE.

The final Equation to model the solution and diffusion flow conditions around a rotating disk electrode, is the Levich Equation 17. All variables are as described in the nomenclature.

$$i_L = (0.620)nFAD^{2/3}\omega^{1/2}\nu^{-1/6}C \quad (17)$$

## 2.5 Rationale and Sustainable Development Goals

### 2.5.1 Rationale of the Study

From literature, high surface area carbon supports and particularly carbon black, is often employed to facilitate the ORR in PEFC's. Platinum use in the fuel cell was motivated and the carbonaceous catalyst support found to be employed due to its high specific area, diverse range of morphologies and low cost. The supports were, however, found to be susceptible to two mechanisms of electrochemical surface area reduction. First, they are vulnerable to oxidation and secondly, due to its instability, platinum dissolution, agglomeration and Ostwald ripening are also possibilities. The ECSA loss is a consequence of the low pH, start-up potentials and, the oxygen rich environment under which the supports are subjected to. By consequence of these conditions, a decrease in the PEFC's operating efficiency and durability are observed.

With their structural properties combining the advantages of both metallic conductivity and ceramic corrosion resistance, MXene's possess the potential to replace carbon catalyst supports for the ORR. $Ti_3C_2T_x$, was the selected MXene for this analysis as it offers a theoretically higher surface activity based on its termination groups than the currently employed carbonaceous supports. Further, it may also offer a more durable, longer lasting catalyst support, based on its acid and oxidation resistance at PEFC operating conditions. The overall aim of the project will therefore be to determine if $Ti_3C_2T_x$ can offer a more durable support with a similar level of activity to carbon black for the ORR in a PEFC.

### 2.5.2 Sustainable Development Goals

To restrict global warming to at least 1.5 °C, it has been determined by the IPCC (2018), that low emission final energy fuels in the transport sector will need to rise to around 10 times its current market share value of 5 %. To achieve this, PEFC's will be required to reach the 5000-hour lifetime target for transport applicable fuel cells set by the DoE of the U.S (Majlan et al., 2018).

With current catalyst supports restricting the lifespan to 1700-hours, the development of more durable supports is crucial. This research, which focuses on the potential of MXene's to help realize the durability targets, contributes toward sustainable development goals relating to cleaner energy and more sustainable communities.

# Chapter Three: Hypothesis and Key Questions

## 3.1 Hypothesis

Based on the literature in Chapter Two and the context of this study, it is hypothesised that:

By exfoliating $Ti_3AlC_2$ with in-situ HF or HF methods followed by sonication, it will be possible to attain, high (>50 $m^2 g^{-1}$), specific surface area, delaminated $Ti_3C_2T_x$ sheets. Further, the as synthesized $Ti_3C_2T_x$ sheets will provide a more durable catalyst support for Pt enabling a similar level of activity to that of carbon black.

## 3.2 Key Questions

The key questions derived from the hypothesis are as:

- Is it possible to attain high (>50 $m^2 g^{-1}$) specific surface area, delaminated, $Ti_3C_2T_x$ sheets by exfoliating $Ti_3AlC_2$ with either in-situ HF or HF methods followed by sonication?
- Does the $Ti_3C_2T_x$ catalyst support outperform the commercial carbon black in the electrochemical environment of a PEFC for the ORR in terms of durability while maintaining similar activity?

# Chapter Four: Research Approach

## 4.1 Experimental System

As the starting particle size and sintering conditions of $Ti_3AlC_2$ impact the synthesised MXene, a single source with as few batches as possible of starting material will be used to eliminate inconsistencies on the product properties (Wei et al., 2021). To this end, three batches of MAX phases ordered from Changsha Easchem Co were used in this report. All three batches were synthesised using the same materials and under the same conditions. The attained MAX phases were listed as 98 % pure with batches one and two having a maximum stipulated lateral particle size of below 74 μm, and batch three 37 μm. The only variation between the synthesis methods of the first two batches and the third, was the final grinding and sieving which was through a smaller sized screen of 400 vs 200-mesh.

Due to company confidentiality, Changsha Easchem Co. were only able to provide the outlining synthesis condition of hot pressing (HP). The alternative to hot pressing is pressure-less synthesis (PLS). Through the variation in starting material synthesis methods, a differential in the degree of preferred orientation is introduced into the derived MXene (Kuo & Shen, 2000; Li, Wang, et al., 2015). Whereas pressure-less synthesis derived MXene's are highly orientated, those synthesised from a hot-pressed MAX phase are relatively lesser so. As a result, when Li et al. (2015), recorded XRD diffractogram's of the MXene's synthesized under the same conditions but using differently synthesised MAX phases, they found significantly greater intensity in the peak intensity from the PLS samples. Li et al. (2015) compared the XRD diffractograms between PLS and HP synthesised MAX phases and while there are subtle differences in peak intensities, they share the same pattern.

Only $Ti_3AlC_2$ has been selected for this investigation based on its corresponding MXene's electronic and thermal conductivities, as well as its oxidant resistant properties. Further, all synthesis routes investigated will be at the mildest possible conditions as described in Chapter One due to safety concerns.

## 4.2 MXene Synthesis Parameters

For the exfoliation and where applicable, delamination, of the MAX phase, $Ti_3AlC_2$, the following protocols were performed for in-situ HF and HF acid etching, respectively. It can be noted that irrespective of the etchant, all etching took place on an IMIUTP-350+ EA Digital magnetic stirrer hotplate with the associated support rod and temperature probe.

The temperature probe was always placed in a silica oil bath with a magnetic stirrer and stirred at 350 RPM. The beaker containing the etching solution was then placed three quarter way into the bath.

### 4.2.1 In-situ HF Etching

By performing in-situ HF etching with the HCl:LiF molar ratio herewith reported, it was possible to etch and delaminate in a single step, thus negating the need to use either intercalants or sonication.

To etch using this method, the etching solution was prepared by adding a weighed amount of LiF to the 10 ml 10 M HCl. The solution was left under continuous stirring at 300 RPM using a magnetic Teflon bar for 5 minutes. Where a specific HCl molarity was required, the acid would be added to a known volume of deionized water to a total etchant volume of 10 ml. Where changes to the etchant concentration was made, stirring was performed for 5 minutes before proceeding with the synthesis. 0.5 g of $Ti_3AlC_2$ powder was added to the prepared etchant over the course of 5 minutes as the reaction of aluminium with HF acid is exothermic. If the MAX phase powder was not added gradually into the etching solution, bubbling and a temperature spike would occur. The reaction was then left to continue at the desired temperature and for the desired time. Once the reaction was completed, the MXene flakes in solution were placed into a polyethylene beaker with 500 ml of deionized (D.I), water and allowed to settle overnight. With this quantity of D.I water, the resultant pH was reduced to within the desired 4-5 range. Once the MXene powder had settled from solution, the surface water was decanted and safely disposed of. The MXene concentrate was then placed into a 200 ml polyethylene beaker which was placed into an oven at 60 °C and allowed to dry before characterisation was conducted in accordance with Section 4.5 to follow.

### 4.2.2 HF Acid Etching

The HF etching solution was prepared measuring out 10 ml of 48 wt % as received hydrofluoric acid. Where a lower assay than provided was required, the HF acid would be added to a known volume of deionized water and brought to a total etchant volume of 10 ml corresponding to the desired molarity. Where changes to the etchant concentration was made, stirring was performed for 5 minutes before proceeding with the synthesis. 0.5 g of $Ti_3AlC_2$ powder was then added to the prepared etchant over the course of 5 minutes as again, the reaction of aluminium with HF is exothermic. The reaction was then left to continue at the desired temperature and for the desired time. Once the reaction was completed, the MXene in solution was placed into a polyethylene beaker with 1-litre of deionized water and allowed to settle overnight. This was repeated to bring the total wash water to a volume of 2-litres over two days.

Where vacuum filtration was desired to allow for a shorter period between synthesis and characterisation, the 1-litre of dispersed flakes was vacuum filtered. The slurry was then redispersed, and the process repeated. Vacuum filtration was performed using an N840 diaphragm pump with quantitative grade 390 filter paper. With the quantity of D.I water mentioned above, the resultant pH was reduced to the desired 4-5 range. Once the MXene powder had settled from solution, the surface water was decanted (and the slurry collected). The MXene concentrate was then placed into a 200 ml polyethylene beaker which was placed into an oven at 60 °C and allowed to dry.

Where grinding by mortar and pestle was required, the dried MXene powder would be ground by the same individual for exactly 10 minutes. As much as possible, this process was attempted to maintain uniformity in terms of the applied force. Where grinding by micronizor was required, the dried MXene flakes were placed into a McCrone Micronizing Mill along with the grinding media for exactly 10 minutes. To remove the flakes from the media and mill, deionized wash water was used. The quantity of D.I water was kept to a minimum to not extend the secondary drying process which would take place in the same oven at 60 °C.

Where sonication was required, it was performed by dispersing 200 mg of dried MXene powder in 50 ml of deionized water. Sonication was performed in a plastic beaker using an SMSC-8801 probe sonicator at 100 % power with a 1s on, 1 s off frequency. This process was done over various time ranges all of which were undertaken in an ice bath. Once more, the sample was placed into an oven at 60 °C and allowed to dry before characterisation was conducted in accordance with Section 4.5.

## 4.3 Platinum Deposition

As discussed in Section 2.4.1, platinum deposition was be carried out by metal organic chemical deposition. The protocols were as follows. First, BET specific surface area results were used to determine the amount of the precursor material (97 %, platinum acetoacetate or $Pt(acac)_2$), to achieve a desired particle dispersion. The platinum precursor was then placed alongside the MXene flakes in a vial in an ultrasonic bath for 30 minutes. The mixed catalyst precursor and support material were then placed in a reactor and into a tube furnace. Argon gas was slowly passed through the reactor to remove surface contaminants as the furnace ramped from 0° to 100 °C at a rate of 3.3 °C/ min or over half an hour. The temperature was then held at 100 °C for 30 more minutes. Over the next hour, the reactor ends were closed with a saturated argon atmosphere inside. The furnace temperature was then ramped from 100 °C to 350 °C at a rate of 4.2 °C or over an hour. After maintaining a temperature of 350 °C for 2 more hours, the catalyst deposition was complete.

## 4.4 Electrochemical Performance Evaluation

To assess whether the MXene-based support outperforms its carbon alternative in terms of both activity and/or durability, an electrochemical performance evaluation was conducted in accordance with the below.

### 4.4.1 Electrode and Catalyst Ink Preparation

The following protocols were strictly employed to ensure consistency of results as per Section 2.4.2. A glassy carbon electrode sheathed in Teflon (A = 0.196 $cm^2$ with Ø = 5 mm, Pine Instruments), was polished on a moistened polishing cloth to a mirror-finish. Polishing was completed in three cycles using milli-pure water and decreasing particle sizes 1 to 0.03 µm of $Al_2O_3$. The electrode was placed in a beaker of milli-pure water and bath sonicated for 5 minutes before being left to dry. The catalyst ink was then formulated using HySA's internally developed protocols for Pt/C. For Pt/MXene, the same volume of ink to retain the same dispersion was used, however, the ink formulation was adapted from Faraji, Parsaee & Kheirmand (2021). The ink composition was as follows:

- The platinum/carbon ink solution consisted of 5 mg catalyst, 5 ml milli-pure water, 1.5 ml isopropanol alcohol and 25 µl of Nafion 5 wt % solution
- The platinum/MXene ink solution consisted of 5 mg catalyst, 6.5 ml of anhydrous ethanol and 25 µl of Nafion 5 wt % solution

Following the ink formulation, all inks were bath sonicated for 30 minutes to create a homogenous catalyst suspension. In all instances, 10 µl of ink was dropped onto the surface of the glassy carbon electrode and dried by attaching it to an upward facing shaft rotated at 700 RPM. Garsany, Singer & Swider-lyons (2011), have shown that this method of ink drying produces more reproducible and smooth films than allowing it to air dry.

### 4.4.2 Electrochemical System Configuration

All electrochemical measurements were performed using a standard three-compartment, glass, electrochemical cell. The electrolyte solution was 0.10 M $HClO_4$ and was de-oxygenated by bubbling through argon gas for at least 30 minutes before experiments were initiated. The working glassy carbon electrode was attached to the electrode rotator and guided into the electrolyte ensuring that no argon bubbles contacted its surface. For the counter electrode, a platinum wire was used, and all potentials were measured against a reversible hydrogen electrode (RHE), which was sealed and bridged using the same electrolyte (0.10 M $HClO_4$). For consistency, the height of the working electrode and by virtue the resistance of the solution between the working and RHE were kept as constant as possible.

All electrodes were then connected via the same channel to the Bio-Logic SP-300, potentiostat. This was done with shielded cables with the same channel always used as to retain the specific calibration parameters. Finally, the results from all experiments were analysed using EC-Lab.

### 4.4.3 Electrochemical Surface Area and Activity Parameters

To measure the electrochemical surface activity (ECSA), following the system configuration as above, the working electrode was cycled at 100 mV $s^{-1}$ from 0.05 to 1.20 V for 50 cycles to remove contaminants and clean the electrode surface. Five cyclic voltammograms (CV's), were then recorded over the same potentials at a scan rate of 50 mV $s^{-1}$ for calculation of the ECSA in accordance with Equation 15 mentioned in Section 2.4.2. Activity measurements for catalysts were determined by performing linear sweep voltammetry (LSV). For background corrections, recordings were done in an argon purged electrolyte. At a scan rate of 20 mV $s^{-1}$, the potential was varied from 1.00 V to 0.02 V, before being reversed from 0.02 V back to 1.00 V. This was conducted at four rotational speeds of 400, 900, 1600 and 2500 RPM to attain a full set of polarization curves. These background measurements were significant as they were required to eliminate capacitive current contributions for platinum oxidation and reduction. Additional background corrections included an impedance measurement that was recording using the software integrated in EC-Lab. This impedance resistance was later used for voltage corrections and was assumed constant throughout the experiment. Finally, the electrolyte was saturated in oxygen and the same LSV parameters used for further measurements. After correcting the voltage for the impedance, the difference between the current from the argon and oxygen polarisation curves can be related to the activity of the catalyst.

### 4.4.4 Accelerated Durability Testing Parameters

The parameters for the catalyst degradation assessment were adapted from Jackson et al. (2017). After initial ECSA measurements, scans at 50 mV $s^{-1}$ by cycling between 0.6 and 1.0 V vs RHE were performed for up to 5000 cycles. At select intervals, the scan rate was changed to 100 mV $s^{-1}$ and cycled between 0.01 and 1.2 V for 50 cycles to remove surface contaminants. Following, the scan rate was reverted to 50 mV $s^{-1}$ and a revised CV recorded before resuming cycling between 0.6 and 1.0 V vs RHE.

## 4.5 MXene Characterisation

To ensure analyse the results, the following characterisation protocols were strictly performed for all samples and starting materials under the same conditions.

For analysis of the morphology and structure of both the $Ti_3AlC_2$ MAX phases and $Ti_3C_2T_x$ MXene flakes, scanning electron microscopy (SEM), transmission electron microscopy (TEM), and X-ray diffraction (XRD), were performed. For only the MAX phases, Raman spectroscopy (RS), was also performed to confirm the chemical composition. In this project, a Tescan MIRA SEM utilizing a backscatter detector was used for the capturing of SEM images such as those shown in Figure 5.2. To identify the elemental composition and specifically, the location of such elements, energy dispersive spectroscopy (EDS) was used and performed using a Nova Nano SEM with an Oxford X-MAX 20 $mm^2$ detector. For catalyst particle size and dispersion analysis, TEM was performed using an FEI Tecnai F20 field emission cryo-TEM. Image J was used to analyse TEM images and provide the particle size distributions. The last characterisation method for chemical composition was RS which was performed using a Witec Confocal Raman Microscope (Alpha 300).

To assess the specific surface area of etched and or delaminated $Ti_3C_2T_x$ flakes, the Brunauer-Emmett-Teller (BET) measurement technique was utilized. The information was collected using a physisorption analysis performed on a Micromertics Tristar ll 3020. All samples were degassed at 200 °C for 3 hours with nitrogen used as the adsorbate and helium employed for determining the void volume of the sample tube.

To determine composition and lattice parameters, powder X-ray diffraction (XRD) was utilized. In this work, measurements were recorded using a Bruker D8 diffractometer utilizing Co Kα radiation and analysed using Diffrac.Suite. The step sizes were constant at 0.02° with 1 s dwelling time and powders placed on holders rotated throughout the analysis to improve particle statistics. Lastly, samples were pressed into the holders to increase peak intensity using a glass slide.

# Chapter Five: Results

The following Section reviews the results of the study. As mentioned in Chapter One, all methods applied were at the mildest possible conditions to attain the desired MXene properties. The results in this work are discussed in three Sections where $Ti_3AlC_2$ powder is first characterised by batch and particle size. Following, the transformation from this MAX phase powder to MXene flakes with a high (>50 $m^2$ $g^{-1}$), specific surface is documented. Finally, the synthesized $Ti_3C_2T_x$ flakes were electrochemically assessed for application as a catalyst support material to facilitate the ORR in terms of activity and durability.

## 5.1 MAX Phase Material Characterization by Batch

The XRD diffractogram for the starting materials is shown in Figure 5.1. As seen, primary peaks are observed at 11.04°, 22.33°, 39.69°, 43.00°, 45.61°, 48.94°, 56.97°, 61.69° and 66.68°. After correcting for the different x-ray sources, agrees with Zhao et al. (2016) who also designated the peaks to planes (002), (004), (101), (103), (104), (105), (107), (108), and (109) respectively. The correction was required as the literature values were measured using a Cu radiation source vs cobalt in this report. The corrections were completed using Braggs Laws.

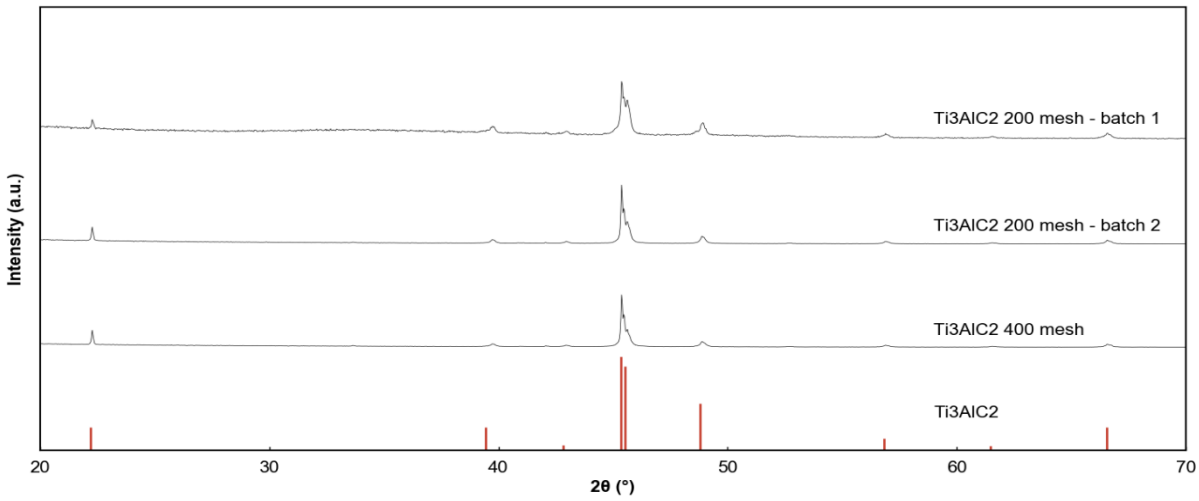


Figure 5.1: XRD of $Ti_3AlC_2$ MAX phases synthesized by hot pressing as sourced from Easchem Co. Diffractogram is shown first by batch number and then particle size of 200 and 400-mesh, respectively, against the reference pattern of $Ti_3AlC_2$.

As shown in Figure 5.1 in red, all reference peaks align with literature. The low intensity peak at 52.65°, corresponding to plane (106), is not visible after normalizing, however, does exist in the original spectrum.

In accordance with (Alhabeb et al., 2017), the most common impurity in $Ti_3AlC_2$ powder is $Ti_2AlC$. The two are distinguishable from each other by their first and their primary peaks which are at around 10° and 45°, respectively. As seen, no $Ti_2AlC$ peaks are observed around 10°, but there is a tangent to the $Ti_3AlC_2$ 45° peak. This means that a single MAX phase with all specific properties relating to it cannot be entirely considered due to a small proportion of impure $Ti_2AlC$, phases. As mentioned in Section 4.1, the attained MAX phases are listed as 98% pure, this agrees with what the XRD results have shown in that there exists a proportion of $Ti_2AlC$ in the sample. Based on the XRD, all three samples have been confirmed to possess the crystalline structure of the desired $Ti_3AlC_2$.

In Figure 5.2, SEM images of the first, second and third MAX phase batches are shown. Images a) and b) represent the first, c) and d), the second, and e) and f), the third. In the figure, the layered structure of the $Ti_3Alc_2$ metal carbide can clearly be seen in all the high magnification SEM images b), d) and f).

For the first batch, while the particle size observed in Figure 5.2 image b) is around 15 µm, the bulk material is shown in a), to have a larger particle size (up to 25 µm). This variation in the lateral particle size distribution (PSD), is expected to influence the etching parameters during MXene synthesis. In accordance with Wei et al. (2021), larger flakes take longer to etch than smaller, or ± 2 µm are expected to take. This was attributed due to the etching kinetics which is a function of aluminium access and by virtue, lateral flake size. Similarly, for batch two, a particle size distribution of between 10 and 25 µm can be seen in c). These two batches based on the discussed crystalline structure as well as morphology and particle size distribution shown in b) and d), are therefore considered similar. This is noteworthy as batch 1 will be consumed using in-situ HF experiments, and batch 2 using HF experiments.

Batch three, or the 400-mesh $Ti_3AlC_2$ MAX phase is also shown in Figure 5.2. As seen in f), an approximate flake size of 10 µm is shown. This is smaller than that observed in the preceding two images and as this sample was sieved through an aperture of half the diameter to the 200-mesh sample, it is expected. While not easily seen in e), the bulk material should consist of smaller laterally sized flakes. This, as per Section 2.3.2 will influence etching time as well as MXene flake size post synthesis. Should the MXene flake size be decreased, the result should correlate to an increase in the specific surface area as measured by the BET analysis.

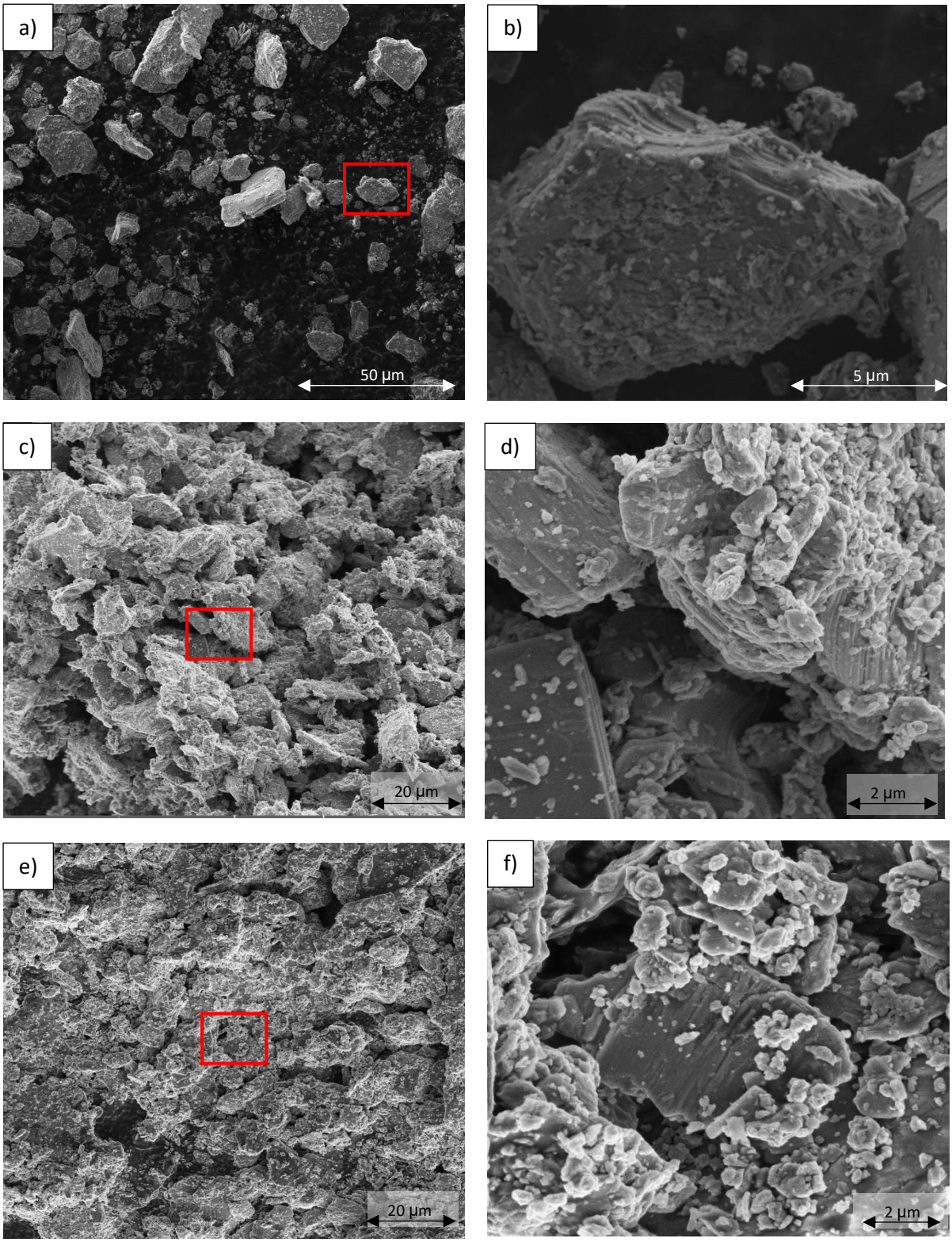


Figure 5.2: SEM images of batch 1 a), b) batch 2 c), d) and batch 3 e), f) of $Ti_3AlC_2$ MAX phases synthesized by hot pressing as sourced from Easchem Co. Images a), b) and c), d) correspond to a 200-mesh particle size and e), f) a 400-mesh particle size. All particles inscribed in red squares are shown at a higher magnification in their adjacent right sided image.

Following the XRD and SEM analysis which confirmed the crystalline structure and morphology to be consistent across batches and with literature, Raman spectroscopy was performed to describe the bonding within the MAX phase's crystal structure. Figure 5.3 shows the Raman spectra for each of the three batches of $Ti_3AlC_2$ procured. As seen, the peaks are in the region between 200 and 700 $cm^{-1}$.

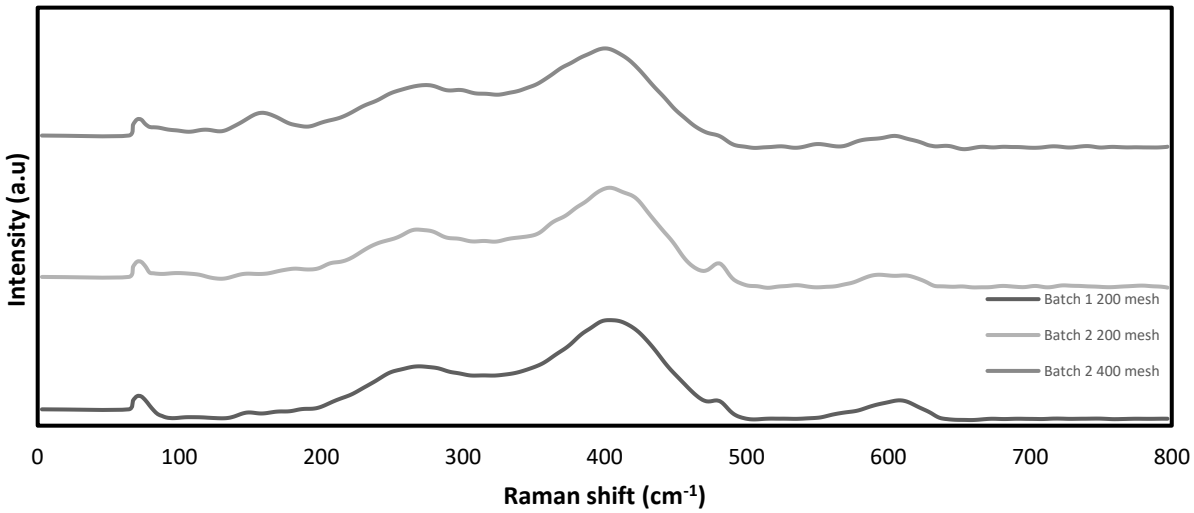


Figure 5.3: $Ti_3AlC_2$ starting material Raman spectrums shown first by batch size and then particle size.

As per Section 2.2.1, for a 312 MAX phase, or $Ti_3AlC_2$, MX layers are reflected about the A-group element located at the centre of a trigonal prism (Eklund, Rosen & Persson, 2017). In accordance with Naguib et al. (2011), the Al-Ti vibrations corrospond to the first three peaks at 70, 250 and 400 $cm^{-1}$. The last two peaks at 490 and 600 $cm^{-1}$, in Figure 5.3 are said to then correspond to Ti-C vibrations. It is therefore expected that after the selective etching of the Al, that the first three peaks will cease to exist. Once more, this selective etching of Al occurs due to its weaker metallic bonding by comparison to the MX layers covalent bonds as discussed in Section 2.2.2. From Figure 5.3, consistency in the bond order and functional groups between samples is confirmed.

A BET analysis confirmed a starting material specific surface area of 2 $m^2\ g^{-1}$ for each of the three batches. While the 400-mesh $Ti_3Al_2$ is supposed to have smaller particles on average and thus a higher specific surface area (SSA), the accuracy at such small values must be considered. After etching, however, the smaller starting particle size is expected to show differences. The attained SSA agrees with literature where previous investigations into $Ti_3AlC_2$ SSA by Tang, Yang & Que (2018), found it to also be 2 $m^2\ g^{-1}$. As mentioned in Section 4.5, the BET analysis was performed after degassing for 3 hours at a temperature of 200 °C. These conditions were replicated from Tang, Yang & Que (2018), on the basis of $Ti_3AlC_2$'s resistance to oxidation below temperatures of 400 °C (Li, Wang, et al., 2015).

## 5.2 $Ti_3C_2T_x$ MXene Synthesis

### 5.2.1 X-ray Diffraction Analysis Considerations

During the experimental characterisation of the as-synthesised MXene's herewith investigated, it was noted that the intensity of the primary MXene characterisation peak (002), at around 8° would decrease in intensity and broaden over time as shown in Figure 5.4.

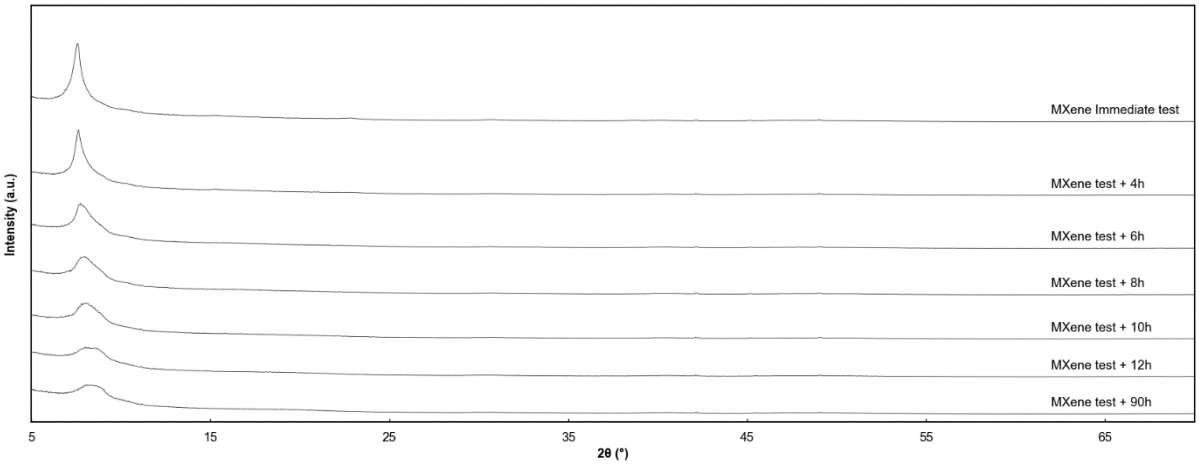


Figure 5.4: XRD evolution from zero to 90 hours showing a decrease in peak intensity of 0.5 g, 200-mesh $Ti_3C_2T_x$ etched in 10 ml of 30 wt % HF at 30 °C after vacuum filtering and oven drying at 60 °C.

Gogotsi & Barsoum (2012), have noted that exfoliation of MAX phases introduces a drastic loss in structural order and by virtue, crystallinity. They note further that cold-pressing of MXene samples forces the delaminated layers to restack in their preferred orientation. Without cold-pressing, however, delaminated MXene (002) peaks shift to lower angles. This in turn relates to higher c parameters which is observed as peak broadening in Figure 5.4.

This analysis was performed by dispersing and vacuum filtering the MXene solution to the desired pH immediately after synthesis. From Figure 5.5 , it is observed that through the vacuum filtering process, no harm is inflicted on the flakes as none of the edges were rounded. Further, the exfoliated sheets remained in the desired accordion like morphology. It was only to the additional risk of having to decant volumes of dilute HF through a vacuum filter, that this processing methodology was not seen as practical for long term use.

Finally, in the XRD diffractograms to follow, it should be noted that due to laboratory equipment sharing, even while measurements were recorded as quickly as equipment became available, it would not always be within the desired first 4 hours after etching and drying where the sharpest peaks are attained.

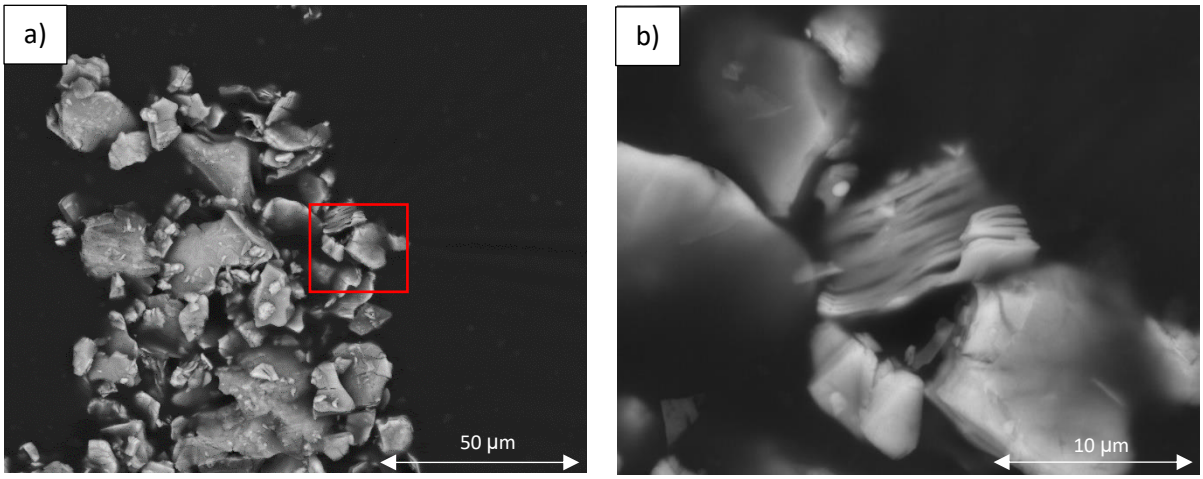


Figure 5.5: SEM images of 0.5 g, 200-mesh $Ti_3C_2T_x$ etched in 10 ml of 30 wt % HF at 30 °C after vacuum filtering and oven drying at 60 °C. The particle inscribed in the red square is shown at a higher magnification the adjacent right sided image.

### 5.2.2 In-situ HF etching

#### 5.2.2.1 Etchant HCl:LiF Molar Ratio Optimization

It was found by Lipatov et al. (2016), that to provide delaminated sheets without sonication, a LiF:HCl ratio of 3:1 should be employed. The bypassing of the sonication process was said to be possible by having excess $Li^+$ ions available for intercalation. This was therefore employed as the first molar ratio considered. All samples in this section were etched for 24 hours and at 35 °C as per Lipatov et al's. (2016), outlined synthesis conditions. In Figure 5.6, for the 3:1 HCl:LiF molar ratio a new peak at 8° becomes visible. The primary MAX phase peaks at 11.04°, 45.61°, and 48.94° are, however, also still visible.

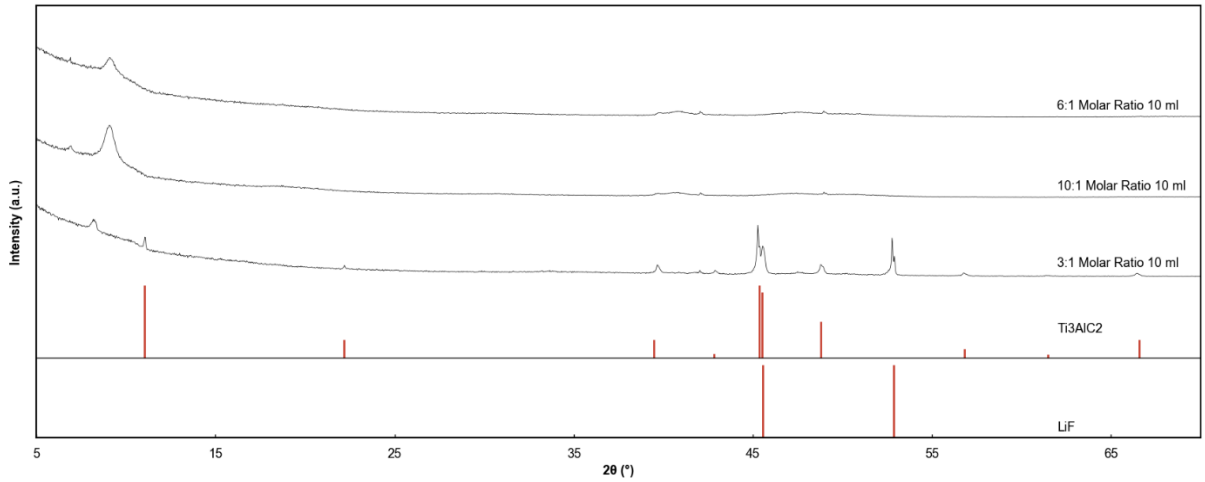


Figure 5.6: XRD diffractogram of 0.5 g, 200-mesh $Ti_3AlC_2$ etched in 10 ml in-situ HF at different molar ratios of LiF:HCl, for 24 hours at 35 °C against reference patterns of $Ti_3AlC_2$ and LiF.

The XRD spectrum shown in Figure 5.6 indicates that there are both MAX phases and MXene's present in the sample. As mentioned earlier in Section 5.1, this is a consequence of the particle size distribution with smaller flakes etching quicker than larger ones. Additionally, a set of new peaks at 45.5 ° and 53.3 ° are formed. This indicates that there remains residual LiF not washed away in the washing process. This phenomena was also experienced by Alhabeb et al. (2017), who mention copious amounts of washing may be required to remove residual LiF and or LiCl salts.

Shown in Figure 5.7 images a) and b), are the SEM images for the 3:1 HCl:LiF molar ratio etched sample. While it can be seen in b), that not all sheets are etched and delaminated, in a), several delaminated sheets are seen scattered throughout the sample. It is also evident from a), that many of the delaminated sheet's agglomerate. This, as previously referenced Section 5.2.1, is the physical manifestation of the loss in structural order and by virtue, crystallinity.

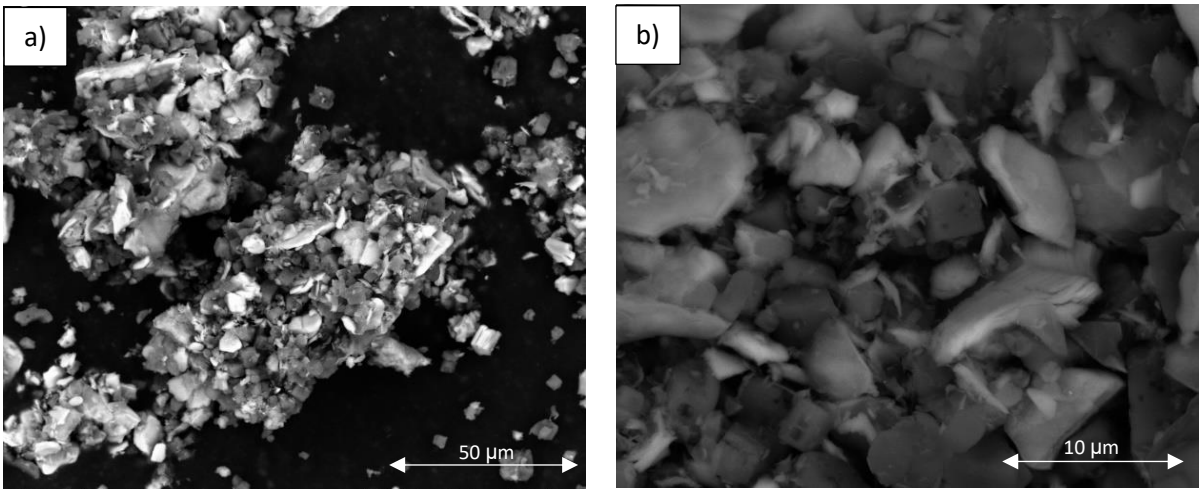


Figure 5.7: 0.5 g, 200-mesh $Ti_3AlC_2$ etched in 10 ml in-situ HF using a 3:1 HCl:LiF molar ratio for 24 hours at 35 °C shown at different magnifications in a) and b).

From the EDS analysis performed and as shown in Figure 5.8, nearly all the aluminium is seen to have been removed with traces remaining on the surface of some sheets as shown in Figure 5.8, Spectrum 1. It is also seen that residual $Cl^+$ ions are still present albeit in small quantities and have not been washed away in this same location. This went undetected by XRD measurements due to the small quantity of only up to 1.2 atomic wt %. The location of LiF, is predominantly in spectrums three and four in Figure 5.8 which is between sheet layers where etching has occurred. This is aligned with literature which suggest rigorous washing may be required to remove the LiF after it reaction with the aluminium where it is in excess against HCl (Alhabeb et al., 2017).

While the presence of oxygen from the EDS analysis was originally unexpected, without any new peaks forming in the XRD in Figure 5.6, oxidation of the MXene and the subsequent formation of Rutile or Anatase titanium dioxide ($TiO_2$), was ruled out. This was further supported by work from Li, Wang, et al. (2015), who noted that $Ti_3C_2T_x$ oxidation does not occur even in an oxygen environment below temperatures of 200 °C. The oxygen is therefore presumed to be no more than a few nanometres thick layer of alumina present due impurities or exposed aluminium not bound between Ti-C layers.

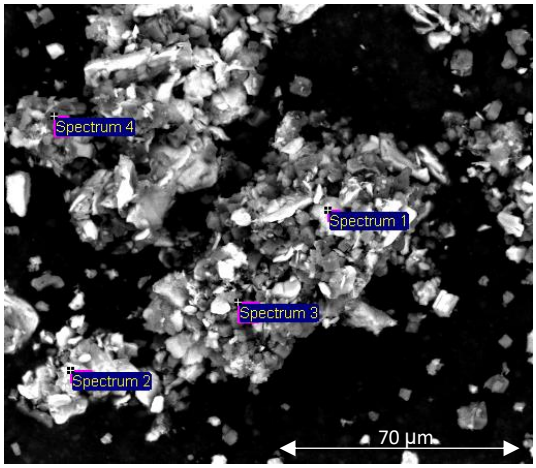


| | EDS analysis in atomic weight % | | | | | |
|---|---|---|---|---|---|---|
| | C | O | F | Al | Cl | Ti |
| Spectrum 1 | 16.7 | 9.6 | 35.3 | 1.8 | 1.2 | 35.4 |
| Spectrum 2 | 38.0 | 22.9 | 23.7 | 0.3 | 0.6 | 14.5 |
| Spectrum 3 | 6.3 | 4.0 | 84.4 | 0.1 | 0.2 | 5.0 |
| Spectrum 4 | 32.2 | 9.6 | 50.7 | 0.1 | 0.4 | 7.0 |

Figure 5.8: EDS spectrum sources and elements shown in atomic weight % of 0.5 g, 200-mesh $Ti_3C_2T_x$ etched in 10 ml 3:1 HCl:LiF for 24 hours at 35 °C.

Finally, the expected termination groups of -OH and -F are also seen to be present in Figure 5.8 as per Naguib et al's. (2011), findings. Rabis, Rodriguez & Schmidt (2012), recommended for an alternative support material for the ORR, a BET surface area of 50 $m^2\ g^{-1}$ must be attained. For this sample, however, the BET surface area measurement was limited to only 5 $m^2\ g^{-1}$. While exfoliated and delaminated sheets are seen in both a) and b) of Figure 5.7, on closer inspection in image b), some of the layers have not been completely etched. This relates to only a moderate extent of exfoliation and agrees with the results as seen from the XRD diffractogram. It also motivates that etching and delamination parameters may need refinement. In the process of trying to increase the specific surface area, alleviate the residual impurities and etch and delaminate a larger portion of the sample, different HCl:LiF ratios were investigated.

To remove the residual traces of LiF salt after etching, different molar ratios were investigated. LiF was set as the limiting reagent when reacted with the in situ-HF. As the limiting reagent, LiCl formation is kept to a minimum. This is important as it requires generous amounts of water to be washed away (Alhabeb et al., 2017).

To enact the above, the exact same protocols as per the previous sample were used, only the HCl diluted to only 10 M with 0.25 g of LiF added into solution. This provided a 10:1 HCl:LiF ratio. From the diffractogram in Figure 5.6, it was clear that the MAX phase powder had been transformed to a MXene. This was confirmed by the presence of the $Ti_3C_2T_x$ primary peak at around 8° which is observed along with the complete disappearance of the original MAX phase's primary peaks at 11.04°, 22.33° and 45.61°. Lastly, the LiF peaks signifying the presence of these impurities have been removed.

While the XRD indicates a successful etching process, the SEM in Figure 5.9 images a) and b), indicate that the desired accordion like morphology has not been attained. Therefore, by the correlation between morphology and SSA, little change in the BET results is expected from the original MAX phase. The *in-situ* HF reaction uses solvated $Li^+$ ions as an intercalant and while the molar ratio maintains LiF as the limiting reagent versus HCl, the ratio utilized was out of standard practice parameters. Due to the shortage of $Li^+$ ions to act as an intercalant, little to no change in morphology has occurred.

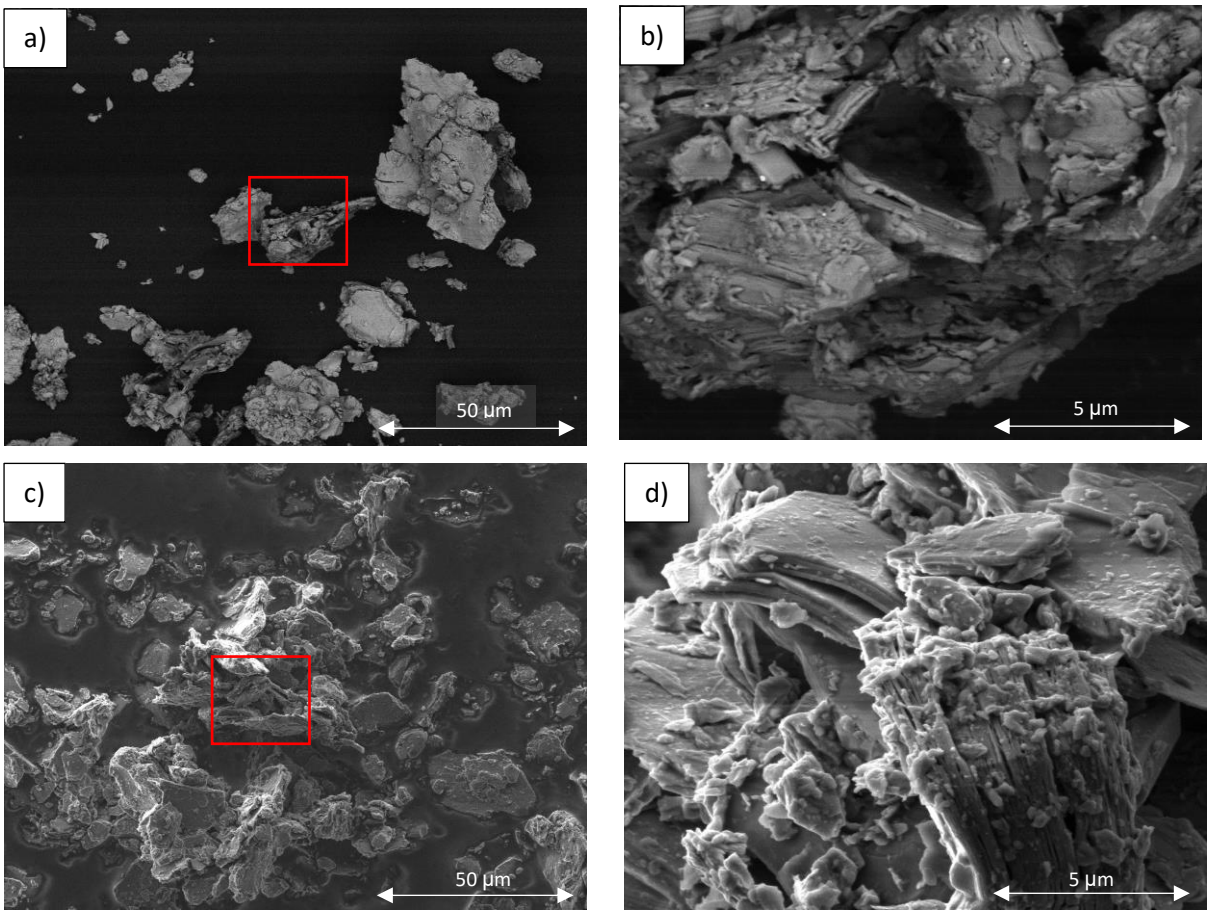


Figure 5.9: SEM images of 0.5 g, 200-mesh $Ti_3C_2T_x$ etched at different HCl:LiF molar ratios in 10 ml in situ-HF for 24 hours at 30 °C. Images a) and b) 10:1 HCl:LiF at different magnifications & images c) and d) 6:1 HCl:LiF at different magnifications. The particle inscribed in the red square is shown at a higher magnification in the adjacent right sided image.

Due to the lack of delamination of flakes or any change in physical characteristics, no BET measurements were taken for this sample. It is evident however, that some midpoint should exist between decreasing residual traces of LiCl and attaining delaminated flakes. For this, a third etching ratio was investigated which lay between the two already considered.

The final molar ratio investigated was an HCl:LiF ratio of 6:1. As previously mentioned, this was selected as a midpoint such that delaminated $Ti_3C_2$ flakes without any residual LiF or LiCl which requires generous washing, could be synthesized. Much like with the previous sample investigated, the XRD in Figure 5.6 indicates a successful etching process with no residual LiF in the sample. The SEM images in both c) and d) of Figure 5.9, however, once more indicate that the desired accordion like morphology has not been attained. By virtue, little change in specific surface area is again expected. The degree of etching and delamination shown in Figure 5.9 is superior to that from the previous 10:1 ratio but falls significantly short of the 3:1 HCl:LiF ratio as shown in Figure 5.7. This was due to a shortage of intercalant material in the form of $Li^+$ ions. This means that while the sample is free of impurities due to a smaller portion of solvated $Li^+$ ions in solution, intercalation and by virtue etching and further, delamination, is near impossible.

As expected, an approach to the desired BET SSA for this sample was not observed. The SSA was measured at 4 $m^2 g^{-1}$, which although it is an improvement from the original 2 $m^2 g^{-1}$, it does not satisfy the catalyst support requirements (>50 $m^2 g^{-1}$). Having recognised the source of the impurity, an approach to make corrections to the experimental parameters and have these impurities removed was undertaken. Based on the degree of delamination and the corresponding change to the specific surface area, an investigation into modification of parameters using the 3:1 HCl:LiF molar ratio ensued.

#### 5.2.2.2 Temperature and Molar Ratio Optimization

In accordance with Alhabeb et al. (2017), a molar ratio of greater than 7.5, corresponding to a mass ratio of one, is a minimum parameter between LiF and $Ti_3AlC_2$ MAX phase powders. This is to facilitate the desired etching role of the $Li^+$ ions present in solution. As a result, 20 ml of etchant with 0.52 g of LiF will now be used along with the 0.5 g of $Ti_3AlC_2$ powder. This will satisfy both the requirements from Lipatov et al. (2016) and Alhabeb et al. (2017). The final modification to the experimental system was to cover the etching solution. This was implemented to reduce etchant loss due to evaporation. Further, it was found by Liu et al. (2017) after performing $Ti_3AlC_2$ in-situ HF etching over a temperature range from 30 °C to 60 °C, that temperature plays a significant role in MXene synthesis.

With an increase in temperature, Liu et al. (2017) found a larger proportion of the sample to transform from a MAX phase to a MXene in the same amount of time. This was the result of increased atomic collisions which increases the rate of reaction. This means more Al atoms are being reacted with the in-situ HF and by virtue, more hydrogen being formed. The rate of hydrogen gas formation is directly responsible for the desired accordion like structure synonymous with successful etching (Alhabeb et al., 2017). Following the above, a 3:1 HCl:LiF ratio was used, with modifications to the etchant volume and LiF salt mass to align with optimised literature conditions mentioned above. Etching was now also set at 60 °C as opposed to 45 °C. The diffractogram comparing the results between the original and optimized conditions is shown in Figure 5.10.

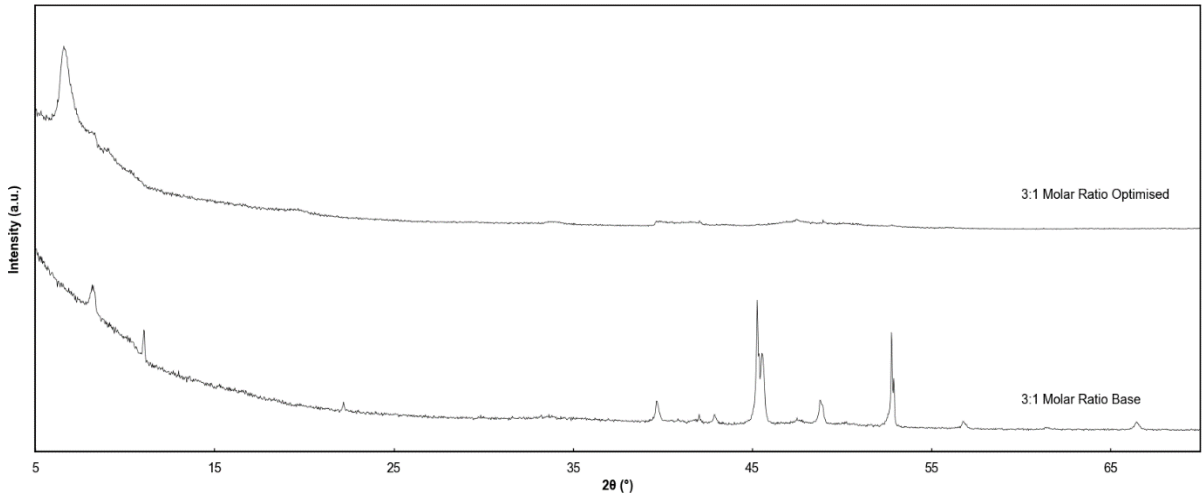


Figure 5.10: XRD diffractogram of 0.5 g, 200-mesh $Ti_3C_2T_x$ etched in 20 ml 3:1 HCl:LiF for 24 hours at 60 °C (covered) contrast to 0.5 g $Ti_3AlC_2$ etched in 10 ml 3:1 HCl:LiF for 24 hours at 60 °C (uncovered).

From Figure 5.10, it is seen that the aluminium has been successfully etched from the MAX phase. This is confirmed by the disappearance of the primary MAX phase peaks at 11.04°, 22.33° and 45.61° along with the presence of the MXene 8° peak. With the modified experimental conditions, it was also possible to eliminate the presence of impurities. Figure 5.11 shows the SEM results. From the SEM images a) and b) shown in Figure 5.11, a significant improvement to the degree of etching and delamination when compared to the unoptimized conditions shown in Figure 5.7 is observed. By comparison, a larger portion of the bulk $Ti_3AlC_2$ powder has been transformed to $Ti_3C_2T_x$. From image b) it is further confirmed that the Ti-C layers have been split apart and the accordion like morphology attained. After etching and delaminating, this sample had a specific surface area of 14 $m^2\ g^{-1}$. While considerably larger than the starting material (2 $m^2\ g^{-1}$), it still falls significantly short of the 50 $m^2\ g^{-1}$ target (Rabis, Rodriguez & Schmidt, 2012). The attained specific surface area, does however, agree with literature from a study performed by Kumar et al. (2020), where a value of 11 $m^2\ g^{-1}$ was attained.

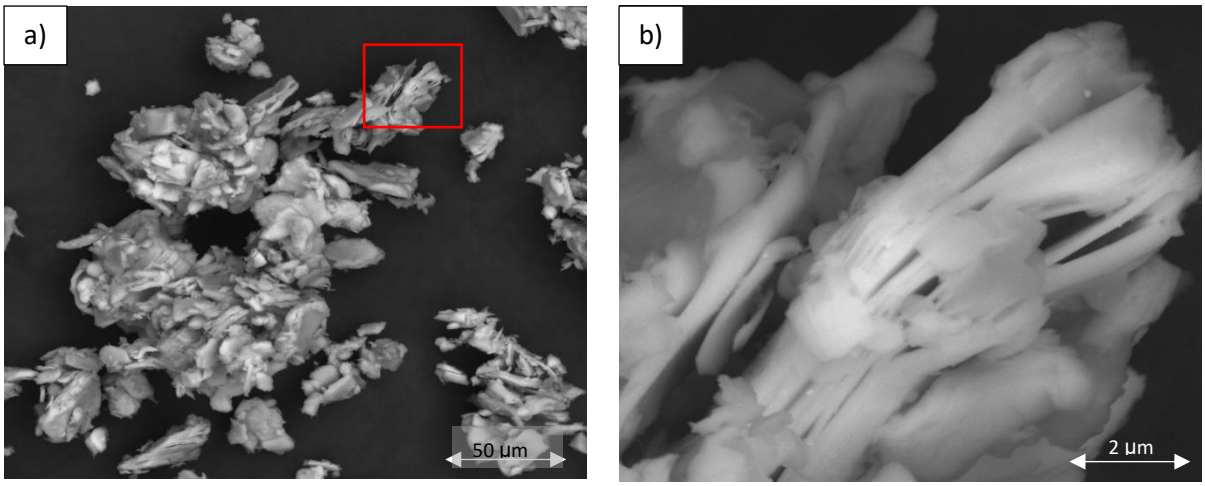


Figure 5.11: SEM images of 0.5 g, 200-mesh $Ti_3C_2T_x$ etched in 20 ml 3:1 HCl:LiF for 24 hours at 60 °C (covered). The particle inscribed in the red square is shown at a higher magnification in the adjacent right sided image.

#### 5.2.2.3 Etching Time Optimization

When similar experimental conditions as shown in Section 5.2.2.2 were repeated, only this time for 48 instead of 24 hours, the diffractogram in Figure 5.12 was attained.

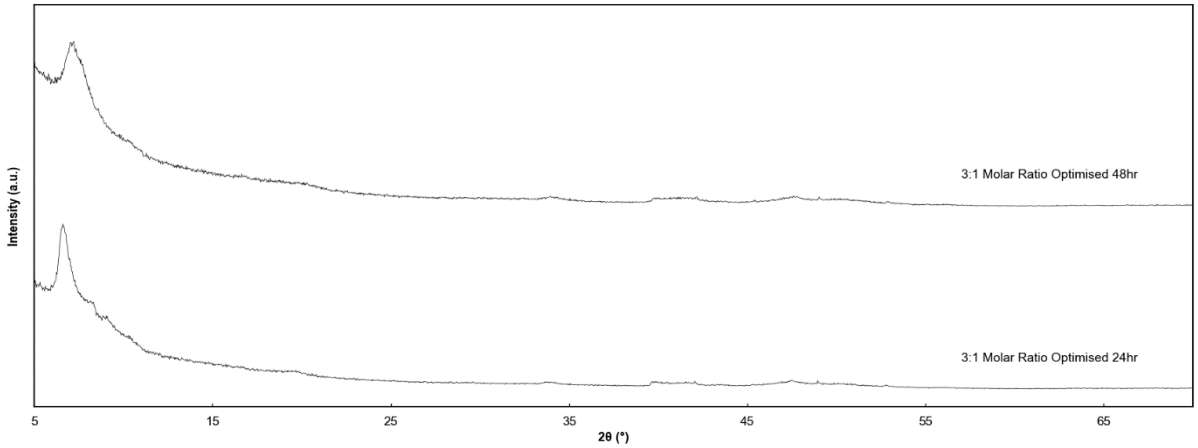


Figure 5.12: XRD diffractogram of 0.5 g, 200-mesh $Ti_3C_2T_x$ etched in 20 ml 3:1 HCl:LiF for 24 hours at 60 °C (covered) comparison to 0.5 g $Ti_3AlC_2$ etched in 20 ml 3:1 HCl:LiF for 48 hours at 60 °C (covered).

From the XRD, the presence of the $Ti_3C_2T_x$ MXene is again confirmed for the sample etched for 48 hours. In general, an increase in time allows a greater opportunity for a solution or etchant to act on a substrate. However, if the reaction was already completed within the shorter period, extending it would offer no value. Without any changes in the XRD or SEM images shown in Figure 5.14, the 24-hour etched sample was therefore deemed ideal. This agrees with literature which suggests for $Ti_3AlC_2$ etched in a 3:1 HCl:LiF ratio, at a temperature of 50 °C, only 24 hours is required (Liu et al., 2017). No BET measurements were taken for this sample as no changes were observed.

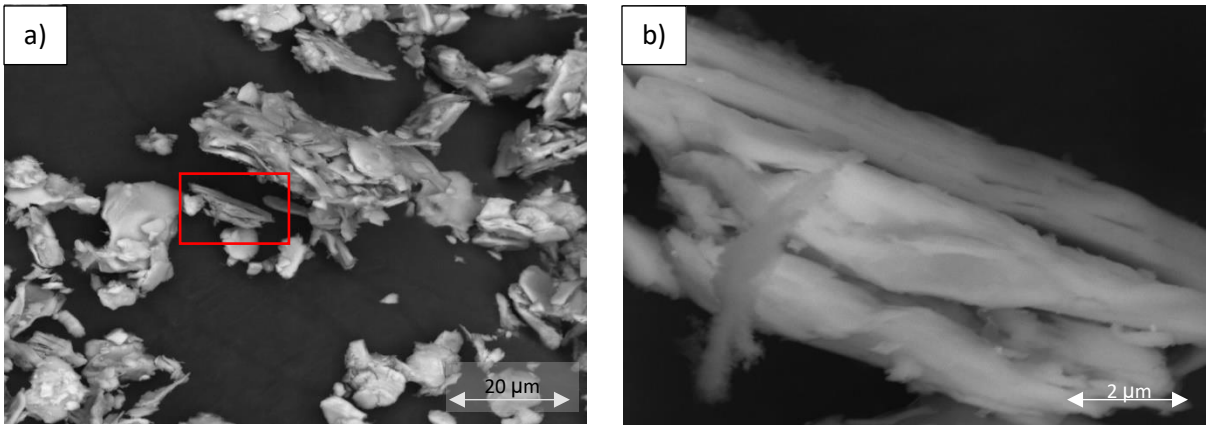


Figure 5.13: SEM images of 0.5 g, 200-mesh $Ti_3C_2T_x$ etched in 20 ml 3:1 HCl:LiF for 48 hours at 60 °C (covered). The particle inscribed in the red square is shown at a higher magnification the adjacent right sided image.

### 5.2.3 HF Etching

#### 5.2.3.1 $Ti_3AlC_2$ Etching in 30 wt % HF for Different Times

Without having attained the desired specific surface area with in-situ methods, HF etching was introduced. For all HF experiments, 10 ml of etchant was used with 0.5 g of $Ti_3AlC_2$ powder. These conditions were replicated from Alhabeb et al. (2017), who showed them to be suitable. Alhabeb et al. (2017), also showed that 30 wt % HF is the minimum concentration required to provide the desired accordion like morphology. As such, this concentration served as the starting point for this analysis. For the etching temperature, the minimum heater plate setting of 30 °C was used in all HF experiments. This was to maintain the mildest possible conditions as outlined in Chapter One.

Shown in Figure 5.14, are the XRD spectrums attained after the processing of $Ti_3AlC_2$ etched in 30 wt % HF from 1.5 to 24 hours. From 1.5 hours the $Ti_3AlC_2$ MAX phase is transformed to $Ti_3C_2T_x$ with the aluminium completely etched out. The morphological changes are also seen to take effect from 1.5 hours as shown in Figure 5.15.

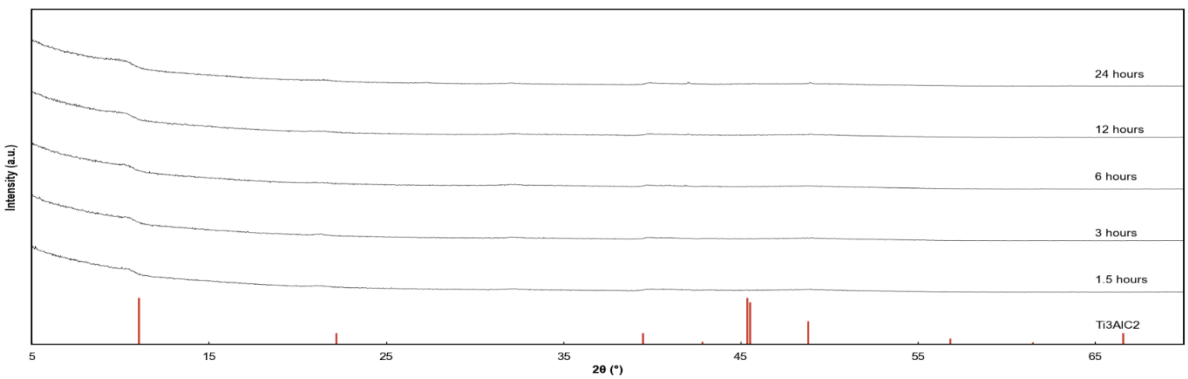


Figure 5.14: XRD diffractogram of 0.5 g, 200-mesh $Ti_3AlC_2$ etched at 30 °C in 10 ml 30 wt % HF at various time intervals from 1.5 to 24 hours against the reference pattern of $Ti_3AlC_2$.

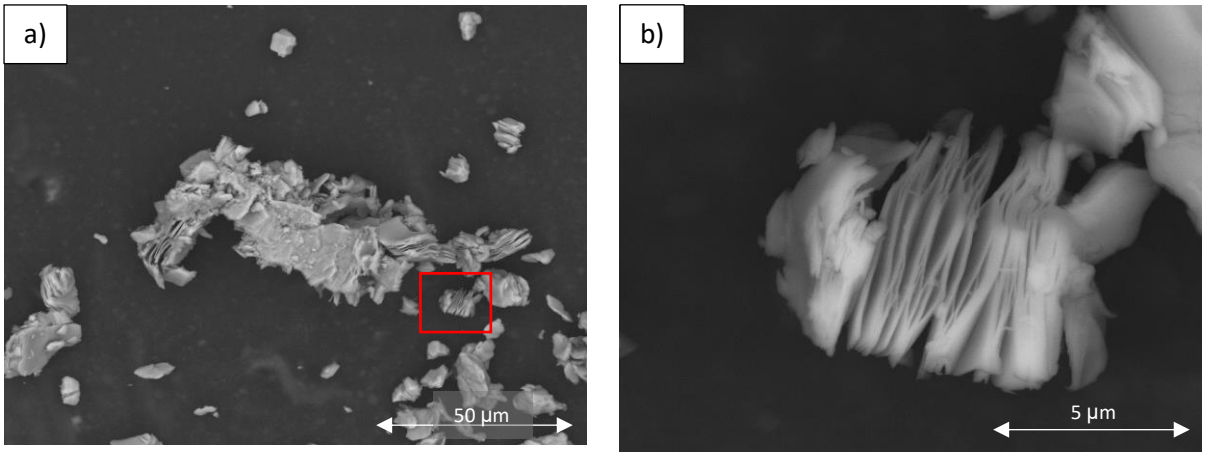

Figure 5.15: SEM images of 0.5 g, 200-mesh $Ti_3C_2T_x$ after etching in 10 ml in 30 wt % HF at 30 °C for 1.5 hours. The particle inscribed in the red square is shown at a higher magnification the adjacent right sided image.

It is immediately evident from Figure 5.15 b), that a higher degree of exfoliation was achieved when compared to in-situ HF application. As seen in Figure 5.15 a) the exfoliation, however, does not extend to delamination. The increased degree of exfoliation is the result of a higher molar concentration of HF acting on the MAX phase substrate. While etching is observed clearly in b), the bulk sample a) can be seen to warrant a higher degree of etching from a longer time exposure to the etchant. This again relates to the particle size distribution of the MAX phase with some larger particles seen to be unetched. As seen in Figure 5.15, it is predominantly the smaller flakes which have been exfoliated.

At double the etching time of the 1.5 hour experiment shown in Figure 5.15, a similar degree of exfoliation is observed in Figure 5.16 b). It is, however, observed to a larger portion of MAX phases as seen in a). The exact same testament is observed for the 6-hour etched MXene c) and d). The only variance being small, delaminated flakes are also observed in d) across the etched layers. From the XRD diffractograms shown in Figure 5.14, all samples shown in Figure 5.16 are confirmed as MXene's. By extending the etching time to 12 and 24 hours in e), f) and g), h), respectively, a continuous increase in the degree of exfoliation to the bulk sample was observed up until the 24 hour etched sample was approached. The specific degree of exfoliation to any single flake, however, remained relatively constant as can be seen in f) and h). While the results show success in attaining the desired morphology, the BET measurements reveal that the SSA is only increased to 7 and 6 $m^2 g^{-1}$ for the 12 and 24 hour exfoliated samples, respectively. The decrease between the 12 and 24 hour SSA may be attributed to the accuracy of BET measurements which serves primarily as an indication as opposed to an absolute figure. Kumar et al. (2020), have, however, also suggested that this decrease may also be the result of adhesion between oxidized MXene layers. On the basis of a larger proportion of the MXene's being etched in the 24 hour sample, these samples are taken for further processing.

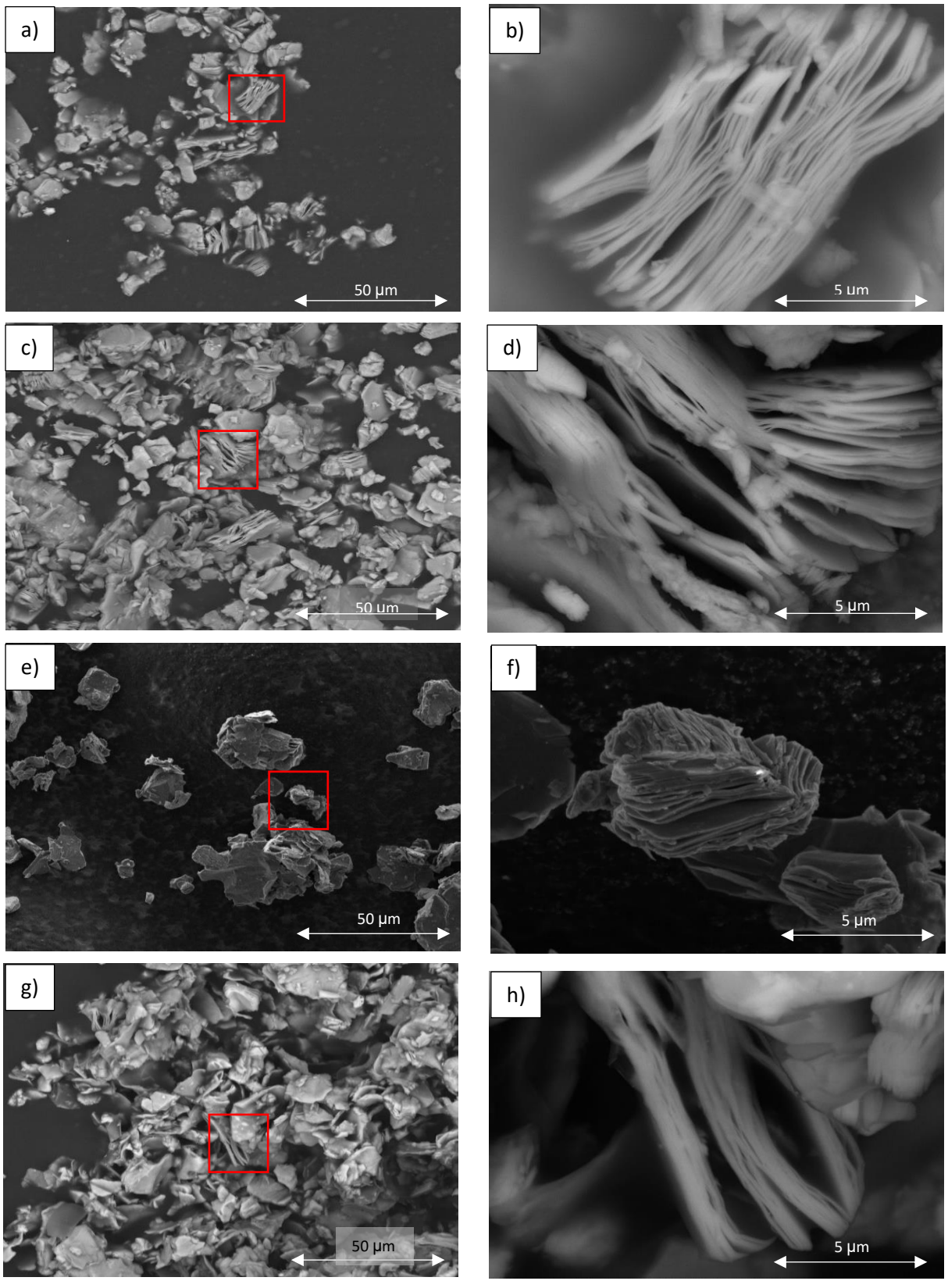


Figure 5.16: SEM images of 0.5 g, 200-mesh $Ti_3C_2T_x$ etched in 10 ml, 30 wt % HF at 30 °C for a), b) 3 hours, c), d) 6 hours, e), f) 12 hours and g), h) 24 hours. The particle inscribed in the red square is shown at a higher magnification in the adjacent right sided image.

#### 5.2.3.2 Concentration Changes

Due to the 30 wt % HF etching not providing the desired SSA, the etchant concentration was increased to 48 wt % HF. After 24 hours of etching at this HF concentration, it was expected that the XRD diffractogram would remain unchanged as the reaction was already complete with all the aluminium reacted at the milder (30 wt % HF) set of conditions. From Figure 5.17, this expectation was confirmed.

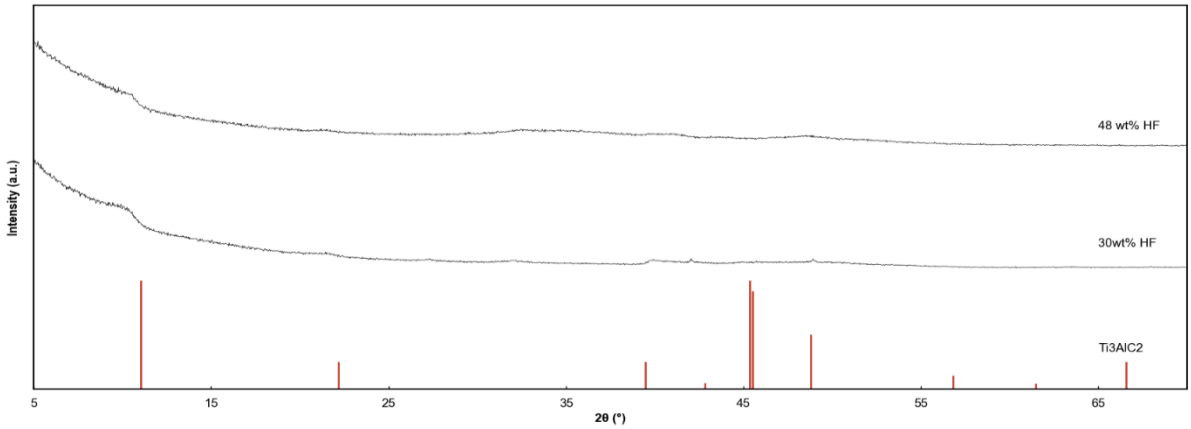


Figure 5.17: XRD diffractogram of 0.5 g, 200-mesh $Ti_3AlC_2$ etched in 10 ml 48 wt % HF at 30 °C for 24 hour comparison to 30 wt % HF at 30 °C for 24 hours against the reference pattern of $Ti_3AlC_2$.

From the SEM images shown in Figure 5.18, a minor degree of delamination can be seen throughout the bulk sample in a). Further, all layers are seen to possess the desired accordion like morphology as shown in b). Figure 5.18 therefore also indicates that after etching at these conditions, the constraint of etching $Ti_3AlC_2$ particles with a sizable particle size distribution have been overcome.

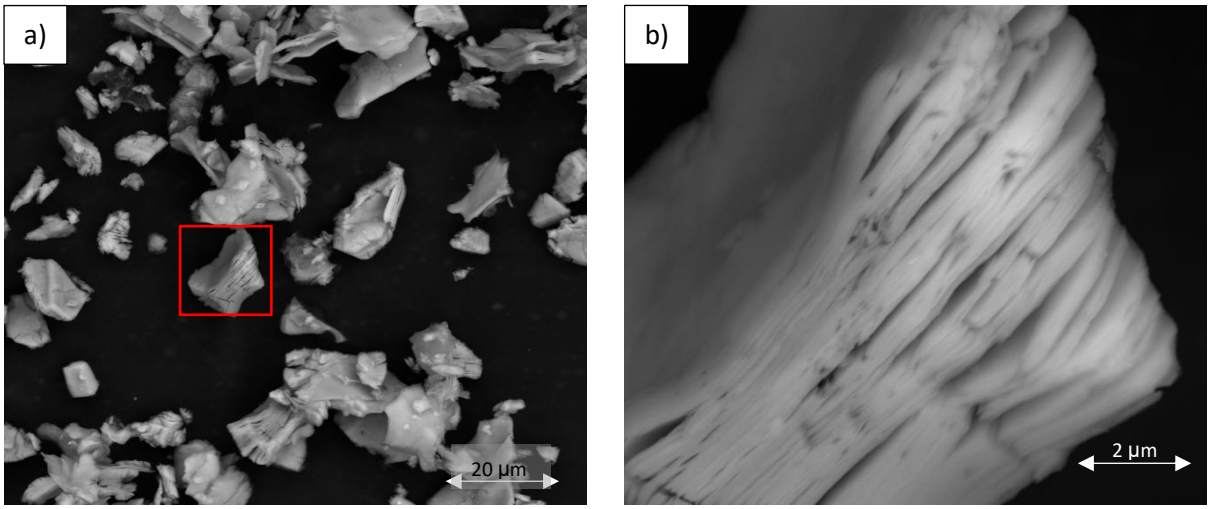


Figure 5.18: SEM images of 0.5 g, 200-mesh $Ti_3C_2T_x$ after etching in 10 ml of 48 wt % HF at 30 °C for 24 hours. The particle inscribed in the red square is shown at a higher magnification the adjacent right sided image.

The specific surface area was measured for the sample etched for 24 hours in 48 wt % HF, and the results only marginally increased to 6 $m^2$ $g^{-1}$. A means of delaminating the etched sample was therefore to be determined. To this end, sonication was introduced to the sample etched in 48 wt % HF at 30 °C for 24 hours. Intercalation was not utilized in this work.

#### 5.2.3.3 Sonication of HF Etched MXene's

The conditions selected for further modification on the basis of literature where it is suggested that for favourable MXene synthesis, high temperature, and HF concentration are both desired along with longer times, were therefore selected as 48 wt % HF for 24 hours at 30 °C (Li, Wang, et al., 2015). The hot plate temperature of 30 °C was maintained on account of using the mildest possible conditions.

Unlike certain in-situ HF etching conditions which do not require sonication to initialise flake delamination, for the breaking of hydrogen bonds post HF etching, sonication is required (Naguib et al., 2011). Maleski et al. (2018), have indicated that the power applied from a probe sonicator and the duration over which it is applied directly affects the lateral size of the flakes. To investigate the effects of sonication time, flakes were sonicated from 5 to 40 minutes. Power was always kept at a constant 100 % and while Maleski et al. (2018), used a pulse setting of 8 s on 2 s off, due to the equipment available, 1 second on and 1 second off was used in this project. The same flake dispersion as Maleski et al. (2018) of 200 mg in 50 ml of deionized water was employed. From the XRD results post sonication processing displayed in Figure 5.19, no changes are observed from Figure 5.17 through the sonicating process to the $Ti_3C_2T_x$ MXene's. This was expected as no changes to the crystalline phases or chemical composition were made.

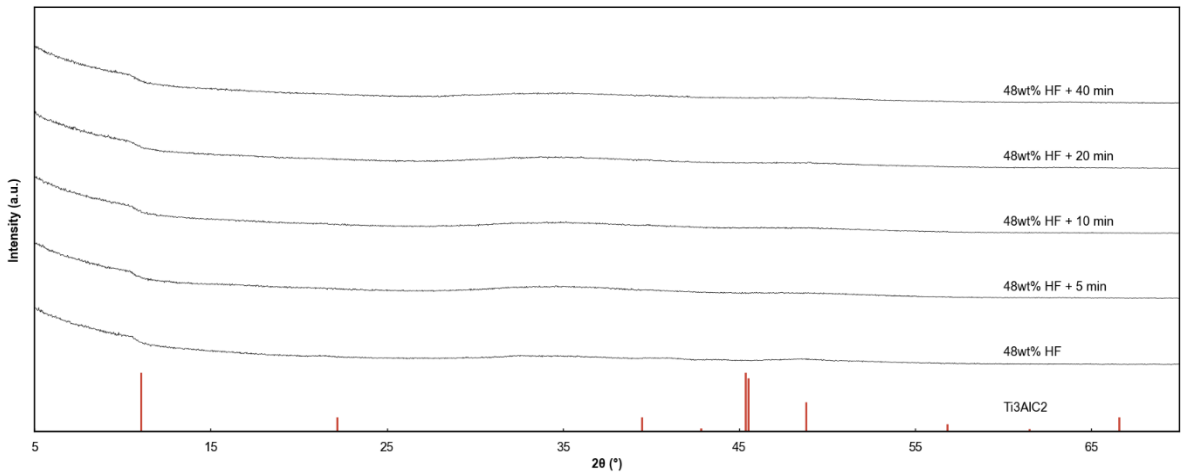


Figure 5.19: XRD diffractogram of 0.5 g, 200-mesh $Ti_3AlC_2$ etched in 10 ml 48 wt % HF at 30 °C for 24-hours and probe sonicated for various times from 5 to 40 minutes against the reference pattern of $Ti_3AlC_2$.

From the SEM results in Figure 5.20 b), even with only 5 minutes of sonicating, changes can be seen to have taken effect to the sample. In this image, subtle changes to flake ends by comparison to Figure 5.18 are observed. These changes were recognised as the onset of delamination. In image a), however, little change to the bulk sample is observed suggesting an increase of sonication time is required for bulk flake delamination. In image d), as expected, after 5 more minutes of sonicating, more flake end rounding is seen than that in the sample sonicated for only 5 minutes. Still, however, little changes to the bulk c) are observed. The same observation was made with progressively increasing flake delamination for the sample sonicated for 20 minutes, images e) and f). The trend outlined above continued through to the sample sonicated for 40 minutes, shown in g) and h). After 40 minutes, however, unlike with previous periods, a large portion of the bulk was seen to be delaminated in g).

Based on the bulk material in Figure 5.20 g), 40 minutes of sonication was considered ideal. Further, from g), clusters of delaminated flakes are seen to agglomerate and form larger groupings of support material. This means the support material will have porous regions where catalyst particle deposition can occur. The agglomerated groupings, in accordance with Hazirah & Junaidi (2021), is the result of strong van der Waals forces between delaminated $Ti_3C_2T_x$ flakes.

From the results, it was determined that a longer sonication time with the same power leads to more exfoliated MXene's delaminating in the bulk. This agrees with literature where (Maleski et al. (2018), found that by varying the mechanical energy input, the lateral size of MXene flakes can be controlled.

For the most delaminated sample sonicated for 40 minutes, the specific surface area was measured as 18 $m^2 g^{-1}$. Once more, this is inadequate based on the requirements outlined by Rabis, Rodriguez & Schmidt (2012), suggesting again that experimental modification is required. The following section looks to advance and on the sonicated flakes and develop a methodology to attain high specific surface area MXene's.

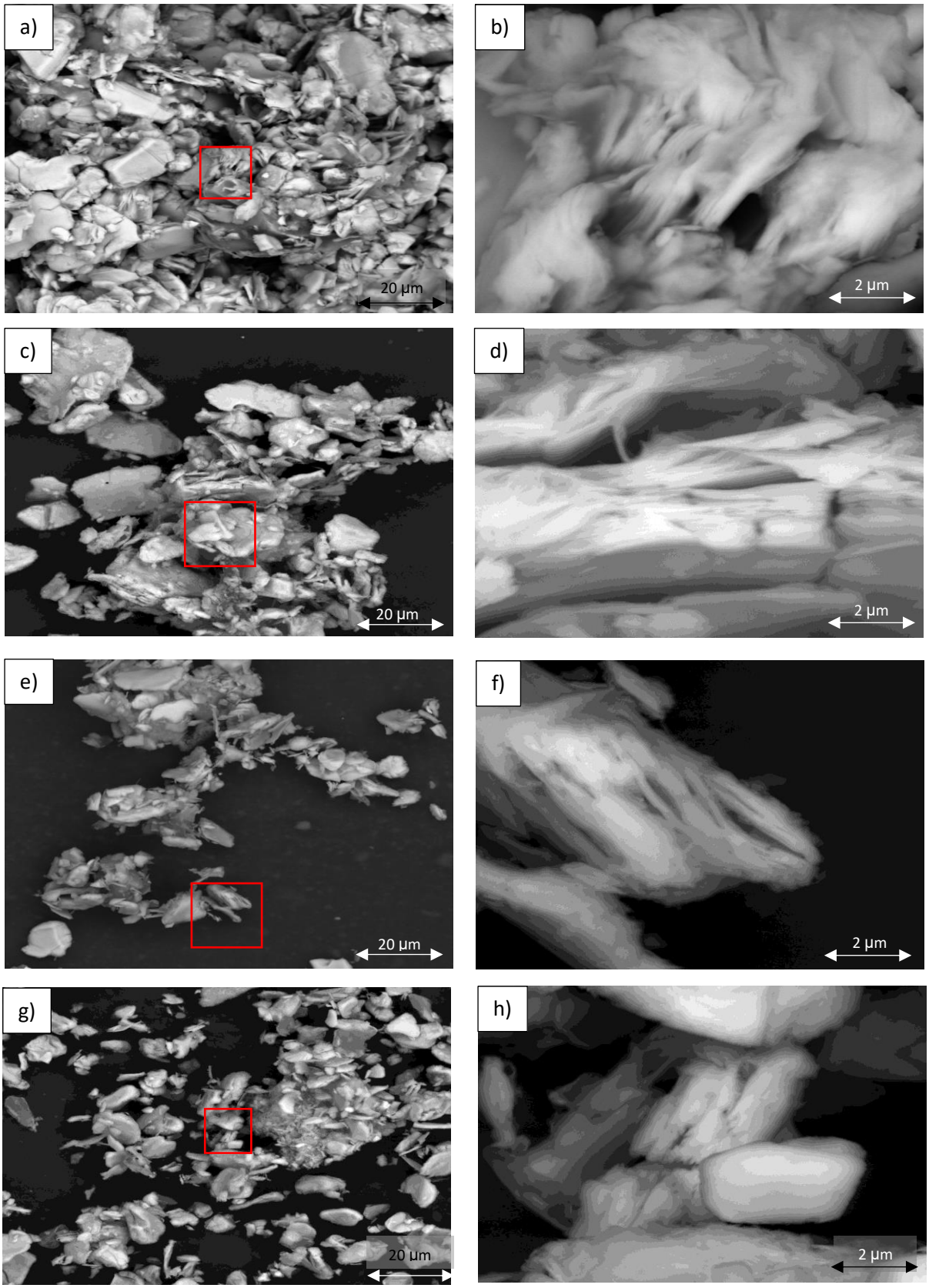


Figure 5.20: SEM images of 0.5 g, 200-mesh $Ti_3C_2T_x$ etched in 10 ml of 48 wt % HF at 30 °C for 24 hours and probe sonicated for 5 minutes a), b) 10 minutes c), d), 20 minutes e), f) and 40 minutes g), h). The particle inscribed in the red square is shown at a higher magnification the adjacent right sided image.

#### 5.2.3.4 Size Reduction by Mechanical Grinding

As mentioned in Section 5.2.3.3, the desired specific surface area could not be attained by sonication only. It was therefore required that further experimental modification be undertaken. From literature, Shahzad et al. (2017), attained a BET SSA of 68 $m^2 g^{-1}$ for delaminated $Ti_3C_2T_x$ flakes. By comparison between their synthesis methods to those performed, it was noted that they had ground their powders prior to sonicating. As the grinding method was not disclosed, two methods were employed in this project to increase the specific surface area of the delaminated flakes. The grinding methods selected were based on available laboratory equipment and comprised of grinding by mortar and pestle as well as micronizing in a lab scale mill. The XRD diffractograms for the MXene samples post grinding and sonicating is shown in Figure 5.21. Once more, both samples are confirmed to have been transformed to MXene's by the complete disappearance of the original MAX phase's primary peaks at 11.04°, 22.33° and 45.61°.

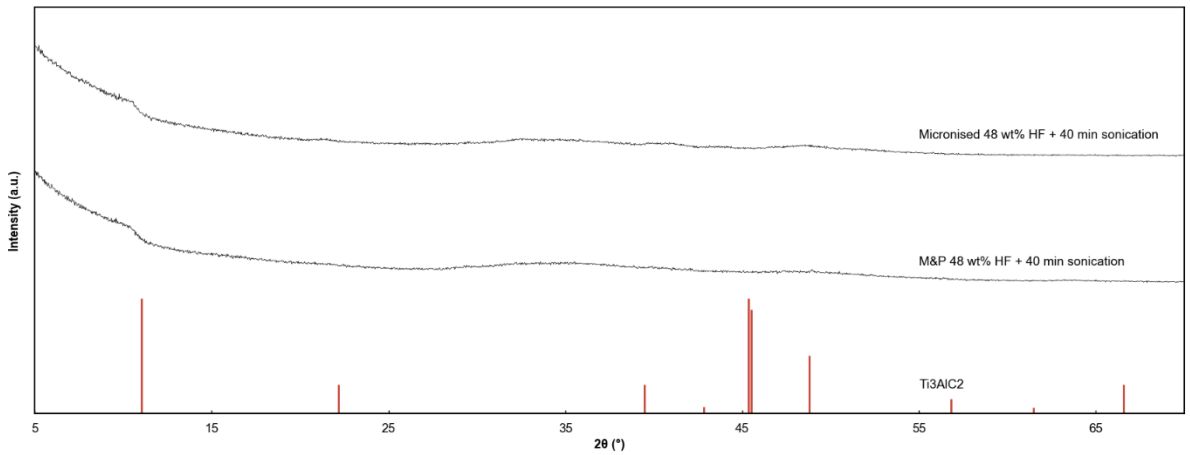


Figure 5.21: XRD diffractogram of 0.5 g, 200-mesh $Ti_3AlC_2$ etched in 10 ml 48 wt % HF at 30 °C for 24-hours and ground by mortar and pestle and a micronizor before being probe sonicated for 40 minutes against the reference pattern of $Ti_3AlC_2$.

The SEM images a) and b), shown in Figure 5.22 are those after grinding by mortar and pestle, but before sonication. As seen, agglomerates are formed in a) which are due to more delaminated flakes flocking together because of the van der Waals forces between them. In b), etched flakes can be seen to have suffered no structural damage by the grinding process. As the flakes were already etched and their sides exposed, little change to the SSA was expected and was also confirmed with a measured specific surface area of 6 $m^2 g^{-1}$.

The second method of grinding was performed by micronizing c) and d). Here, ceramic media was placed along with the sample into a holder. Autogenous grinding then ensued for a period of 10 minutes. Unlike with the mortar and pestle, significant morphological changes occurred after grinding.

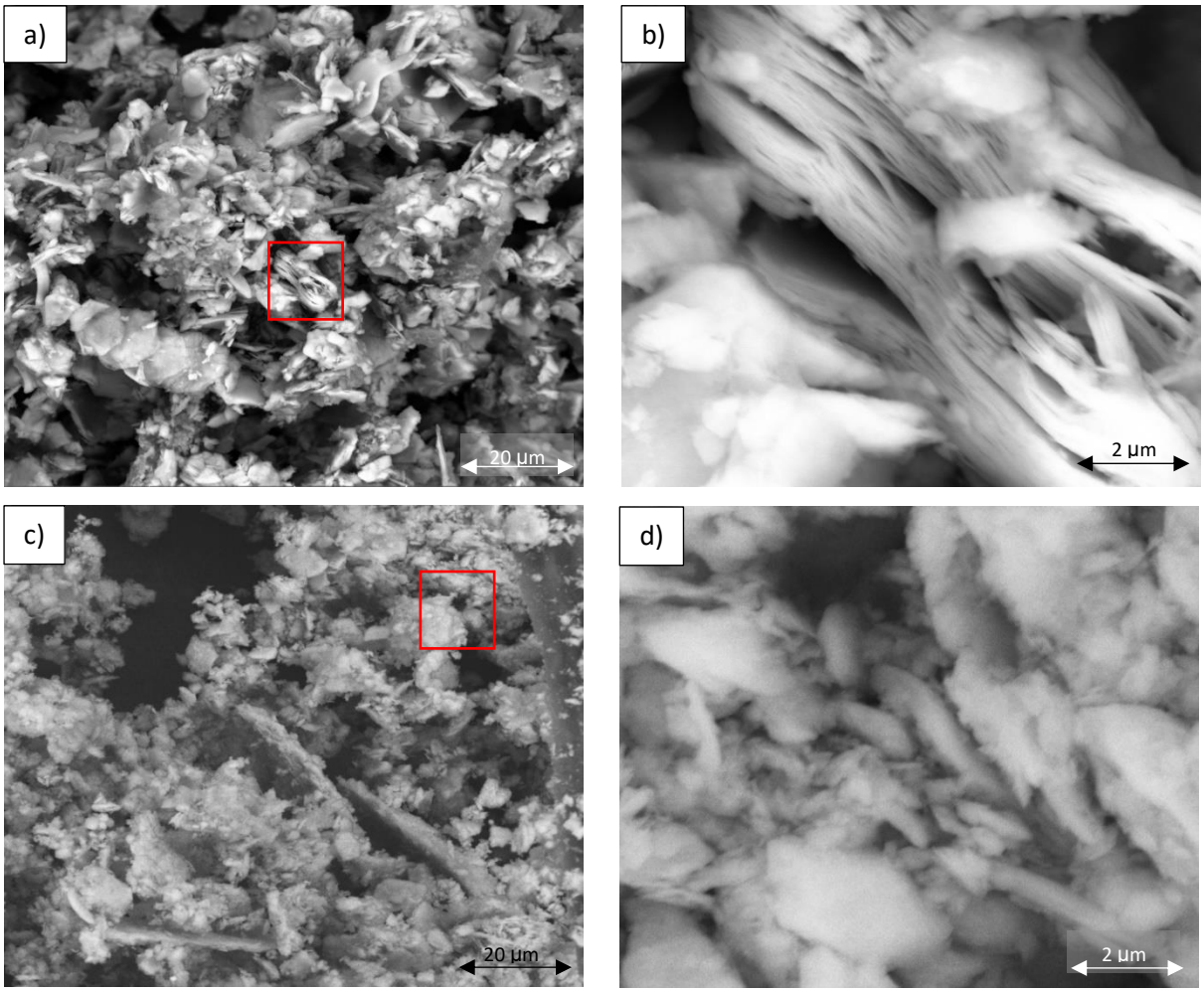


Figure 5.22: SEM image of 0.5 g, 200-mesh $Ti_3C_2T_x$ etched in 10 ml of 48 wt % HF at 30 °C for 24 hours and ground by a), b) mortar and pestle and c), d), micronizor. The particle inscribed in the red square is shown at a higher magnification the adjacent right sided image.

The first change observed after micronizing is significantly reduced lateral flake size d). This is across the bulk of the sample as seen in c). Further, large clusters of delaminated flakes are seen in both images with the once clear edges shrunk and made round. In the case of micronizing, the specific surface area was measured at 5 $m^2/g$. Compared to the as synthesised $Ti_3C_2T_x$, neither mechanical grinding mechanism offers significant changes to the specific surface area of the MXene. Shown in Figure 5.23 are the delaminated flakes after 40 minutes of sonication post grinding by a), b) mortar and pestle and c), d) micronizor. In a), there are now many more delaminated and agglomerated flakes visible when compared to the original sample in Figure 5.18. In b), smaller flakes with rounded edges are observed. The specific surface area for the sample ground by mortar and pestle before being sonicating for 40 minutes was measured as 16 $m^2/g$. This increase confirms that the grinding pre sonicating is effective at attaining an increase in the number of delaminated flakes.

From Figure 5.23 c) and d), it is immediately apparent just how significant an impact the combined micronizing and sonicating method has on the etched flakes. In c), an almost transparent area of delaminated sheets can be seen. This is an indication of how small, light, and concentrated the agglomerated flakes have become. In image d), this is again visible at a higher magnification. The specific surface area for this sample ground by micronizor and sonicated for 40 minutes was measured as 79 $m^2/g$.

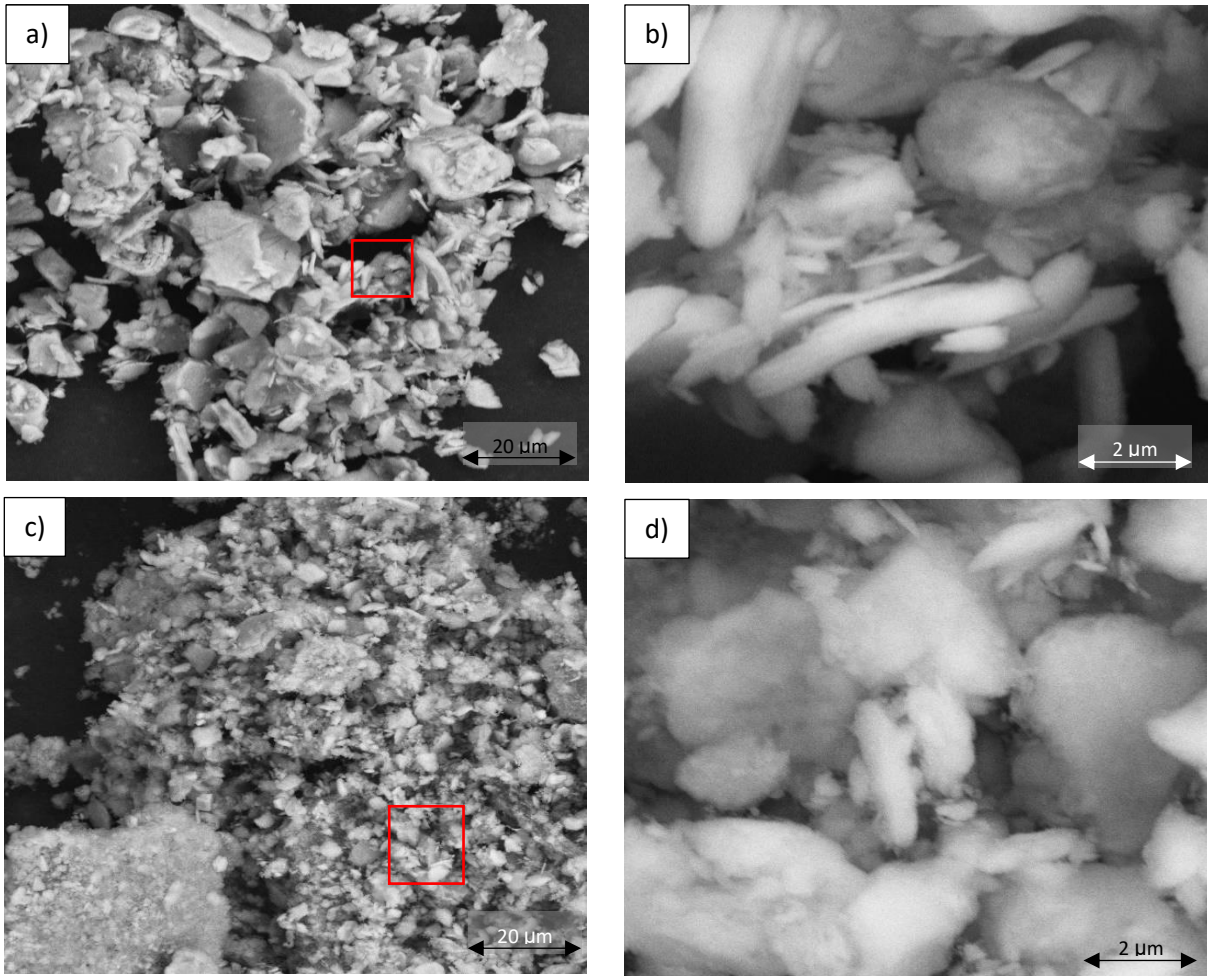


Figure 5.23: SEM images of 0.5 g, 200-mesh $Ti_3AlC_2$ etched in 10 ml 48 wt % HF at 30 °C for 24-hours and ground by a), b) mortar and pestle c), d) sonicator before being probe sonicated for 40 minutes. The particle inscribed in the red square is shown at a higher magnification the adjacent right sided image.

To assess the influence of starting particle size on the MXene's specific surface area, the methodology applied above was applied to the 400-mesh $Ti_3AlC_2$ particles. It was expected following the literature discussed in Section 2.3.2, that by etching MAX phases with a smaller lateral particle size, etching should be completed over a shorter period. It was also expected that by virtue of the starting particles being smaller, once subjected to the processing methodology outlined above, MXene's with a smaller average flake size and higher specific surface area will be synthesized.

The exact same protocols that were applied to the 200-mesh samples shown in Figures 5.21 and 5.23 were applied to the smaller 400-mesh starting particle size, $Ti_3AlC_2$ MAX phase. The XRD shown in Figure 5.24 shows after processing by the same conditions, $Ti_3C_2T_x$ MXene is once more attained.

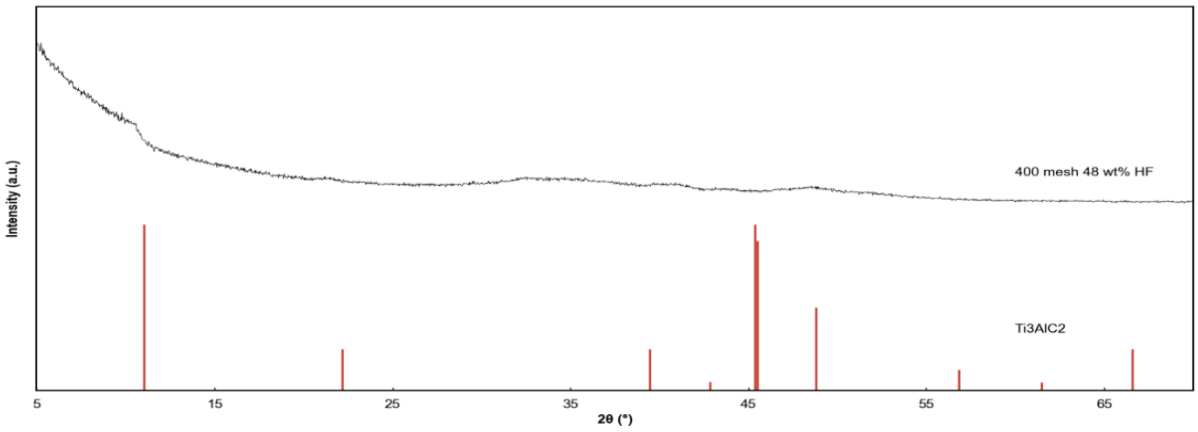


Figure 5.24: XRD diffractogram of 0.5 g, 400-mesh $Ti_3C_2T_x$ etched in 10 ml of 48 wt % HF at 30 °C for 24 hours after micronizing for 10 minutes and probe sonicating for 40 minutes with $Ti_3AlC_2$ reference.

In Figure 5.25, the $Ti_3C_2T_x$ flakes synthesized from 400-mesh $Ti_3AlC_2$ are shown. As seen in a) and b), the flake size has been significantly reduced and large, porous agglomerates formed. With the decreased flake size expected to translate to a higher SSA, the smaller starting particle size is seen as ideal as it avails additional sites for catalyst deposition or platinum anchoring. Further, it is observed that the flake sizes remain polydisperse. This agrees with literature by Maleski et al. (2018), where additional methods in density gradient centrifugation is said to be required to isolate a flake size range.

For this project, this sample is considered adequate even with polydisperse flake sizes. A specific surface area of 86 $m^2\ g^{-1}$ was attained for the sample confirming literature by Wei et al. (2021), that decreasing the MAX phases particle size leads to a decrease in the MXene's flake size.

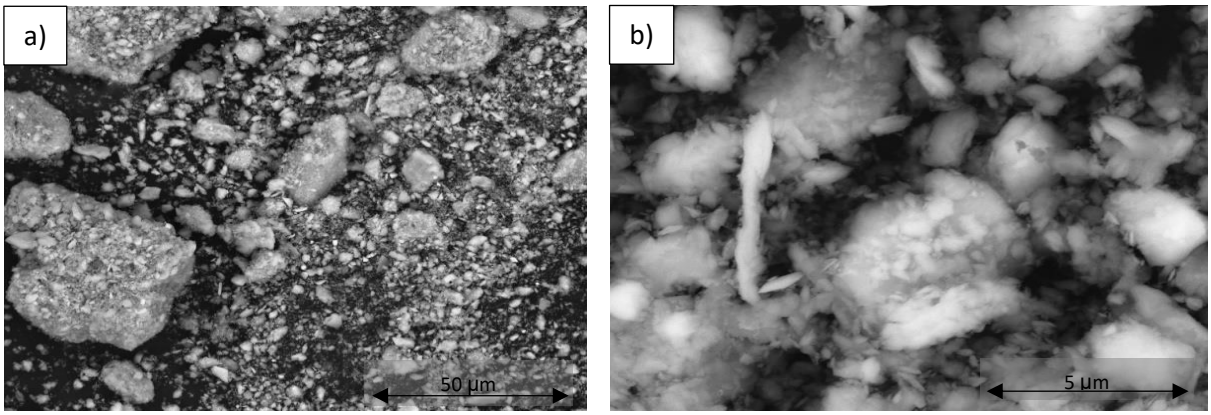


Figure 5.25: SEM images of 0.5 g, 400-mesh $Ti_3C_2T_x$ etched in 10 ml of 48 wt % HF at 30 °C for 24 hours after micronizing for 10 minutes and probe sonicating for 40 minutes

#### 5.2.3.5 Etching Results Summary

In review, the best fit for purpose MXene synthesized under this experimental matrix of mild in-situ HF conditions, was 0.5 g, 200-mesh $Ti_3AlC_2$ etched and delaminated for 24 hours in 20 ml of 10M HCl and 3.33M (or 0.52 g) LiF at 60 °C. This provided a BET SSA of 14 $m^2 g^{-1}$. Table 2 summarises the attained specific surface area from the experimental matrix.

Table 2: $Ti_3C_2T_x$ in-situ HF etched specific surface area by different methods of grinding and sonicating.

| Condition | Specific Surface Area ($m^2 g^{-1}$) |
|---|---|
| MAX Phase Starting Material | 2 |
| 45 °C, 24 hours, 3:1 HCl:LiF molar ratio | 5 |
| 45 °C, 24 hours, 6:1 HCl:LiF molar ratio | 4 |
| 60 °C, 24 hours, 3:1 HCl:LiF molar ratio (optimised) | 14 |

Based on Table 2 and the specific surface area requirement for an advanced catalyst support as outlined by Rabis, Rodriguez & Schmidt, (2012), none of the above meet the > 50 $m^2 g^{-1}$ benchmark. It was therefore required that HF etching be employed. While the results in Section 5.2.3.4 speak only to the 48 wt % HF etched powders, all experimental protocols were repeated and tabulated for the 30 wt % HF materials. These results are shown in Table 3.

Table 3: $Ti_3C_2T_x$ HF etched specific surface area by process method of grinding and sonicating.

| Etchant and time | Size reducing mechanism | SSA ($m^2/g$) |
|---|---|---|
| 24 hours 30 wt % HF (200-mesh) | None | 6 |
| | Sonication only | 17 |
| | Mortar & pestle | 6 |
| | Mortal & Pestle + sonication | 20 |
| | Micronizor | 5 |
| | Micronizor + sonication | 64 |
| 24 hours 48 wt % HF (200-mesh) | None | 6 |
| | Sonication only | 18 |
| | Mortar & pestle | 5 |
| | Mortal & Pestle + sonication | 16 |
| | Micronizor | 5 |
| | Micronizor + sonication | 79 |
| 24 hours 48 wt % HF (400-mesh) | Micronizor + sonication | 86 |

Based on the specific surface area requirements set out Rabis, Rodriguez and Schmidt (2012), for an advanced catalyst support to facilitate ORR, only those samples micronized prior to sonication are suitable having attained SSA's greater than 50 $m^2 g^{-1}$. With the 400-mesh $Ti_3AlC_2$ has the highest specific surface area of the analysed matrix, this powder was selected for use in the electrochemical performance evaluation section of this work.

## 5.3 Electrochemical Performance Evaluation

### 5.3.1 Platinum on Carbon Baseline Activity Measurements

As a baseline for the electrochemical evaluation on the $Ti_3C_2T_x$ catalyst support to follow, an analysis was first conducted on a commercial 40 wt % platinum on carbon (Pt/C), catalyst. This served to provide a fair, comparative standard. It further allowed the rigour of the methodology to be critically evaluated. The TEM images for this, commercial catalyst are shown in Figure 5.26 in images a) and b) at different magnifications. As seen from the histogram in c), after measuring 100 particles, the average particle size is in the region of 2-4 nm. This particle size agrees with literature from Tran et al. (2016), where the platinum particle size was investigated for the same loading and was found to be within the same region. As seen from a) and b), a high dispersion with fairly constant interparticle distance is also observed in the commercial catalyst.

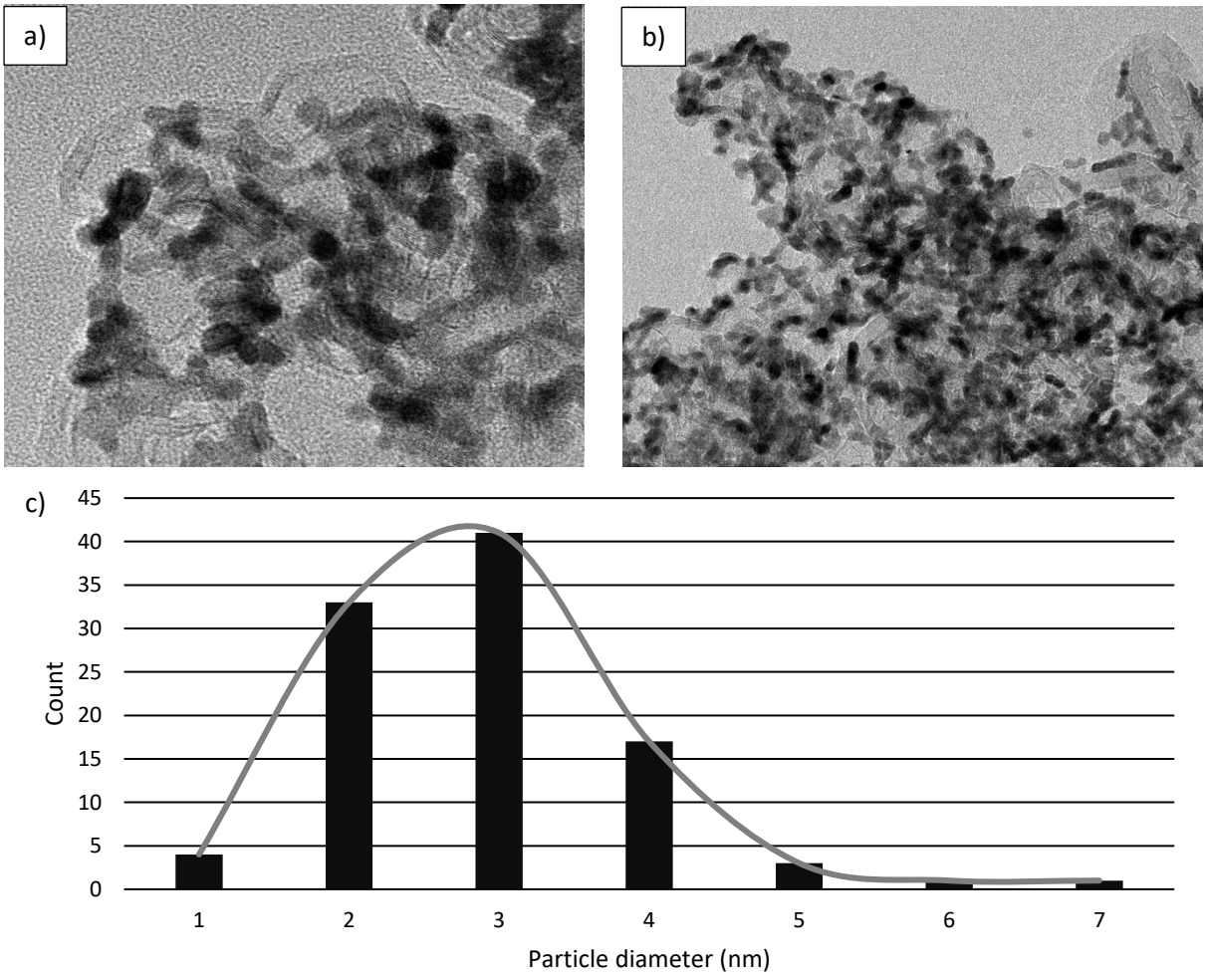


Figure 5.26: TEM images of a 40 wt % Pt/C commercial catalyst at different magnifications a) and b) with the histogram c) showing of the corresponding platinum particle size distribution.

In this work, all cyclic voltammograms were recorded at 50 mV/s after cycling at 100 mV/s for 50 cycles. This pre-measurement cycling was performed to remove any by products or oxides formed on the catalyst film. In Figure 5.27, the first cyclic voltammogram for the commercial catalyst is displayed. These measurements were taken in an electrolyte solution of 0.10 M $HClO_4$ after formulation of the catalyst ink, polishing of the electrode surface, and catalyst deposition onto its surface as per Sections 4.4.3 to 4.4.5. In Figure 5.27 the typical hydrogen adsorption-desorption peaks are clearly visible in the region between 0 and 0.3 V vs RHE. The platinum oxidation region between 0.7-1.2V vs RHE and oxide reduction peak around 0.8 V vs RHE on the reverse can also be clearly observed.

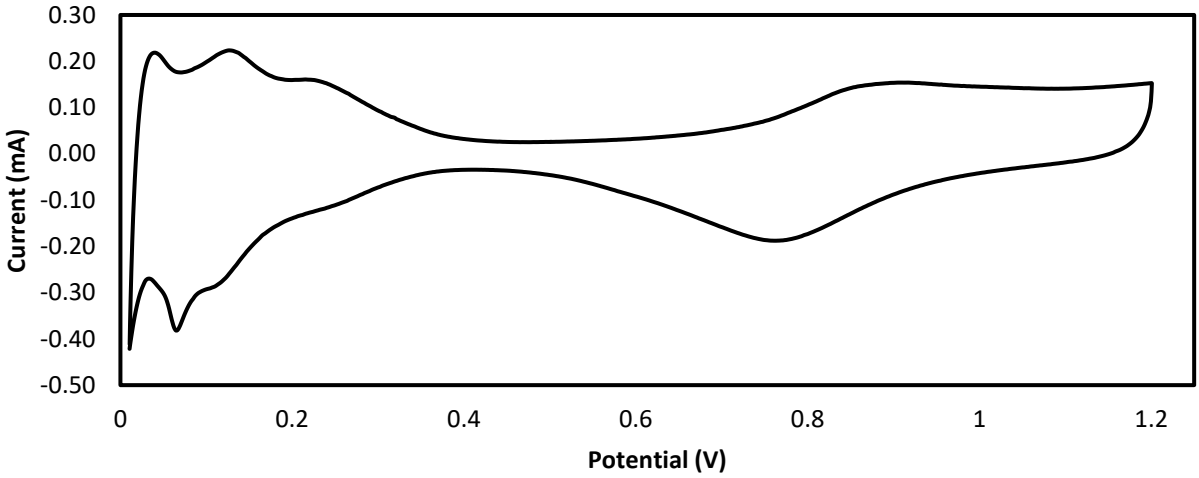


Figure 5.27: First cyclic voltammogram from 0.01 to 1.2 V versus RHE of a 40 wt % Pt/C catalyst recorded at 50 mV/s in 0.10 M deoxygenated $HClO_4$ solution recorded at room temperature.

To calculate the ECSA, the charge was determined as 0.511 mC by integrating the positive region between the hydrogen underpotential and the double layer plateau after extrapolation. Using a charge of 210 µC $cm^{-2}$ for the monolayer adsorption of atomic hydrogen in the electrolyte as per Section 4.4.5, and by then determining the Pt loading from the ink formulation, catalyst synthesis and electrode deposition, the electrochemically active surface area of 80 $m^2$ $g^{-1}$ was determined as per Equation 17 (Garsany et al., 2010).

$$ECSA\ \left(\frac{cm^2}{gPt}\right) = \frac{Charge\left(\frac{\mu C}{cm^2}\right)}{210\left(\frac{\mu C}{cm^2}\right)\cdot Pt\ loading\left(\frac{gPt}{cm^2}\right)} = \frac{(1000\cdot 0.5108/0.196)}{210\cdot\frac{4.99\cdot 10\ \cdot 0.40}{1000\cdot(6500+25)}\cdot\frac{1}{0.196}} = 79.5\ m^2/gPt \quad (17)$$

This agrees with typical literature values where a 40 wt % Pt/C catalyst was found to have an ECSA in the region from 74.5 to 87.4 $m^2$ $g^{-1}$ (Fu et al., 2016; Taylor et al., 2016). The above analysis was repeated using the same catalyst, but with a re-developed ink in a fresh electrolyte solution. This also meant the electrode surface would have to be cleaned and polished before catalyst deposition could be performed again. The cyclic voltammogram recorded from this analysis is shown in Figure 5.28.

As seen in Figure 5.28, the cyclic voltammogram clearly indicates the presence of the hydrogen adsorption-desorption, the platinum oxidation region, and oxide reduction peak. By performing the same integration as above, a charge of 0.495 mC relating to an ECSA of 77 $m^2 g^{-1}$ was determined. The results both agree with literature and are within 5 % of each other thus indicating that the laboratory setup, ink preparation and film quality are reliable.

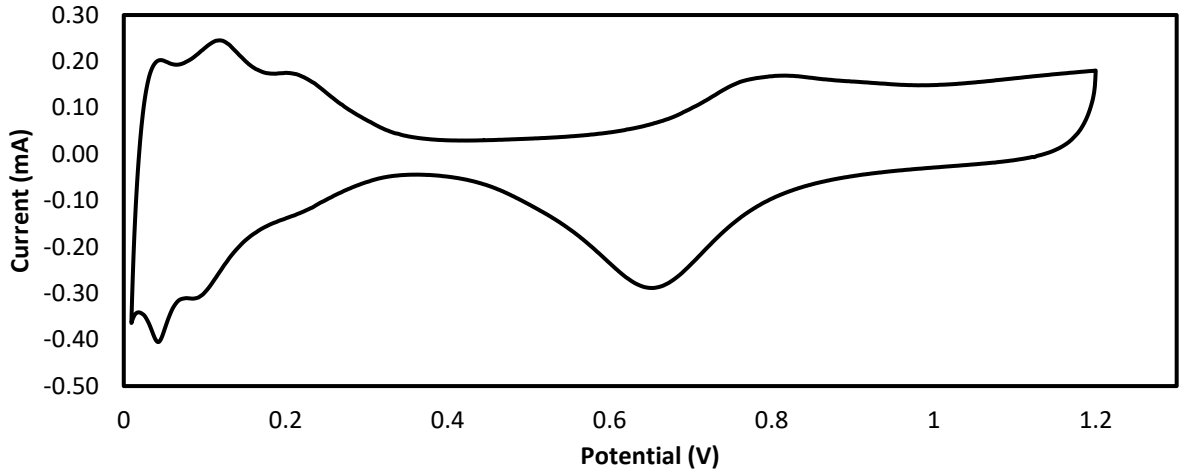


Figure 5.28: Second cyclic voltammogram from 0.01 to 1.2 V versus RHE of a 40 wt % Pt/C catalyst recorded at 50 mV/s in 0.10 M deoxygenated $HClO_4$ solution recorded at room temperature.

To determine the mass specific and surface specific activity, linear sweep voltammetry with a rotating disk electrode (RDE), was recorded at different rotation speeds of 400, 900, 1600 and 2500 RPM as per Section 4.4.5. This analysis was performed using the second baseline catalyst for the Pt/C electrochemical performance evaluation and followed straight after. The obtained curves were corrected for iR drop and background current in accordance with Equation 16 and are shown in Figure 5.29. In this report, only the cathodic current will be referenced which speaks to the positive current.

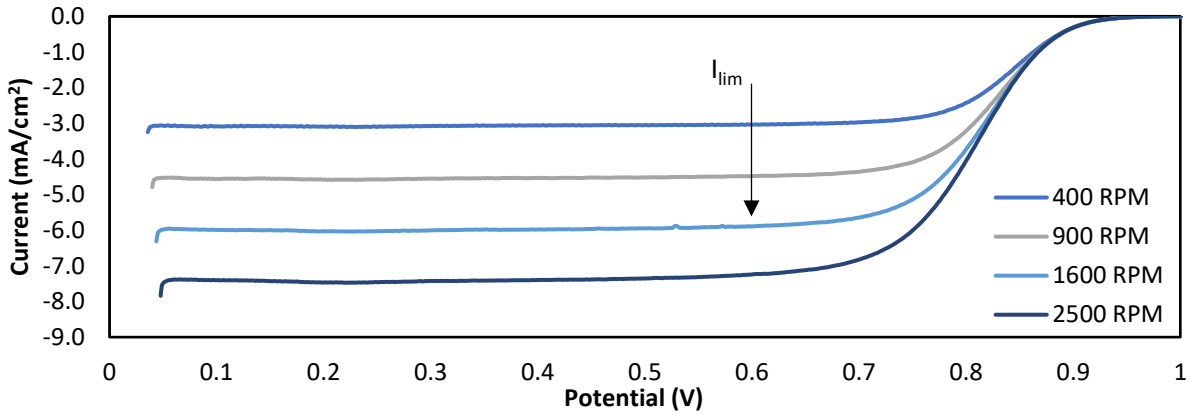


Figure 5.29: Linear sweep curves corrected for IR drop and background current for a 40 wt % Pt/C catalyst in 0.1M $HClO_4$ solution recorded at room temperature.

In Figure 5.29 the typical shape of the curves is obtained for all rotation speeds (Wang et al., 2015). In addition, for all rotation speeds, the curves came close to the theoretical limiting current as shown in Table 4. The Levich Equation used for Table 4 assumes a 4 $e^-$ transfer with a diffusion co-efficient, $O_2$ concentration and kinematic viscosity for a $O_2$ saturated 0.10 M solution.

Table 4: Corrected current densities of the linear sweep curves for a 40 wt % Pt/C catalyst from an RPM range of 400 to 2500 RPM referenced against results from the Levich Equation.

| RPM | Obtained Value (mA/cm$^2$) | Theoretical Limiting Current (mA) |
|---|---|---|
| 400 | 3.05 | 3.02 |
| 900 | 4.40 | 4.53 |
| 1600 | 6.05 | 6.04 |
| 2500 | 7.50 | 7.55 |

The limiting cathodic current corresponds to the current whereby movement from the equilibrium potential offers no marginal increase in mass transport over a finite range. This was read off the plateau in Figure 5.29 as 6.05 mA/cm$^2$ which is equivalent to 1.19 mA (with A = 0.196 cm$^2$). Using the current from Figure 5.29, at 0.9V for the electrode rotated at 1600 RPM (0.08 mA), the activity ($I_k$) with a cathodic current of 0.087 mA was attained in accordance with Equation 19.

$$\frac{1}{I} = \frac{1}{I_k} + \frac{1}{I_{lim}} \tag{19}$$

Finally, the kinetic specific activity is attained as per Equation 20:

$$KSA = \frac{I_k}{Pt\ (mass) \cdot ECSA} = \frac{0.086\ (mA)}{2.99 \cdot 10^{-6}\ (gPt) \cdot 795\ 155\left(\frac{cm^2}{gPt}\right)} = 35.36 \frac{\mu A}{cm^2} \tag{20}$$

Similarly, the mass specific activity (MSA), was calculated in accordance with Equation 21.

$$MSA = \frac{I_k}{Pt\ (mass) \cdot} = \frac{0.086\ (mA)}{2.99 \cdot 10^{-3}\ (mgPt)} = 29.10 \frac{mA}{mg} \tag{21}$$

The values attained for the KSA and MSA are within range of literature indicating that a successful standard for the comparison of the $TiC_2T_x$ catalyst support has been established (Taylor et al., 2016).

### 5.3.2 Platinum on MXene Activity Measurements

As per Section 5.2.2, in-situ HF etching was unable to provide a high surface area support. With HF etching, the accordion like morphology was attained and after micronizing and sonicating, the material was transformed into a relatively high (>50 m$^2$ g$^{-1}$), surface area support as seen in Table 3. With a smaller MAX phase starting particle size of 400-mesh from 200-mesh, the SSA after synthesis and processing was seen to increase. With the XRD confirming all the material had been transformed from a MAX to MXene, the 400-mesh starting material etched for 24 hours in 48 wt % HF before being micronized and probe sonicated for 40 minutes, was selected for electrochemical performance evaluation. For the MXene supported catalysts, three were synthesized.

All MXene based catalysts were synthesized using metal organic chemical deposition which took place at 350 °C for 4 hours as per Section 4.2. The objective was first to find an active catalyst before assessing its stability in an accelerated durability test.

#### 5.3.2.1 21 wt % (40 eq. wt % Pt/C) Platinum Deposited on $Ti_3C_2T_x$

The first catalyst synthesized was based off an equivalent Pt/C loading of 40 wt %. This loading was selected as it served to provide a starting point by relating an equivalent Pt/C particle distribution and interparticle distance to the Pt/MXene catalyst. With approximately a third of the specific surface area (measured at 227 vs 87 $m^2 g^{-1}$), the equivalent loading on this catalyst was calculated as 21 wt %. This equivalent loading was calculated by scaling the platinum mass by the ratio of the SSA of the commercial to the MXene support materials. This was designated such that the $Ti_3C_2T_x$ based catalyst has the same Pt mass per unit support surface area as the commercial catalyst. TEM imaging of this catalyst is shown in Figure 5.30. By comparison to Figure 5.26, the desired dispersion and interparticle distance shown in a) and b) was successfully attained. This is confirmed as the platinum nanoparticles are well distributed on the surface of the $Ti_3C_2T_x$ support. Figure 5.30 c) shows the average particle size measured around 3 nm. The above indicates a successful catalyst deposition onto $Ti_3C_2T_x$.

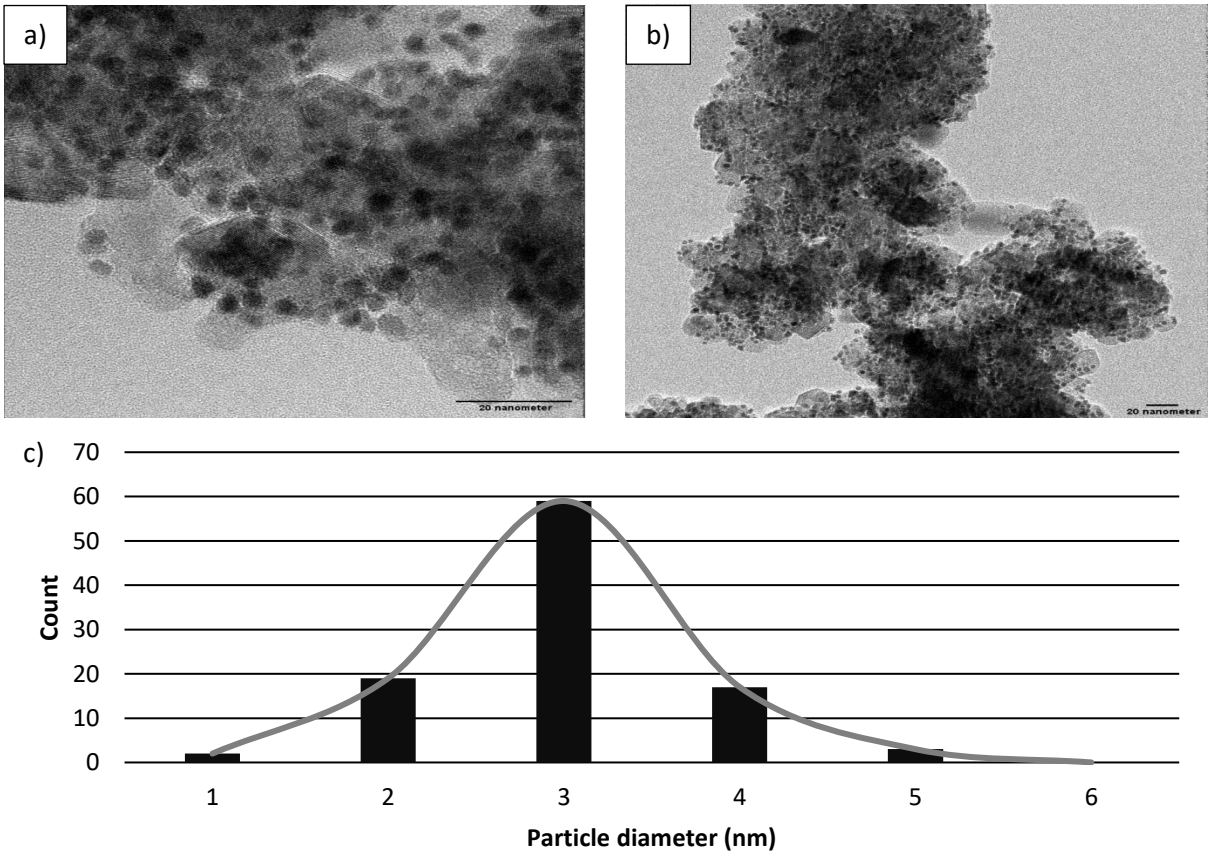


Figure 5.30: TEM images of a 40 eq. wt % Pt/C to Pt/MXene catalyst at different magnifications a) and b) with the histogram c) showing of the corresponding platinum particle size distribution.

After performing an electrochemical performance evaluation on the above catalyst, no part of the surface was found to be electrochemically active. This is shown in Figure 5.31. As per the platinum on carbon analysis, all cyclic voltammograms in this section were recorded at 50 mV/s after cycling at 100 mV/s for 50 cycles to remove any by products or oxides formed on the catalyst film. No activity measurements were recorded for this catalyst as it would prove insignificant after already having determined no electrochemically active surface area available. To further understand this higher Pt loadings were attempted.

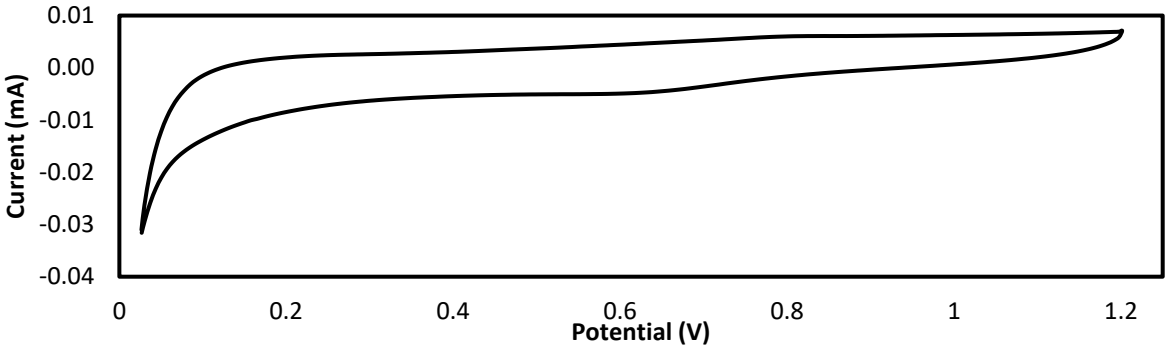


Figure 5.31: Cyclic voltammogram from 0.01 to 1.2 V versus RHE of a 40 eq. wt% Pt/C to Pt/$Ti_3C_2T_x$ catalyst recorded at 50 mV/s in 0.10 M deoxygenated $HClO_4$ solution at room temperature.

#### 5.3.2.2 40 wt % (78 eq. wt% Pt/C) Platinum Deposited on $Ti_3C_2T_x$

The second catalyst synthesized was 40 wt % Pt/MXene. While this is a high loading for this support material, it was selected as the results from the first catalyst had no indicative ECSA. The TEM images and particle size distribution histogram are shown in Figure 5.32, images a) and b) and c, respectively.

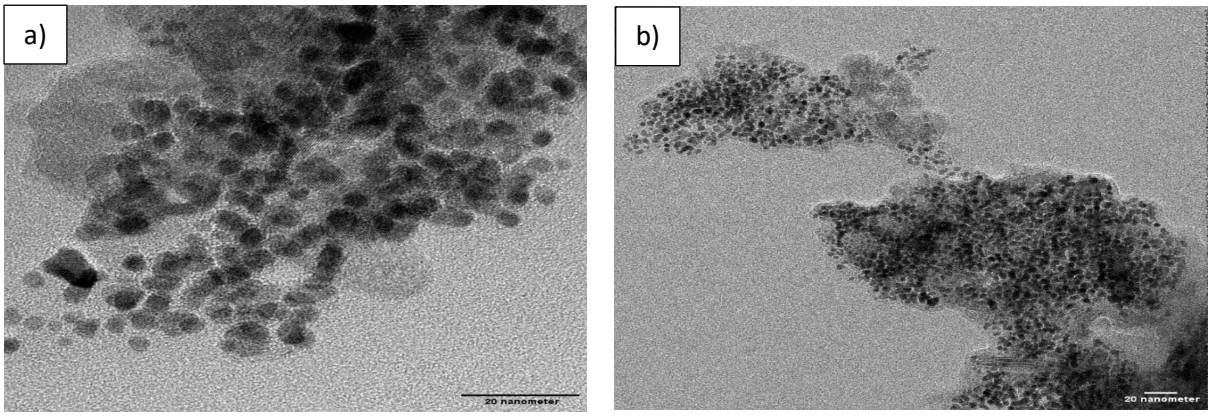


Figure 5.32: TEM images of a 40 wt % Pt/$Ti_3C_2T_x$ catalyst at different magnifications a) and b). Corresponding particle size distribution shown in Figure 5.33.

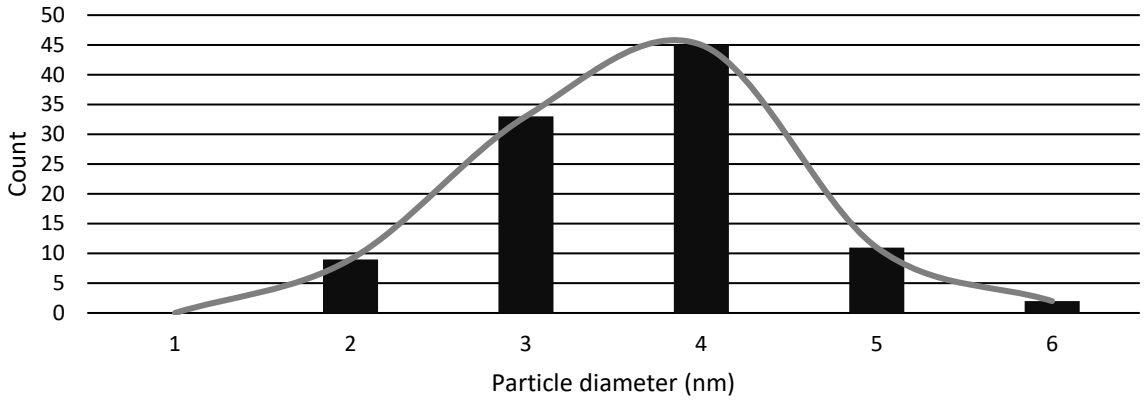


Figure 5.33: Platinum particle size distribution of a 40 wt % Pt/$Ti_3C_2T_x$ catalyst corresponding to TEM images a) and b) in Figure 5.32.

From Figure 5.32, in a) uniformity and adequate dispersion is observed. In b), clusters of platinum particles are seen in some regions, and unutilized support regions seen in others. In the bottom right side of this image, the density of this loading can be seen. From Figure 5.33, an adequate platinum particle size distribution is, however, still maintained. The above indicates that while the MOCD method remains fit for purpose, this loading is considerably high for the $Ti_3C_2T_x$.

The cyclic voltammogram for this catalyst is shown in Figure 5.34. While a semblance of electrochemically active surface area exists, it was considered insignificant and not warranting of further activity measurements.

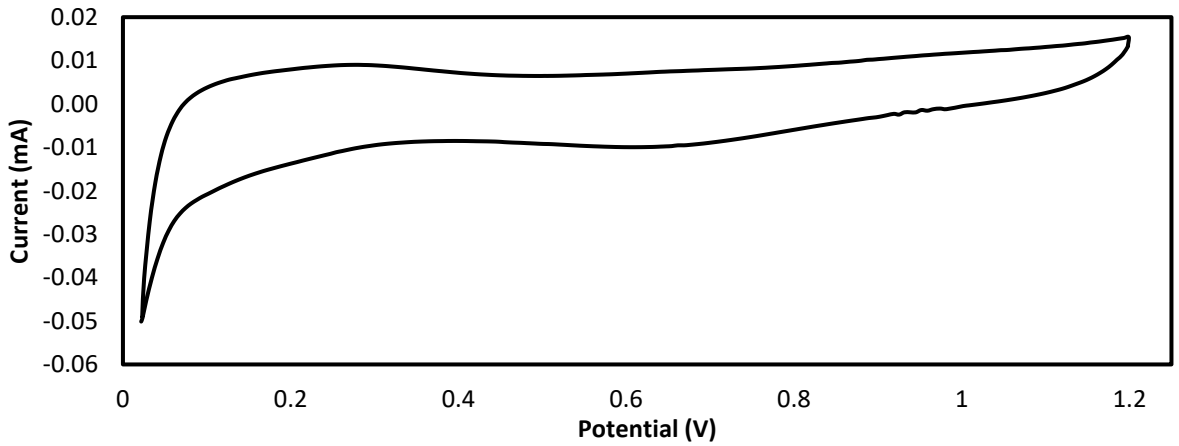


Figure 5.34: Cyclic Voltammogram from 0.01 to 1.2 V versus RHE of a 40 wt % Pt/MXene catalyst recorded at 50 mV/s in 0.10 M deoxygenated $HClO_4$ solution at room temperature.

It was suspected that the lack of activity from this catalyst was due to an insufficiently conductive support material. This relates back to findings by Maleski et al. (2018), where it was discovered that while smaller flake sizes provide more active sites for deposition, which in turn enables better electrolyte accessibility, decreasing $Ti_3C_2T_x$ lateral flake size, decreases its conductivity.

Based on the specific surface area (>50 $m^2$ $g^{-1}$), requirement outlined by Rabis, Rodriguez & Schmidt, (2012), a constraint therefore exists between conductivity and SSA. It is therefore recommended that considerations to the conductivity of the support material be undertaken to develop the catalysts conductivity within the SSA requirement. To overcome the suspected conductivity issues carbon was added to the catalyst film.

#### 5.3.2.3 40 wt % (78 eq. wt% Pt/C) Platinum Deposited on $Ti_3C_2T_x$ after Carbon Addition

The final catalyst synthesized was a 46 wt % Pt catalyst mixed with additional carbon at the ink formulation stage. This loading reduced the amount of Pt on the surface of the electrode to that equivalent to the 40 wt % Pt/C previously tested in Section 5.3.2.2. This ink formulation was selected after reviewing literature by Fabbri et al. (2014), who found that composite electrodes utilizing both a support material and acetylene black were able to increase electron transfer by a factor of 3.5 to either individual material. The 15 wt % of Vulcan 72XC was thus introduced into the ink. For this catalyst and in Figure 5.34 a), b) is the TEM imaging showing platinum dispersion and interparticle distance prior to carbon addition. Shown in c), d) is the same catalyst after carbon addition. As mentioned, the carbon was added at the ink formulation stage and then bath sonicated post platinum deposition onto the MXene support.

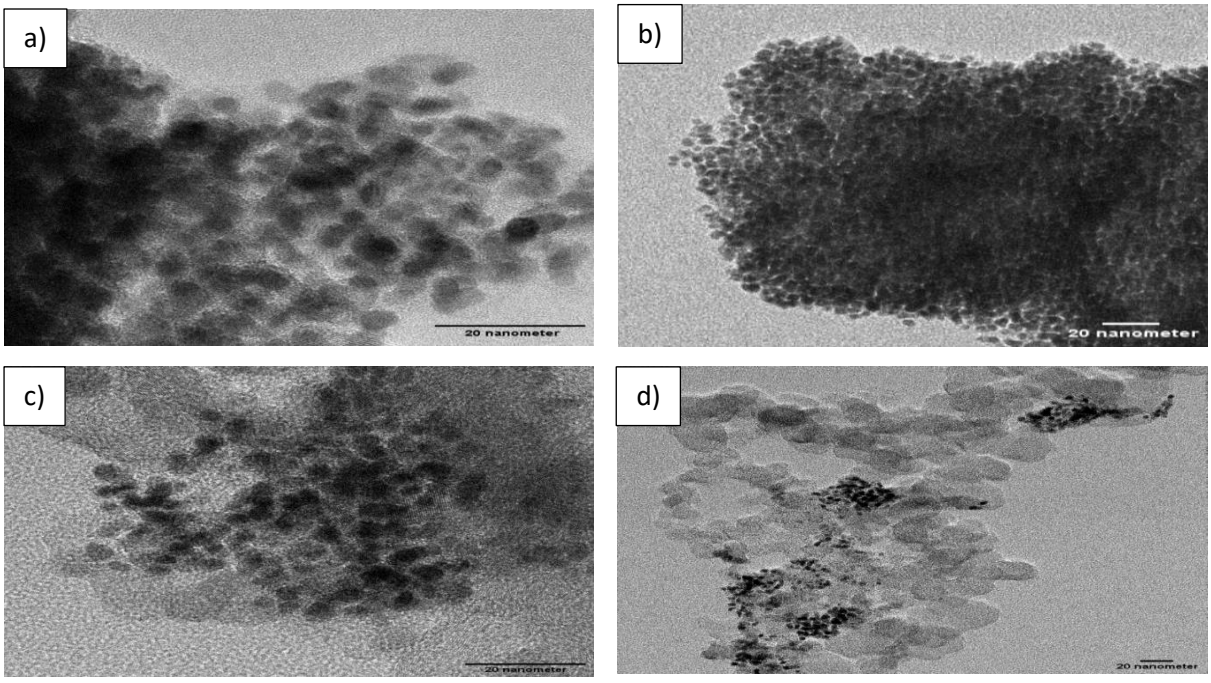


Figure 5.35: TEM images of the 46 wt % Pt/MXene at different magnifications a), b). Images c), d) show the catalyst after carbon addition (to 15 wt % of the catalysts total mass), post bath sonication for 30 minutes.

As can be seen in Figure 5.35 c) and d), the high surface area carbon (225 $m^2$ $g^{-1}$), disperses the $Pt/Ti_3C_2T_x$ catalyst. It is anticipated that the addition of the carbon will allow for better electron conductivity to and from the catalyst sites. The particle size distribution was recorded from the original catalyst before dispersion with carbon as this allowed more particles to be accumulated into the analysis. From the histogram shown in Figure 5.36, particles remain around the desired 3 nm size even while their dispersion and interparticle distance shown in Figure 5.35 b) is considerably lower than the commercial catalyst shown in Figure 5.26.

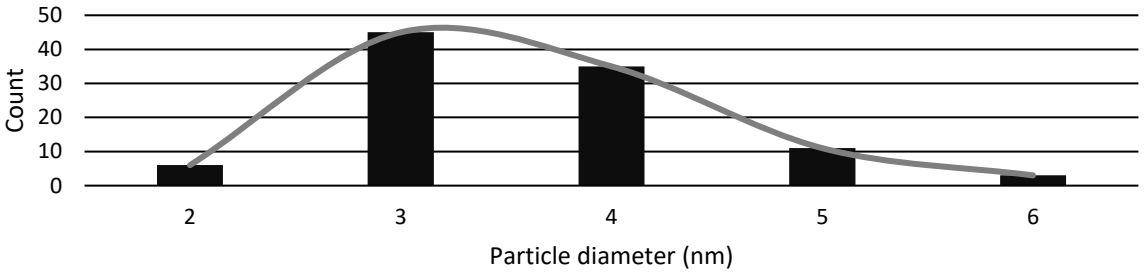


Figure 5.36: Histogram of Pt particle size distribution based off TEM imaging from Figure 5.35 a), b) showing Pt dispersion and inter particle distance for the 46 wt % Pt/MXene.

From the cyclic voltammogram for this catalyst shown in Figure 5.37, the desorption of hydrogen from Pt (110) sites and the desorption of hydrogen from Pt (100) sites are visible in the expected 0 – 0.3 V regions. The Pt oxidation region (0.7 – 1.2 V) as well as the oxide reduction peak (about 0.75 V) are also visible. Lastly, the double layer, a non-faradaic current due to current which must flow to charge an electrode interface upon a change in applied potential is also visible. With the above elements all visible, a favourable interaction between the carbon and catalyst is seen to exist. This confirms the observation by Fabbri et al. (2014).

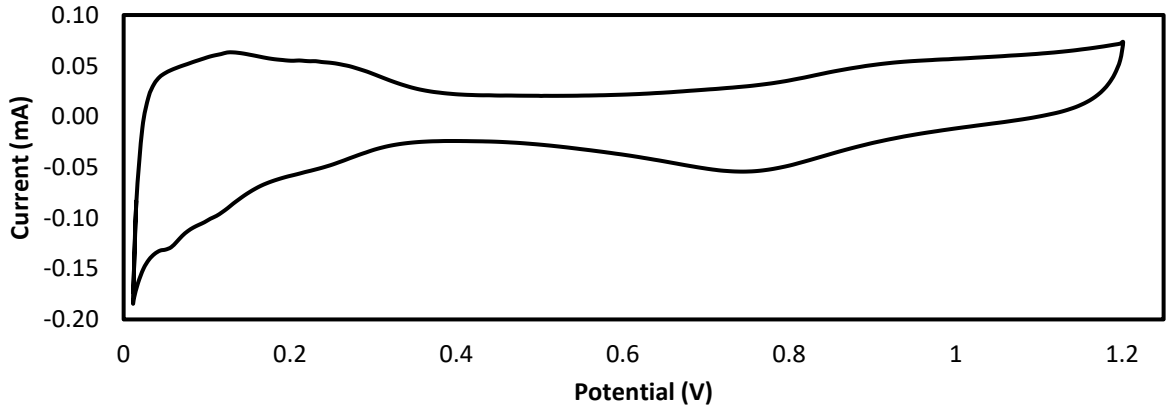


Figure 5.37: Cyclic Voltammogram from 0.01 to 1.2 V versus RHE of a 46 wt % Pt/MXene catalyst + 15 wt % carbon recorded at 50 mV/s in 0.10 M deoxygenated $HClO_4$ solution at room temperature.

The charge was determined from the cyclic voltammogram shown in Figure 5.37, by integrating the region under the hydrogen desorption peak as 0.1739 mC. The electrochemically active surface area of the catalyst was subsequently determined as 28 $m^2\ g^{-1}$ as shown in Equation 22. While this is less than half of that of a 40 wt % Pt/C catalyst (80 $m^2\ g^{-1}$), it was deemed acceptable for further electrochemical measurements to follow in the form of activity and durability testing.

$$ECSA\ \left(\frac{cm^2}{gPt}\right) = \frac{Charge\ \left(\frac{\mu C}{cm^2}\right)}{210\ \left(\frac{\mu C}{cm^2}\right) \cdot Pt\ loading\ \left(\frac{gPt}{cm^2}\right)} = \frac{(1000 \cdot 0.1739/0.196)}{210 \cdot \frac{5.01 \cdot 10 \cdot 0.46}{1000 \cdot (6500+25)} \cdot 0.85 \cdot \frac{1}{0.196}} = 28.6\ m^2/gPt \qquad (22)$$

For an activity comparison to the commercial catalyst, linear sweep voltammetry was performed. After normalizing both the voltage and current, the linear sweep profiles are shown in Figure 5.38.

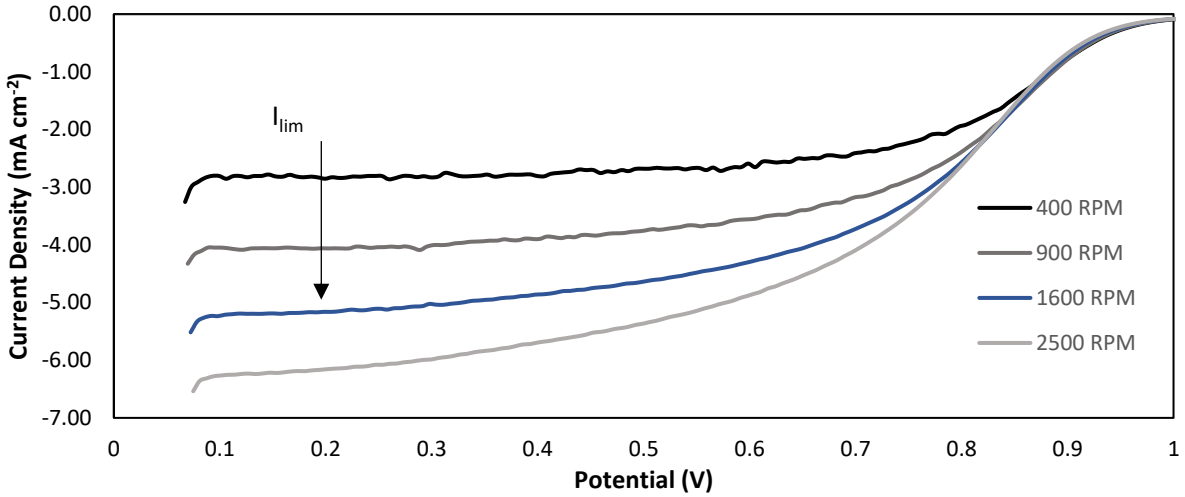


Figure 5.38: Linear sweep curves corrected for IR drop and background current for a 46 wt % Pt/MXene catalyst + 15 wt % carbon catalyst in 0.10 M $HClO_4$ solution recorded at room temperature.

From Figure 5.38, it is evident that electrical transport limitations play a significant role in what is limiting both the electrochemically active surface area, and by virtue, the kinetic surface activity. This is visible by the significant over-potential required before the limiting current is attained.

The limiting cathodic current was read off Figure 5.38 as indicated and was equal to 5.1 mA $cm^{-2}$ or 1.02 mA by using A = 0.196 $cm^2$. This is significantly lower than the theoretical limiting current of 6.02 mA $cm^{-2}$ and hence the activity parameters calculated below can only be regarded as indicative numbers as the correction through Koutecky-Levich is not entirely reliable with the obtained limiting current. Thus, solving for the activity ($I_k$) using the Koutecky-Levich, a current of 0.204 mA was attained. Finally, the kinetic specific activity and mass specific activity is attained as per Equations 23 and 24 shown respectivelty.

$$KSA = \frac{I_k}{Pt\ (mass) \cdot ECSA} = \frac{0.204\ (mA)}{2.99 \cdot 10^{-6}\ (gPt) \cdot 327\ 084\ \left(\frac{cm^2}{gPt}\right)} = 0.208 \frac{mA}{cm^2} = 208 \frac{\mu A}{cm^2} \quad (23)$$

$$MSA = \frac{I_k}{Pt\ (mass)} = \frac{0.204\ (mA)}{2.99 \cdot 10^{-3}\ (mgPt)} = 0.208 \frac{mA}{cm^2} = 68.23 \frac{mA}{mgPt} \quad (24)$$

The above shows that while the catalyst is active, due to electron transport limitations introduced by the support material it remains limited in its ability to facilitate the oxygen reduction reaction.

### 5.3.3 Platinum on MXene Durability Measurements

The final assessment of the electrochemical performance evaluation was to determine the durability of the support material. With the addition of the carbon to the support, it would be difficult to deconvolute between carbon or MXene corrosion which would have similar results as platinum is lost to solution. An approach to instead assess the platinum corrosion was therefore undertaken. This would allow the assessment of the metal support interaction. To this end, a scan rate of 50 mV $s^{-1}$ cycling between 0.6 and 1.0 V vs RHE was used and the ECSA was measured after 100, 1000 and every thousand thereafter up to 5000 cycles or until no electrochemically active surface area remains. These conditions were replicated from works by Jackson et al. (2017). The result of this analysis is shown in Figure 5.39. Much like in the previous experiment, a starting ECSA of around 26 $m^2$ $g^{-1}$ is attained. After 3000 cycles, no more recordings were performed as the ECSA reduction had reached such an extent that no more peaks could be observed. Table 5 summarises the evolution of ECSA by cycle.

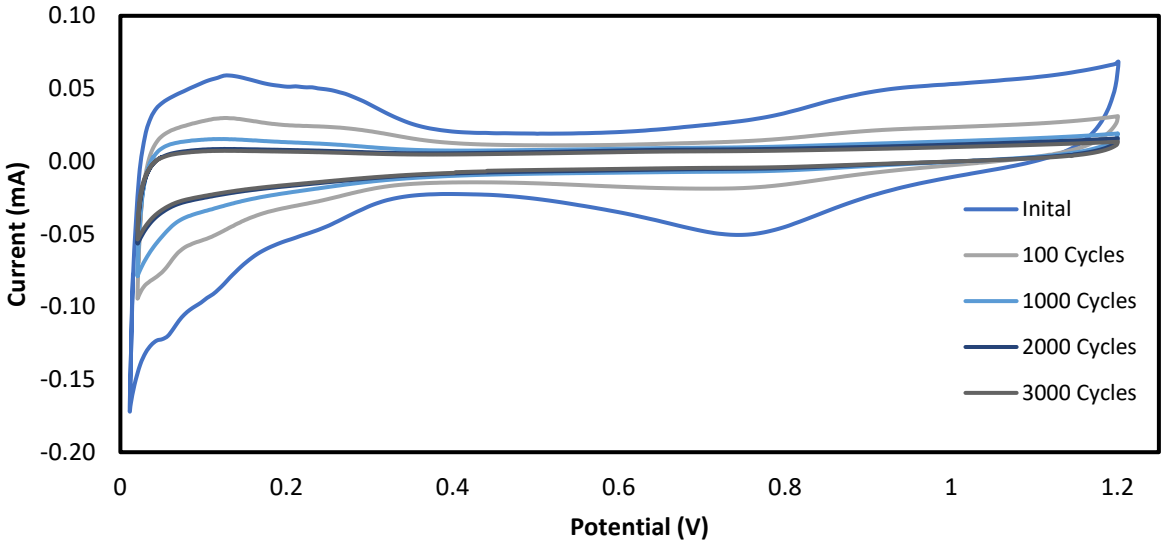


Figure 5.39: Metal support durability measurements recorded up to 3000 cycles from 0.01 to 1.2 V versus RHE for a 46 wt % Pt/MXene catalyst + 15 wt % carbon catalyst recorded in 0.10 M deoxygenated $HClO_4$ solution at room temperature.

Table 5: Electrochemical surface area results summary for a 46 wt % Pt/MXene catalyst + 15 wt % carbon catalyst recorded in 0.10 M deoxygenated $HClO_4$ solution at room temperature.

| Cycles | ECSA ($m^2\ g^{-1}$) |
|---|---|
| Initial | 25.77 |
| 100 | 17.19 |
| 1000 | 5.73 |
| 2000 | 1.70 |
| 3000 | 0.00 |

### 5.3.4 Platinum on Carbon Durability Measurements

For comparative purposes, the same accelerated durability analysis as above was performed for the commercial Pt/C catalyst. These cyclic voltammogram results are shown in Figure 5.40.

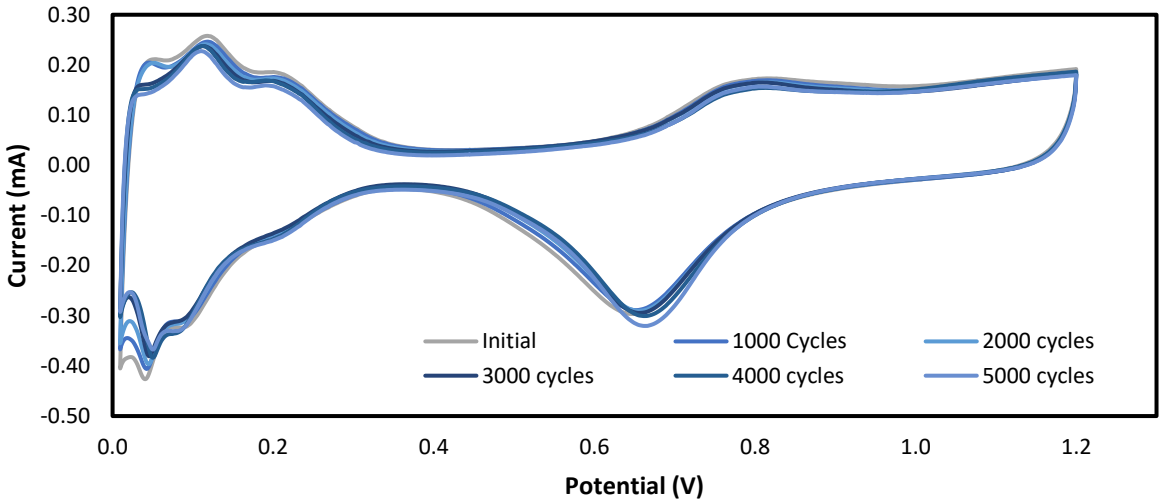


Figure 5.40: Metal support durability measurements recorded to 5000 cycles from 0.01 to 1.2 V versus RHE for a 40 wt % Pt/C catalyst recorded in 0.10 M deoxygenated $HClO_4$ solution at room temperature.

It is immediately evident from Figure 5.40 that the carbon support holds a significantly better metal support interaction. Unlike with the MXene catalyst support, which was rendered inactive after 3000 cycles, for the carbon catalyst support, even after 5000 cycles the Pt features were clearly still visible. This, from Figure 5.40 is clear as both the hydrogen adsorption-desorption and oxide reduction peaks are visible as well as the Pt oxidation region even after the 5000$^{th}$ cycle. Table 6 summarises this electrochemical surface area evolution by cycle.

From Figure 5.39 and Table 5, it is clear that a very poor metal support interaction exists for the Pt/MXene catalyst. After the first 100 cycles approximately 35 % of electrochemical surface area is lost due to poor catalyst anchoring. By comparison, from Figure 5.40 and Table 6, even after 5000 cycles for the Pt/C catalyst, this sort of reduction is not seen.

Table 6: Electrochemical surface area results summary for a 40 wt % Pt/C catalyst recorded in 0.10 M deoxygenated $HClO_4$ solution at room temperature.

| Cycles | ECSA ($m^2\ g^{-1}$) |
|---|---|
| Initial | 74.80 |
| 1000 | 73.91 |
| 2000 | 72.74 |
| 3000 | 65.44 |
| 4000 | 63.33 |
| 5000 | 59.95 |

The above results agree with literature from Jackson et sal. (2017), who, for a catalyst with the same loading, noted a 23 % ECSA loss (after 6000 cycles), vs the 20 % herewith shown (after 5000 cycles).

# Chapter Six: Overall Discussion

The synthesis of the catalyst support material was attempted first with mild in-situ HF conditions. While this method could both etch and delaminate flakes in a single stage, because the flake size remained large and unchanged, the specific surface area attained of 14 $m^2$ $g^{-1}$, did not satisfy the outlined requirements of 50 $m^2$ $g^{-1}$ (Rabis, Rodriguez & Schmidt, 2012). Using the in-situ method here reported, it was possible to attain flake sizes around 10 µm, as shown in Figure 5.11. While it was reported by Alhabeb et al. (2017) and Maleski et al. (2018), that larger flakes are more conductive, due to the specific surface area requirement for an advanced catalyst support, smaller flakes had to be utilized.

To synthesize $Ti_3C_2T_x$ flakes with a high specific surface area, HF etching was utilized. Here, 0.5 g of 400-mesh $Ti_3AlC_2$ flakes synthesized by hot pressing was etched in 48 wt % HF for 24 hours at 30 °C. After micronizing for 10 minutes and sonicating for a further 40 minutes, high surface area MXene flakes of 86 $m^2$ $g^{-1}$ were attained. The approximate size of these flakes, from Figure 5.25, ranged between 0.1 and 2 µm. It should be noted that literature reports flake sizes smaller than 0.5 µm have five times lower conductivities of 1000 vs 5000 S $cm^{-1}$, than flakes around 5 µm. It is further believed that this conductivity trend continues for both smaller and larger flake sizes (Maleski et al., 2018). Based on the above, it was expected that the desired conductive properties of the $Ti_3C_3T_x$ sheets would have been diminished in increasing its specific surface area. It was also noted that agglomeration occurs with increasing effect as $Ti_3C_2T_x$ sheet size is reduced. This is said to be caused by strong van der Waal's forces between the negatively charged delaminated sheets attracting each other (Ahmad Junaidi et al., 2021). While the increase in degree of flake agglomeration was initially seen as beneficial due to the porosity it offers for catalyst deposition, there were unexpected consequences for both the activity and durability which are later addressed in the discussion.

By performing metal organic chemical deposition at 350 °C for 2 hours, well dispersed platinum nanoparticles averaging between 2 and 5 nm were consistently deposited onto the $Ti_3C_2T_x$ support. While the deposition was confirmed successful through TEM imaging, the location of the nanoparticles could not be confirmed to be within the porous agglomerated structures or only on their surfaces. This is a significant consideration as shown in a study by Lee et al. (2021), where particles deposited on the edge of sheets are found to donate more electrons to platinum than basal dominated supports.

The initial electrochemical performance evaluation used a 40 equivalent Pt/C wt % to synthesize an equally dispersed Pt/MXene catalyst. It was immediately evident that no part of the catalyst was electrochemically active as shown in Figure 5.31. Similar results were shown in Figure 5.34 for the 40 wt % Pt/MXene, even though this loading is considered relatively high for a support with a specific surface area of 86 $m^2 g^{-1}$. The cause for these poor results relates back to the conductivity constraint that lies within utilizing small flakes as well potentially the location of the deposited Pt nanoparticles.

With the incorporation of carbon to the catalyst material in the ink formulation stage, a degree of electrochemical surface area could be observed. While this was less than half of that of Pt/C which was 80 by comparison to the Pt/$Ti_3C_2T_x$'s 28 $m^2 g^{-1}$, it served as a strong indication as to where the electrochemical constraints lie. Upon accelerated durability testing of the Pt corrosion, the MXene supported catalyst was rendered inactive after only 3000 cycles. By comparison to a commercial catalyst, this loss is extremely high. After 3000 cycles the commercial catalyst lost only 13 % of its ECSA. This high loss of ECSA for the Pt/$Ti_3C_2T_x$ catalyst is due to an unstable support or a poor metal-support interaction. There are therefore three potential issues identified:

- A poorly conductive support material
- An unstable support material
- An unfavoured metal-support interaction

While the cause of the low conductivity has been clearly identified and related to the small flakes shown in the results and Figure 5.25, the underlying principle was described by Maleski et al. (2018). The decrease in conductivity they hypothesized, is the result of more defective flakes and by correlation, an increase in the number of flake end interfaces which leads to increased resistance between flakes. Having decreased the lateral flake size and by virtue, increased the number of interfaces, their hypothesis agrees with what was observed in the results. Further agreement with results from literature is provided by Lee et al. (2021), where individual sheets are seen as less conductive than those with multiple (22), layers.

What was observed as potentially an unstable support or an undesired metal-support interaction limiting the stability of the catalyst, was unexpected based on the MXene's ability to withstand both the acidic environment and oxidation under PEFC operating conditions (Xie et al., 2013; Li, Wang, et al., 2015). Further, their surface termination groups (-F, -O, and -OH) are said to enhance the interaction between the platinum nanoparticles and the MXene's hydrophilic surface (Xie et al., 2013). More specifically to the above, strong platinum-support interactions are said to arise from -O terminated MXene's.

By comparison, F-terminated MXene's, with weaker interactions, however, show increased activity and performance for the ORR. By the synthesis method here reported, it was expected that both termination groups were present (Liu & Li, 2019). This therefore suggested a relatively proportionate degree of both a favourable metal support interactions and activity would be observed.

It was therefore expected from the literature that the $Ti_3C_2T_x$ support would overcome deficiencies presented by the currently employed supports. This was, however, until a recent study by Zhang et al. (2020), showed that MXene flake disorder and restacking may trap unwanted intermediate products formed during the oxygen reduction reaction. Not only do these intermediates restrict catalyst site access, but in accordance with Hazirah & Junaidi (2021), also result in both a two and four electron transfer processes occurring. This is said to occur between sheets or in porous regions where Pt nanoparticles have been deposited. As mentioned in Section 2.1.3, the two-electron transfer process is highly undesirable as in accordance with Equations 6 to 9, these protonation and reduction reactions form hydrogen peroxide. As discussed, hydrogen peroxide is extremely detrimental to the PEFC proton exchange membrane. The damage to the PEM is irreversible and is identified as the cause of the rapid ECSA observed during the accelerated durability testing of the $Pt/Ti_3C_2T_x$ catalyst. This is specifically as he methodology in this report synthesized high specific surface area, or 86 $m^2\ g^{-1}$ delaminated $Ti_3C_2T_x$ sheets. These sheets, due to their small sizes and increased interfaces therefore possess many porous regions as shown in Figure 5.25 where trapped intermediates formed from the ORR can further react.

Means of mitigation to the above has been previously investigated by Xu et al. (2020), who have hybridized $Ti_3C_2T_x$ with carbon nanotubes. They then found that the composite material enhances both durability and ORR activity performance compared to Pt/C. Further mitigation should extend to optimizing on that work with a focus on tuning the Pt nanoparticle deposition position, and the $Ti_3C_2T_x$ termination groups such that the selectivity of surface activity and durability may ensue.

# Chapter Seven: Conclusions and Recommendations

## 7.1 Conclusions of the Study

$Ti_3C_2T_x$ was first synthesised from hot pressed $Ti_3AlC_2$ using in-situ HF methods. Here, it was found that larger flakes can be synthesized than HF methods due to intercalation performed by $Li^+$ ions. The SSA of flakes synthesised from in-situ methods, however, is limited to below 14 $m^2 g^{-1}$. For in-situ methods, etching at a higher temperature, for a longer time and using a 3:1 HCl:LiF ratio provided the most delaminated flakes. By synthesising $Ti_3C_2T_x$ using HF methods, similar conclusions were drawn for etching time and concentration with the following additional conclusions:

- The SSA of $Ti_3C_2T_x$ is dependent on the starting particle size of the $Ti_3AlC_2$ MAX phase
- Sonicating for a longer time provides a higher degree of exfoliation
- Grinding before sonicating has significant effects on the performance of the sonication and by correlation, the SSA of the flakes
- By delaminating and reducing the $Ti_3C_2T_x$ flake size, large porous agglomerates of sheets are formed and held together by van der Waals forces

For the electrochemical performance evaluation, little activity was rendered in initial tests due to poor support conductivity. The support conductivity was significantly lower than the reported literature due to its direct relationship to flake size which was significantly reduced in this project to meet the reported guidelines. The decreased flake size increased the number of sheet interfaces and by virtue, increased the electrical resistance. The conductivity was possibly further reduced by the Pt deposition which could have favoured basal over edge anchoring on account of the smaller sheets.

After eliminating the conductivity constraint through the synthesis of a hybrid electrode, it was found that due to the agglomerated $Ti_3C_2T_x$ sheet regions, the entrapment of ORR intermediates occur. These trapped intermediates then go on to limit catalytic site access and react and form $H_2O_2$, irreversibly damaging the PEFC proton exchange membrane and ultimately rendering the catalyst inactive.

## 7.2 Recommendations from the Study

The relationship between flake size and conductivity is inversely proportional and, on this basis, in-situ methods are preferred. However, while conductivity is an essential element for an electrochemical performance evaluation, the low specific surface area of these sheets, placed it significantly short of the advanced support requirement which requires high Pt dispersion.

As expected from the relationship between conductivity and flake size, the high specific surface area MXene's synthesized from HF etching was found to be a poor conductor and therefore significant limitations were posed on electron transport. Given the extremely hazardous nature of HF it should be investigated to try and find an alternative acid for the etching process. A further limitation resulting from the high specific surface area MXene application included the entrapment of ORR intermediates.

To mitigate the above concerns, it is recommended to perform density gradient centrifugation to isolate a specific range of delaminated lateral flake sizes. The uniformity of the flakes will aid in maintaining a constant degree of electron transport across the support material. It is further recommended that the ratio of carbon addition is optimized or the use of carbon nanotubes to limit catalyst support agglomeration is optimized. Lastly, the selectively of the termination groups on the MXene's surfaces should be tuned, the material doped, and the Pt nanoparticle deposition position optimized to increase its activity toward the ORR. These recommendations may allow for the synthesize a catalyst which can meet the DoE's PEFC durability targets with similar activity to the carbonaceous.

# References


Ahmad Junaidi, N., Wong, W., Loh, K., Rahman, S. & Daud, W. 2021. A comprehensive review of MXenes as catalyst supports for the oxygen reduction reaction in fuel cells. *International Journal of Energy Research*. 45(1):15760–15782. DOI: 10.1002/er.6899.

Alhabeb, M., Maleski, K., Anasori, B., Lelyukh, P., Clark, L., Sin, S. & Gogotsi, Y. 2017. Guidelines for synthesis and processing of two-dimensional titanium carbide ($Ti_3C_2T_x$ MXene). *Chemistry of Materials*. 29(18):7633–7644. DOI: 10.1021/acs.chemmater.7b02847.

Antolini, E. 2009. Palladium in fuel cell catalysis. *Energy and Environmental Science*. 2(9):915–931. DOI: 10.1039/b820837a.

Barsoum, M. & Radovic, M. 2011. Elastic and mechanical properties of the MAX phases. *Annual review of materials research*. 41:195–227. DOI: 10.1146/annurev-matsci-062910-100448.

Castillo, J.L., Martin, S., Rodriguez-perez, D., Higuera, F.J. & Garcia-ybarra, P.L. 2018. Nanostructured porous coatings via electrospray atomization and deposition of nanoparticle suspensions. *Journal of Aerosol Science*. 125(March):148–163. DOI: 10.1016/j.jaerosci.2018.03.004.

Cheng, X., Shi, Z., Glass, N., Zhang, L., Zhang, J., Song, D., Liu, Z., Wang, H., Shen, J. 2007. A review of PEM hydrogen fuel cell contamination: Impacts, mechanisms, and mitigation. *Journal of Power Sources*. 165(2):739–756. DOI: 10.1016/j.jpowsour.2006.12.012.

Eklund, P., Palmquist, J., Howing, J., Trinh, D., El-Raghy, T., Hogberg, H. & Hultman, L. 2007. $Ta_4AlC_3$: Phase determination, polymorphism and deformation. *Acta Materialia*. 55(14):4723–4729. DOI: 10.1016/j.actamat.2007.04.040.

Eklund, P., Rosen, J. & Persson, P. 2017. Layered ternary $M_{n+1}AX_n$ phases and their 2D derivative MXene: An overview from a thin-film perspective. *Journal of Physics D: Applied Physics*. 50(11):11301. DOI: 10.1088/1361-6463/aa57bc.

Fabbri, E., Mohamed, R., Levecque, P., Conrad, O. & Schmidt, T.J. 2014. Perovskite and carbon toward oxygen reduction in alkaline media. *ACS catalysis*. 4(4):1061–1070. DOI: 10.1021/cs400903k.

Faraji, M., Parsaee, F. & Kheirmand, M. 2021. Facile fabrication of N-doped graphene/$Ti_3C_2T_x$ (Mxene) aerogel with excellent electrocatalytic activity toward oxygen reduction reaction in fuel cells and metal-air batteries. *Journal of Solid State Chemistry*. 303:122529. DOI: 10.1016/j.jssc.2021.122529.

Fu, T., Fang, J., Wang, C. & Zhao, J. 2016. Hollow porous nanoparticles with Pt skin on Ag-Pt alloy structure as highly active electrocatalyst for oxygen reduction reaction. *Journal of Materials Chemistry A*. 4(22):8803–8811. DOI: 10.1039/C6TA02202B.

Garsany, Y., Baturina, O.A., Swider-lyons, K.E. & Kocha, S. 2010. Experimental methods for quantifying the activity of platinum electrocatalysts for the oxygen. *Analytical Chemistry*. 82(15):6321–6328. DOI: 10.1021/ac100306c.

Garsany, Y., Singer, I.L. & Swider-Lyons, K.E. 2011. Impact of film drying procedures on RDE characterization of Pt/VC electrocatalysts. *Journal of Electroanalytical Chemistry*. 662(2):396–406. DOI: 10.1016/j.jelechem.2011.09.016.

Garsany, Y., Ge, J., St-Pierre, J. & Rocheleau, R. 2014. Analytical procedure for accurate comparison of rotating disk electrode results for the oxygen reduction activity of Pt/C. *Journal of The Electrochemical Society*. 161(5):628–640. DOI: 10.1149/2.036405jes.

Ghosh, N.C. & Harimkar, S.P. 2012. Consolidation and synthesis of MAX phases by spark plasma sintering (SPS): A review. *Advances in Science and Technology of $M_{n+1}AX_n$ Phases*. 47–80. DOI: 10.1533/9780857096012.

Gómez-Navarro, C., Burghard, M. & Kern, K. 2008. Elastic Properties of Chemically Derived Single Graphene Sheets. *Nano Letters*. 8(7):2045–2049. DOI: 10.1021/nl801384y.

HA, H., vam Man, T., Tai, H. & HTT, V. 2016. Preparation and characterization of high-dispersed pt/c nano-electrocatalysts for fuel cell applications. *Vietnam Journal of Science and Technology*. 54(4):472. DOI: 10.15625/0866-708X/54/4/7308.

Halim, J. 2016. An X-Ray Photoelectron Spectroscopy Study of Multilayered Transition Metal Carbides (MXenes). Drexel University. DOI: 10.1016/j.apsusc.2015.11.089.

Holton, B.O.T. & Stevenson, J.W. 2013. The role of platinum in proton exchange membrane fuel cells. *Platinum Metals Review*. 57(4):259–271. DOI: 10.1595/147106713X671222.

Huang, S., Ganesan, P. & Popov, B.N. 2010. Environmental electrocatalytic activity and stability of niobium-doped titanium oxide supported platinum catalyst for polymer electrolyte membrane fuel cells. *Applied Catalysis B, Environmental*. 96(1–2):224–231. DOI: 10.1016/j.apcatb.2010.02.025.

Jackson, C., Smith, G.T., Inwood, D.W., Leach, A.S., Whalley, P.S., Callisti, M., Polcar, T., Russell, A.E., Levecque, P., Kramer, D. 2017. Electronic metal-support interaction enhanced oxygen reduction activity and stability of boron carbide supported platinum. *Nature Communications*. 8:1–11. DOI: 10.1038/ncomms15802.

Jaksic, J., Ristic, N., Krstajic, N. & Jaksic, M. 1998. Electrocatalysis for hydrogen electrode reactions in the light of fermi dynamics and structural bonding FACTORS—I. individual electrocatalytic properties of transition metals. *International Journal of Hydrogen Energy*. 23(12):1121–1156. DOI: 10.1016/S0360-3199(98)00014-7.

Koyappayil, A., Chavan, S.G., M, M., Go, A., SY, H. & Lee, M. 2020. β-Hydroxybutyrate dehydrogenase decorated MXene nanosheets for the amperometric determination of β-hydroxybutyrate. *Microchimica Acta*. 187(5):1–7. DOI: 10.1007/s00604-020-04258-y.

Kumar, S., Kang, D., Hong, H., Rehman, A., Lee, Y. & Seo, Y. 2020. Effect of $Ti_3C_2T_x$ MXenes etched at elevated temperatures using concentrated acid on binderfree supercapacitors. *RSC Advances*. 10(68):41837–41845. DOI: 10.1039/d0ra05376g.

Lee, Y., Hyuk, J., Park, H., Jung, J., Jeon, Y., Lee, D., Kim, M., Lee, E., Kim, C., Kwon, Y. 2021. Support structure-catalyst electroactivity relation for oxygen reduction reaction on platinum supported by two-dimensional titanium carbide. *Nano Energy*. 79:105363. DOI: 10.1016/j.nanoen.2020.105363.

Lei, J., Zhang, X. & Zhou, Z. 2015. Recent advances in MXene: Preparation, properties, and applications. *Frontiers of Physics*. 10(3):276–286. DOI: 10.1007/s11467-015-0493-x.

Li, X. & Hsing, I. 2006. The effect of the Pt deposition method and the support on Pt dispersion on carbon nanotubes. *Electrochimica Acta*. 51(25):5250–5258. DOI: 10.1016/j.electacta.2006.01.046.

Li, L., Hu, L., Li, J. & Wei, Z. 2015. Enhanced stability of Pt nanoparticle electrocatalysts for fuel cells. *Nano Research*. 8(2):418–440. DOI: 10.1007/s12274-014-0695-5.

Li, Z., Wang, L., Sun, D., Zhang, Y., Liu, B., Hu, Q. & Zhou, A. 2015. Synthesis and thermal stability of two-dimensional carbide MXene $Ti_3C_2$. *Materials Science and Engineering B: Solid-State Materials for Advanced Technology*. 191(C):33–40. DOI: 10.1016/j.mseb.2014.10.009.

Lipatov, A., Alhabeb, M., Lukatskaya, M.R., Boson, A., Gogotsi, Y. & Sinitskii, A. 2016. Effect of synthesis on quality, electronic properties and environmental stability of individual monolayer $Ti_3C_2$ MXene flakes. *Advanced Electronic Materials*. 2(12). DOI: 10.1002/aelm.201600255.

Liu, C. & Li, E.Y. 2019. Termination effects of Pt/V-$Ti_{n+1}C_nT_2$ MXene surfaces for oxygen reduction reaction catalysis. *ACS Applied Materials & Interfaces*. 11(1):1638–1644. DOI: 10.1021/acsami.8b17600.

Liu, D., Wang, R., Chang, W., Zhang, L., Peng, B., Li, H., Liu, S., Yan, M., Guo, C. 2018. $Ti_3C_2$ MXene as an excellent anode material for high-performance microbial fuel cells. *Journal of Materials Chemistry A*. 6(42):20887–20895. DOI: 10.1039/c8ta07305h.

Liu, F., Zhou, A., Chen, J., Jia, J., Zhou, W. & Wang, L. 2017. Preparation of $Ti_3C_2$ and $Ti_2C$ MXenes by fluoride salts etching and methane adsorptive properties Applied Surface Science Preparation of $Ti_3C_2$ and $Ti_2C$ MXenes by fluoride salts etching and methane adsorptive properties. *Applied Surface Science*. 416:781–789. DOI: 10.1016/j.apsusc.2017.04.239.

Lv, H., Mu, S., Cheng, N. & Pan, M. 2010. Environmental Nano-silicon carbide supported catalysts for PEM fuel cells with high electrochemical stability and improved performance by addition of carbon. *Applied Catalysis B, Environmental*. 100(1–2):190–196. DOI: 10.1016/j.apcatb.2010.07.030.

Magnuson, M. & Mattesini, M. 2017. Chemical bonding and electronic-structure in MAX phases as viewed by X-ray spectroscopy and density functional theory. *Thin Solid Films*. 621:108–130. DOI: 10.1016/j.tsf.2016.11.005.

Maleski, K., Ren, C.E., Zhao, M.Q., Anasori, B. & Gogotsi, Y. 2018. Size-dependent physical andelectrochemical properties of two-dimensional MXene flakes. *ACS Applied Materials and Interfaces*. 10(29):24491–24498. DOI: 10.1021/acsami.8b04662.

Marinho, B., Ghislandi, M., Tkalya, E., Koning, C.E. & With, G. De. 2012. Electrical conductivity of compacts of graphene, multi-wall carbon nanotubes, carbon black, and graphite powder. *Powder Technology*. 221:351–358. DOI: 10.1016/j.powtec.2012.01.024.

Mashtalir, O., Naguib, M., Dyatkin, B., Gogotsi, Y. & Barsoum, M.W. 2013. Kinetics of aluminum extraction from $Ti_3AlC_2$ in hydro fl uoric acid. *Materials Chemistry and Physics*. 139(1):147–152. DOI: 10.1016/j.matchemphys.2013.01.008.

Naguib, M., Kurtoglu, M., Presser, V., Lu, J., Niu, J., Heon, M., Hultman, L., Gogotsi, Y., Barsoum, M. 2011. Two-dimensional nanocrystals produced by exfoliation of $Ti_3AlC_2$. *Advanced Materials*. 23(37):4248–4253. DOI: 10.1002/adma.201102306.

Naguib, M., Mashtalir, O., Carle, J., Pressler, V., Lu, J., Hult, am, L., Gogotsi, Y. & Barsoum, M.W. 2012. Two-dimensional transition metal carbides. *ACS Nano*. 6(2):1322–1331. DOI: 10.1021/nn204153h.

Nie, Y., Li, L. & Wei, Z. 2015. Recent advancements in Pt and Pt-free catalysts for oxygen reduction reaction. *Chemical Society Reviews*. 44(8):2168–2201. DOI: 10.1039/c4cs00484a.

Nørskov, J.K., Rossmeisl, J., Logadottir, A., Lindqvist, L., Lyngby, D.- & Jo, H. 2004. Origin of the overpotential for oxygen reduction at a fuel-cell cathode. *The Journal of Physical Chemistry B*. 108(46):17886–17892. DOI: 10.1021/jp047349j.

Palatkar, G.M., Dhopte, P.V. & Sajjanwar, S.W. 2017. Recent trends and comparison in fuel cell technology. *Chemical Engineering Transactions*. 4(1):214–218. DOI: 10.24001/ijaems.icsesd2017.76.

Palma, V., Vaiano, V., Matarangolo, M. & Anello, G. 2018. Comparison of Pt/C electrocatalyst deposition methods for PEM fuel cells. *Chemical Engineering Transactions*. 70:1525–1530. DOI: 10.3303/CET1870255.

Rabis, A., Rodriguez, P. & Schmidt, T.J. 2012. Electrocatalysis for polymer electrolyte fuel cells: Recent achievements and future challenges. *ACS Catalysis*. 2(5):864–890. DOI: 10.1021/cs3000864.

Rayment, C. & Sherwin, S. 2003. Introduction to Fuel Cell Technology. *Department of Aerospace and Mechanical Engineering*. 46556:11–12.

Regali, F., Liotta, L.F., Venezia, A.M., Montes, V., Boutonnet, M. & Järås, S. 2014. Effect of metal loading on activity, selectivity and deactivation behavior of Pd/silica-alumina catalysts in the hydroconversion of n-hexadecane. *Catalysis Today*. 223:87–96. DOI: 10.1016/j.cattod.2013.08.028.

Sathiskumar, C., Ramakrishnan, S., Vinothkannan, M. & Rhan, A. 2019. Nitrogen-doped porous carbon derived from Biomass used as trifunctional electrocatalyst toward oxygen reduction, oxygen evolution and hydrogen evolution reactions. *Nanomaterials*. 10(1):76. DOI: 10.3390/nano10010076.

Sethuraman, V.A. & Weidner, J.W. 2010. Analysis of sulfur poisoning on a PEM fuel cell electrode. *Electrochimica Acta*. 55(20):5683–5694. DOI: 10.1016/j.electacta.2010.05.004.

Shahzad, A., Rasool, K., Miran, W., Nawaz, M., Jang, J., Mahmoud, K.A. & Lee, D.S. 2017. Two-dimensional Ti3C2Tx MXene nanosheets for efficient copper removal from water. *ACS Sustainable Chemistry and Engineering*. 5(12):11481–11488. DOI: 10.1021/acssuschemeng.7b02695.

Sharma, S. & Pollet, B.G. 2012. Support materials for PEMFC and DMFC electrocatalysts - A review. *Journal of Power Sources*. 208:96–119. DOI: 10.1016/j.jpowsour.2012.02.011.

Sinha, A., Zhao, H., Huang, Y., Lu, X., Chen, J. & Jain, R. 2018. MXene: An emerging material for sensing and biosensing. *Trends in Analytical Chemistry*. DOI: 10.1016/j.trac.2018.05.021.

Stephens, I.E.L., Bondarenko, A.S., Grønbjerg, U., J, R. & Chorkendorff, I. 2012. Understanding the electrocatalysis of oxygen reduction on platinum and its alloys. *Energy and Environmental Science*. 5(5):6744–6762. DOI: 10.1039/c2ee03590a.

Tang, Y., Yang, C. & Que, W. 2018. A novel two-dimensional accordion-like titanium carbide (MXene) for adsorption of Cr (VI) from aqueous solution. *Journal of Advanced Dielectrics*. 8(5):1–5. DOI: 10.1142/S2010135X18500352.

Taylor, S., Fabbri, E., Levecque, P., Schmidt, T.J. & Conrad, O. 2016. The effect of platinum loading and surface morphology on oxygen reduction activity. *Electrocatalysis*. 287–296. DOI: 10.1007/s12678-016-0304-3.

Trogadas, P., Fuller, T.F. & Strasser, P. 2014. Carbon as catalyst and support for electrochemical energy conversion. *Carbon*. 75:5–42. DOI: 10.1016/j.carbon.2014.04.005.

Vliet, D. Van Der, Wang, C., Debe, M., Atanasoski, R., Markovic, N.M. & Stamenkovic, V.R. 2011. Platinum-alloy nanostructured thin film catalysts for the oxygen reduction reaction. *Electrochimica Acta*. 56(24):8695–8699. DOI: 10.1016/j.electacta.2011.07.063.

Wang, X.H. & Zhou, Y.C. 2010. Layered machinable and electrically conductive $Ti_2AlC$ and $Ti_3AlC_2$ ceramics: A review. *Journal of Materials Science & Technology*. 26(5):385–416. DOI: 10.1016/s1005-0302(10)60064-3.

Wang, C., Markovic, N.M. & Stamenkovic, V.R. 2012. Advanced platinum alloy electrocatalysts for the oxygen reduction reaction. *ACS Catalysis*. 2(5):891–898. DOI: 10.1021/cs3000792.

Wang, X., Kumar, R., Myers, D.J., Lett, E.S., A-a, P., Wang, X., Kumar, R. & Myers, D.J. 2006. Effect of voltage on platinum dissolution: relevance to polymer electrolyte fuel cells. *Electrochemical and Solid-State Letters*. 9(5):225–228. DOI: 10.1149/1.2180536.

Wang, Z., Xu, D., Zhong, H., Wang, J., Meng, F. & Zhang, X. 2015. Gelatin-derived sustainable carbon-based functional materials for energy conversion and storage with controllability of structure and component. *Science Advances*. 1(1):1–9. DOI: 10.1126/sciadv.1400035.

Wei, Y., Zhang, P., Soomro, R.A., Zhu, Q. & Xu, B. 2021. Advances in the synthesis of 2D MXenes. *Advanced Materials*. 33(39):1–30. DOI: 10.1002/adma.202103148.

Wu, D., Shen, X., Pan, Y., Yao, L. & Peng, Z. 2020. Platinum alloy catalysts for oxygen reduction reaction: Advances, challenges and perspectives. *ChemNanoMat*. 6(1):32–41. DOI: 10.1002/cnma.201900319.

Xie, X., Chen, S., Dang, W., Nie, Y. & Wei, Z. 2013. An extraordinarily stable catalyst: Pt NPs supported on two-dimensional $Ti_3C_2X_2$ (X=OH, F) nanosheets for oxygen reduction reaction. *Chemical Communications*. 49(86):10112–10114. DOI: 10.1039/c3cc44428g.

Xu, C., Fan, C., Zhang, X., Chen, H., Liu, X., Fu, Z., Wang, R., Hong, T., Cheng, J. 2020. MXene ($Ti_3C_2T_x$) and carbon nanotube hybrid-supported platinum catalysts for the high-performance oxygen reduction reaction in PEMFC. *ACS Applied Materials & Interfaces*. 12(17):19539–19546. DOI: 10.1021/acsami.0c02446.

Yoon, Y., Le, T.A., Tiwari, A.P., Kim, I., Barsoum, M.W. & Lee, H. 2018. Low temperature solution synthesis of reduced two dimensional $Ti_3C_2$ MXenes with paramagnetic behaviour. *Nanoscale*. 10(47):22429–22438. DOI: 10.1039/c8nr06854b.

Yuan, X.-Z., Wang, H. & Zhang, J. 2008. PEM fuel cell fundamentals. In *PEM Fuel Cell Electrocatalysts and Catalyst Layers: Fundamentals and Applications*. London: Springer. 1–87.

Zhang, C., Ma, B., Zhou, Y. & Wang, C. 2020. Highly active and durable Pt/MXene nanocatalysts for ORR in both alkaline and acidic conditions. *Journal of Electroanalytical Chemistry*. 865:114142. DOI: 10.1016/j.jelechem.2020.114142.

Zhao, C., Wang, Q., Zhang, H., Passerini, S. & Qian, X. 2016. Two-dimensional titanium carbide/RGO composite for high-performance two-dimensional titanium carbide/RGO composite for high-performance supercapacitors. *ACS applied materials & interfaces*. 8(24):15661–15667. DOI: 10.1021/acsami.6b04767.

Zhou, A. 2012. Methods of MAX-phase synthesis and densification – II. In *In Advances in Science and Technology of $M_{n+1}AX_n$ Phases*. Woodhead Publishing. 21–46. DOI: 10.1016/B978-1-84569-991-8.50002-3.